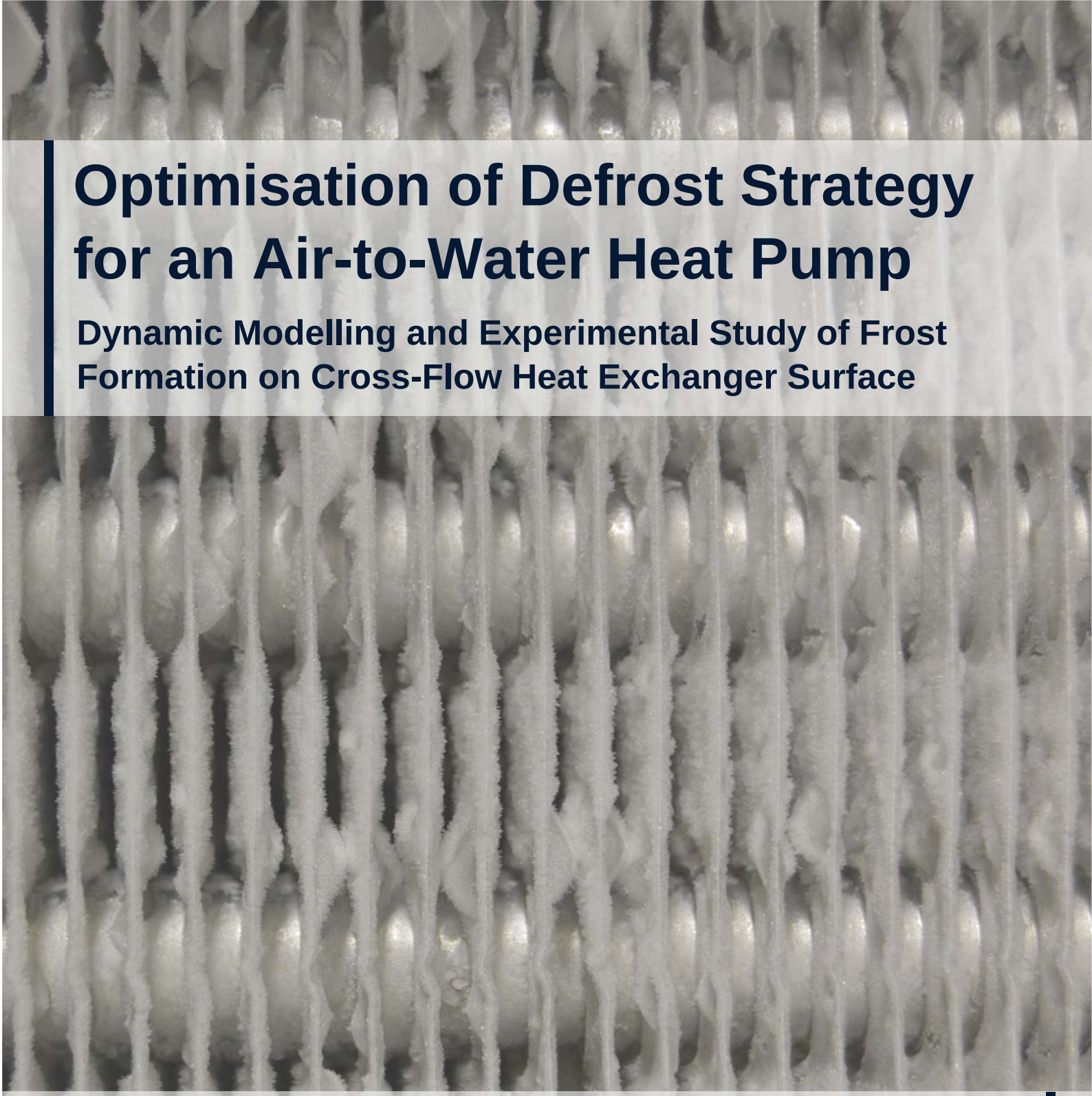

Optimisation of Defrost Strategy for an Air-to-Water Heat Pump

Dynamic Modelling and Experimental Study of Frost Formation on Cross-Flow Heat Exchanger Surface

Emil Ø. Schmidt & Mikael S. Kristensen

Master Thesis

Thermal Energy & Process Engineering
Department of Energy Technology
Aalborg University

June 2014

AALBORG UNIVERSITY
STUDENT REPORT

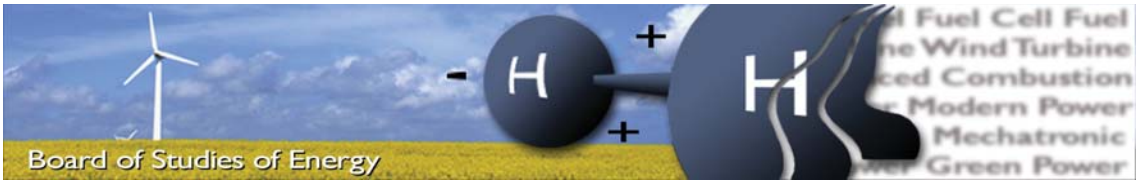

Title:	Optimisation of Defrost Strategy for an Air-to-Water Heat Pump - Dynamic Modelling and Experimental Study of Frost Formation on Cross-Flow Heat Exchanger Surface
Semester:	10th
Semester theme:	Master thesis
Project period:	03.02.2014 to 03.06.2014
ECTS:	30
Supervisors:	Mads Pagh Nielsen & Carsten Bojesen
Project group:	TEPE4-1001

Emil Østergaard Schmidt

Mikael Skrydstrup Kristensen

Copies:	6
Pages, total:	154
Pages, report:	126
Pages, enclosure:	14
Pages, formalia:	14
Appendices:	A-D
Supplements:	CD

SYNOPSIS:

Formation of frost on heat exchanger surfaces is a well known issue in air source heat pump systems at low ambient temperatures. The purpose of this project is to improve the defrosting strategy of a DVI LV9 Combi heat pump, which currently operates with a fixed defrost interval of 60 minutes. A model is developed to determine the reduction in heat pump performance as frost develops on the evaporator surface and to calculate the optimal defrost initiation point. The model is validated against experimental measurements acquired at relative humidities in the range of 65% to 85% and air temperature of -4°C to 4°C. Two 5-hour experiments are conducted at identical conditions in order to compare the current defrost strategy to the one determined by the model. The model suggests a defrost interval of 35 minutes at the given conditions, which is found to be consistent with the point where the heat pump would otherwise have a significant decrease in performance. The new strategy results in a more stable performance, but does not improve the coefficient of performance significantly. A more stable performance would probably allow DVI Energi to reduce the superheat reference point and increase the performance of the heat pump.

By signing this document, each member of the group confirms that all participated in the project work and thereby all members are collectively liable for the content of the report. Signing this document also confirms that this report does not contain any plagiarism.

Preface

This is a master thesis project written in the period 3rd of February to 3rd of June 2014 at Department of Energy Technology at Aalborg University, Denmark.

The models in this thesis are developed in MathWorks MATLAB or Engineering Equation Solver. MATLAB uses REFPROP, developed by National Institute of Standards and Technology (NIST), to provide thermodynamic properties of fluids.

The project is developed in cooperation with DVI Energi who has provided equipment and facilities for experiments. The models developed throughout the project are validated using a DVI air-to-water heat pump with a rated heating capacity of 9 kW, with the evaporator located in a climate chamber.

Reading Instructions
Throughout the project, references are collected in a bibliography in the back of the report. The source reference follows the Harvard method, where the source in the text is referenced to with [Author, Year]. If the source is placed before a period in the end of a sentence, the source will cover the statement in that sentence. If the source is placed after a period, the source refers to the full paragraph.

Figures, tables, equations and calculations are numbered according to the chapter where they are located. That is, the first figure in chapter 4 has the number 4.1, the next number 4.2, etc. Explaining text will be attached beneath figures and above tables. The appendices are addressed with letters, while the files on the attached CD are addressed with numbers.

Acknowledgements
The authors would like to acknowledge Henning Pallesen, CEO at DVI Energi, for providing equipment and facilities for the experiments. Without the help of him this project would not have been possible. Christer Eiersted has spend many hours helping with preparation of the experimental equipment, which has been greatly appreciated. Also the supervisors Mads Pagh Nielsen and Carsten Bojesen have provided great guidance and valuable discussions throughout the project.

Summary

Frost formation on heat exchanger surfaces is a well-known and undesired issue in air source heat pump systems. At low ambient temperatures, frost develops on the surface of the evaporator which reduces the performance of the heat pump. The frost layer reduces the rate of heat transfer in the evaporator because it acts as a thermal insulation. Furthermore, the frost layer blocks part of the air flow passage through the evaporator which causes a further reduction of the performance. As a consequence, air source heat pumps operating in cold and humid conditions need regular defrosting in order to be kept free from frost.

The objective of this project is to develop a reversed cycle defrost control strategy for an air source heat pump that can improve the performance of a commercial heat pump, the DVI LV9 Combi heat pump, compared to its current strategy. The approach is to develop a dynamic model of the frost formation process on the evaporator surface and the heat pump performance reduction, and thereby determine the optimal defrost interval at a set of ambient conditions. The current defrost strategy will be compared to the new developed strategy in an experimental study.

The model of the frost formation process on the evaporator surface is developed as a dynamic model where the heat pump performance reduction is modelled as a consequence of an increasing frost formation. The frost formation process is modelled using empirical correlations for properties of frost. The impact of the frost formation on the flow conditions is modelled to account for the blocking effect of the increasing frost layer development on the evaporator surface.

Experimental studies are performed on the DVI LV9 Combi heat pump in a climate chamber in order to investigate the influence of ambient conditions on the frost formation process and to validate the frost formation model. It is found that higher air temperatures and relative humidities results in more frost to develop on the evaporator surface, leading to a more significant decrease in performance. During all experiments the difference between the air temperature and the evaporation temperature increases during the operation cycle, often with a sudden significant increase which indicates that severe frost conditions affects the operation.

The frost formation model is used to simulate an operation cycle at conditions similar to the experiments. This is done in order to validate the model against the experiments at varied ambient conditions. The model generally underestimates the cooling capacity at conditions that yields a low amount of frost and overestimates at conditions yielding a high amount of frost. At a medium level of frost, the model is consistent with the experimental results with an average deviation of 7.1%.

The model is used to calculate a new defrost interval which is compared to the current defrost strategy in two 5-hour experiments at a relative humidity set point of 80% and an air temperature set point of 3°C. The current strategy is performed with a defrost interval of 60 minutes. A new defrost interval is determined by the frost formation model which yields an interval of 35 minutes in the new developed strategy. The COP measured during the two 5-hour experiments is shown in Figure 1.

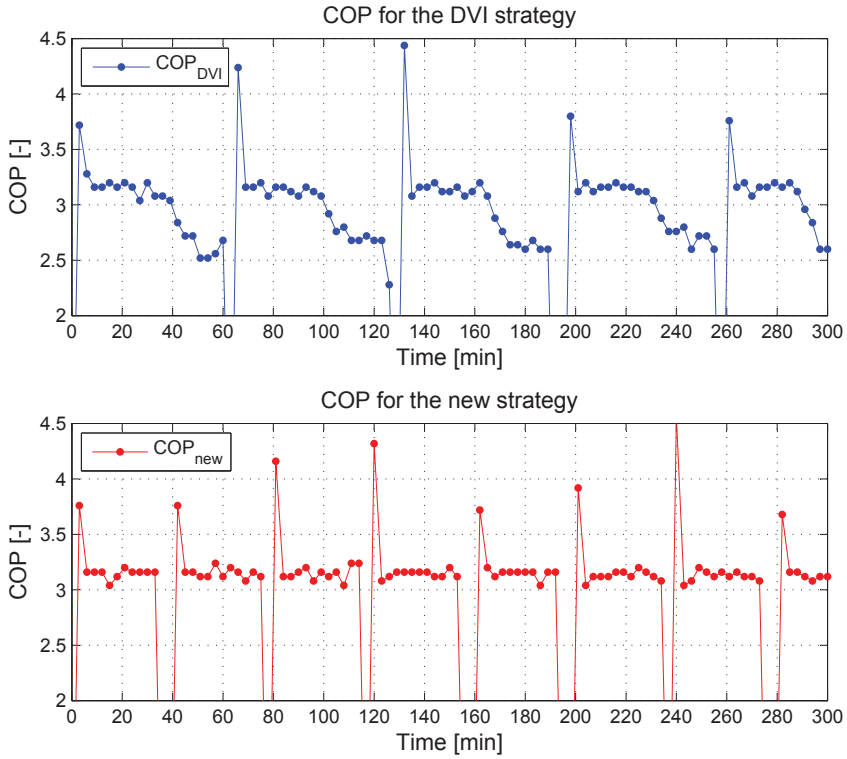

Figure 1. The COP during the 5-hour experiments for defrost intervals of 60 and 35 minutes using the DVI strategy and the new strategy respectively.

The interval of 35 minutes causes the heat pump to initiate a defrost cycle just before a significant drop in performance. Defrosting after 35 minutes therefore results in a more stable operation at the cost of more frequent defrosting cycles. The difference in coefficient of performance during the 5-hour experiments is almost insignificant, indicating that the cost of performing additional defrost cycles is equalized by the more stable performance. However, if the defrosting process is changed according to the reduced interval time it will be beneficial for the new strategy. A more stable performance will probably allow DVI Energi to reduce the superheat reference point and increase the performance.

The developed frost formation model successfully identifies a defrost initiation point that results in more stable heat pump performance. However, the model is very sensitive to the input variables and properties for frost, which makes it more practical to determine the defrost point from measuring the difference between evaporation temperature and ambient temperature. With improvements to the inlet air flow distribution and frost deposition pattern the model could serve as an analysis tool in the refrigeration industry.

Nomenclature

List of Symbols

Symbol	Description	Units
A_{eva}	Evaporator surface area	m^2
A_{fin}	Evaporator fin surface area	m^2
A_{tube}	Evaporator tube surface area	m^2
CT	Condensation temperature	°C
D_{eva}	Depth of evaporator coil	m
D_{fin}	Depth of evaporator fins	m
D_h	Hydraulic diameter	m
$D_{tube,i}$	Evaporator inner tube diameter	m
$D_{tube,o}$	Evaporator outer tube diameter	m
ET	Evaporation temperature	°C
F	Cross-flow correction factor	-
G_{max}	Mass velocity at maximum air velocity	$kg/(m^2s)$
$H_{blocked}$	Amount of height blocked by tubes	m
H_{eva}	Height of evaporator coil	m
H_{fin}	Height of evaporator fins	m
L_{eva}	Length of evaporator coil	m
L_{tube}	Length of evaporator tubes	m
Nu	Nusselt number	-
P	Power	W
P	Temperature ratio	-
Pr	Prandtl number	-
P_{comp}	Compressor electrical input	W
$Q_{defrost}$	Amount of energy required to perform a defrost cycle	J
$Q_{difference}$	Difference between Q_{rated} and Q_{eva}	kWh
Q_{eva}	Heat exchanged while influenced by frosted conditions	kWh
Q_{rated}	Rated heat exchanged at a set of ambient conditions	kWh
$Q_{reproduced}$	Amount of energy that needs to be reproduced after defrost	J
Q_{stop}	Lost heat production due to operation stop	kWh
$\dot{Q}_{eva}$	Cooling capacity of evaporator	W
$\dot{Q}_{supply}$	Total power supplied during defrost	W
$\dot{Q}_{tank}$	Heat transfer rate from storage tank during defrost	W
R	Temperature ratio	-
R	Thermal resistance	K/W
Re	Reynolds number	-
SC	Level of subcooling	°C

Symbol	Description	Units
SH	Level of superheat	°C
S_D	Diagonal tube distance	m
S_L	Longitudinal tube distance	m
S_T	Transverse tube distance	m
T	Temperature	°C
U	Overall heat transfer coefficient	W/m^2
$\dot{V}$	Volumetric flow rate	m^3/s
X_L	Hexagonal length	m
X_M	Hexagonal length	m
f	Friction factor	-
h	Convective heat transfer coefficient	$W/(m^2K)$
h	Enthalpy	kJ/kg
$h_{melting}$	Latent heat of melting of water	kJ/kg
j	Colburn factor	-
k_a	Thermal conductivity of air flow	W/(mK)
k_{fin}	Thermal conductivity of evaporator fins (aluminium)	W/(mK)
k_r	Thermal conductivity of refrigerant flow	W/(mK)
k_{tube}	Thermal conductivity of evaporator tubes (copper)	W/(mK)
m	Mass	kg
m	Standard extended surface parameter	-
$\dot{m}$	Mass flow rate	kg/s
$n_{channels}$	Number of channels on the evaporator air side	-
n_{fin}	Number of evaporator fins	-
n_{tube}	Number of evaporator tubes	-
$n_{tubes,row}$	Number of tubes in a vertical row	-
p	Pressure	kPa
r	Radius	m
r_{eq}	Equivalent radius	m
t_{fin}	Evaporator fin thickness	m
u	Propagated error	-
v	Velocity	m/s
x	Refrigerant quality	-
x_{center}	Position of tube centre	m
x_f	Start point of frost formation	m
x_{fin}	Distance between evaporator fins	m
x_{wall}	Position of tube wall	m

Greek Letters

Symbol	Description	Units
Δ	Difference	-
α	Thermal diffusivity	m^2/s
η	Efficiency	-
ν	Kinematic viscosity	m^2/s
ρ	Density	kg/m^3
σ	Area ratio	-
τ	Time step	-
ϕ	Relative humidity	%
ω	Absolute humidity	kg/kg

Subscripts

Symbol	Description
CF	Cross-flow
LMTD	Log Mean Temperature Difference
a	Air
avg	Average
comp	Compressor
cond	Conductive or condenser
conv	Convective
d.a	Dry air
defrost	Defrost cycle
eva	Evaporator
f	Frost
fr	Frontal
fs	Frost surface
i	Inner
in	Inlet
m	Mean
o	Outer
out	Outlet
r	Refrigerant
reverse	Reversing of 4-way valve
set	Set point
tot	Total
v	Vapour

Abbreviations

Description	Acronym
Air to Water Heat Pump	AWHP
Air Source Heat Pump	ASHP
Brine to Water Heat Pump	BWHP
Coefficient of Performance	COP
Condensation Temperature	CT
Engineering Equation Solver	EES
Evaporation Temperature	ET
Reversed Cycle Defrost	RCD
Subcooling	SC
Superheat	SH

Table of Contents

Chapter 1

Introduction

According to the Danish Energy Agency, heat pumps are expected to play a significant role in the future infrastructure of the Danish energy system. This is due to their large energy saving potential and the possibility to use these in more flexible electrical grids and district heating grids in the future. The Danish Energy Agency plans to phase out all oil boilers in private households by 2035 and replace them by other sources. Out of 205.000 oil boilers in 2013, 86.000 are expected to be replaced by heat pumps while the rest will be replaced by other sources. Furthermore, 87.000 new heat pumps are expected to be installed in new areas without district heating supply. Consequently, an average of approximately 8000 heat pumps are expected to be installed every year towards 2035 in Denmark. (DONG Energy, Energinet.dk and Dansk Energi, 2013)

These heat pumps will mainly be of two types: Brine to Water Heat Pumps (BWHP) and Air to Water Heat Pumps (AWHP). Also Air to Air Heat Pumps (AAHP) are available, but since these cannot interact with the water system of a house, they are not expected to be significant in the large perspective in Denmark. BWHP is usually more efficient, while AWHP are cheaper to install since it is not necessary to bury any geothermal tubes. AWHP is estimated to constitute a significant number of the current and future heat pumps installed in Denmark as well as globally. Together AWHP and AAHP constitute the Air Source Heat Pump (ASHP) type. (DONG Energy, Energinet.dk and Dansk Energi, 2013)

Heat pumps for heating applications usually have most of their operating hours in the winter season where the need of heat is at the highest. Unfortunately, this season also imply a common problem to the ASHP type. At low outdoor air temperatures and at certain outdoor air humidities, a layer of frost will develop on the surface of the evaporator. This layer of frost will gradually increase which reduces the rate of heat transfer and the volumetric air flow through the evaporator. This leads to a degradation of the heat pump's heating capacity and Coefficient of Performance (COP).

To keep the evaporator surface free from frost, a defrosting process must be utilised in the ASHP type to regularly clear the surface from frost in order to keep the performance of the heat pump as high as possible. Depending on the manufacturer and the heat pump design there are a number of strategies used for controlling the defrosting cycle. Since it is difficult to perform a direct measurement of the frost thickness, the control strategies are typically based on indirect parameters such as ambient air temperature and humidity. This implies that the control strategies lead to mal-defrost phenomena, where the ASPH will initiate a defrost cycle either when it is not necessary or when the frost has been severe for too long.

1.1 Estimation of Defrosting Requirement

In order to estimate and quantify the need for defrosting, it is necessary to consider the ambient air temperature. According to DVI Energi, the frost formation problem occurs when the ambient temperature is approximately 4°C or below. At this temperature, the air flow through the evaporator might be cooled to 0°C or lower which will cause frost formation to occur if the evaporator surface is below 0°C. (Pallesen, 2014)

The number of days in the year where an ambient temperature of 4°C or lower is measured in Denmark are considered. That is, if the ambient temperature in a given day at any point drops to 4°C or lower, it will count as a day where defrost might be necessary, hence it is considered in this analysis. So a day with an average temperature of 6°C might have a temperature down to 4°C or lower at some point and will potentially lead to frost formation in the evaporator. This is done using temperature measurements provided by Danish Meteorological Institute (2013) for lowest average day temperature in Denmark. The average ambient temperature over a year in Denmark is approximately 7°C, so it is expected that a large number of days will have temperatures at 4°C or lower. The days in the years of 2011, 2012 and 2013 with temperatures of 4°C or lower in Denmark are plotted and shown in Figure 1.1. (Danish Meteorological Institute, 2013)

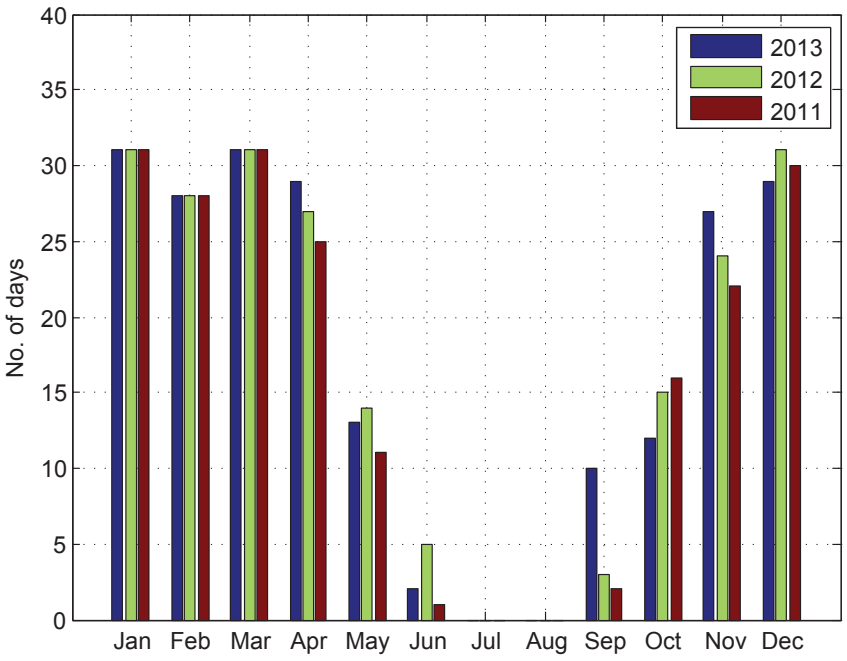

Figure 1.1. The number of days with an ambient temperature lower than 4°C per month in 2011, 2012 and 2013. (Danish Meteorological Institute, 2013)

As seen in Figure 1.1, the amount of days with an ambient temperature lower than 4°C is highest in the winter period as expected. All days in the months of January, February and March have an ambient temperature lower than 4°C. Most of the heat production on a ASHP is in the winter period which means that a large percentage of the production is in days where defrosting might be necessary. The total number of days with an ambient temperature of 4°C or lower for 2011, 2012 and 2013 are 197, 209 and 212 respectively. This corresponds

to a yearly percentage of approximately 54%, 57% and 58% respectively. So in more than half of the days in the year, defrosting might be necessary. On the other hand, the lowest temperatures occurs in the night hours where less heat usually is used, so the heat pump might not operate as much in these hours, hence some of the defrost situations are avoided. Regardless of this, the need to perform defrosting on ASHP's is very significant in the winter period and has a great impact on the performance of this heat pump type.

1.2 Review of Previous Studies on Frost Formation in Air Source Heat Pump Systems

The purpose of this section is to outline the state of the art knowledge and research within the field of frost formation in ASHP systems. Numerous studies have been conducted within this field and most of these are based on experimental approaches. This study includes empirical research on frost formation, parameters that affects frost formation, defrost strategies, mal-defrost phenomena and operating characteristics during defrost.

Frost Formation on Evaporator Surfaces
When the surface temperature of the evaporator is below the freezing point of water, and below the ambient air dew point temperature, a layer of frost will develop on the evaporator surface, where water vapour from the humid air flow will deposit directly from its gaseous state to solid state. Initially, the frost layer increases the air-side heat transfer rate because the rough frosted surface behaves as a finned surface. However, as the frost thickness increases, the insulating effect of the frost layer results in a reduction of the heat transfer rate. Eventually the volumetric air flow is reduced due to an increasing thickness of the frost layer, hence leading to an increased pressure drop through the air side of the evaporator. This effectively reduces the rate of heat transfer and thereby the performance of the heat pump. To avoid this, periodic defrosting is required in order to maintain effective performance of the ASHP. (Don et al., 2011)

Parameters that Influence Frost Formation on Evaporator Surfaces
Several parameters affect the frost formation on the evaporator surface. Ambient air temperature and humidity plays a significant role in the amount of frost that deposits on the evaporator surface. The velocity of the air flow also impacts the frost formation along with the temperature and wettability of the evaporator surface. The geometry and design of the evaporator also impacts the frost formation. (Wang et al., 2011)

Some of these indirect parameters are often used as measurements in experiments in order to determine the primary parameter which is the frost thickness. Because of practical implications in measuring the frost thickness directly it is usually necessary to use these indirect parameters. Both Moallem et al. (2010) and Xu et al. (2012) used advanced image analysis to determine the frost thickness directly, which might be the most successful way to measure frost thickness. This will on the other hand be an impractical and expensive technology to use in commercial heat pumps.

The indirect parameters that are often used to determine the rate of frost formation and frost layer thickness are listed below. (Wang et al., 2011)

- Ambient air temperature
- Ambient air humidity
- Ambient air velocity
- Temperature of heat exchanger surface
- Wettability of heat exchanger surface

Heat Exchanger and Fin Design

The design of the heat exchanger in the evaporator of an ASHP is important to consider regarding frost formation. The most common configurations are fin-and-tube and microchannel heat exchangers. Microchannel heat exchangers are becoming more popular due to their smaller size, compared to fin-and-tube heat exchangers of equivalent capacity, which yields lower costs. On the other hand, fin-and-tube heat exchangers are more widely used in ASHP applications due to a lower rate of frost formation compared to microchannel heat exchangers. Microchannel heat exchanger tubes have a low conductive thermal resistance which results in a fin base temperature which is close to the saturation temperature of the refrigerant. This leads to a higher rate of frost formation. The fin-and-tube and microchannel designs are illustrated in Figure 1.2 which shows cross-flow configurations from front perspective. (Padhmanabhan et al., 2008) (Xu et al., 2012)

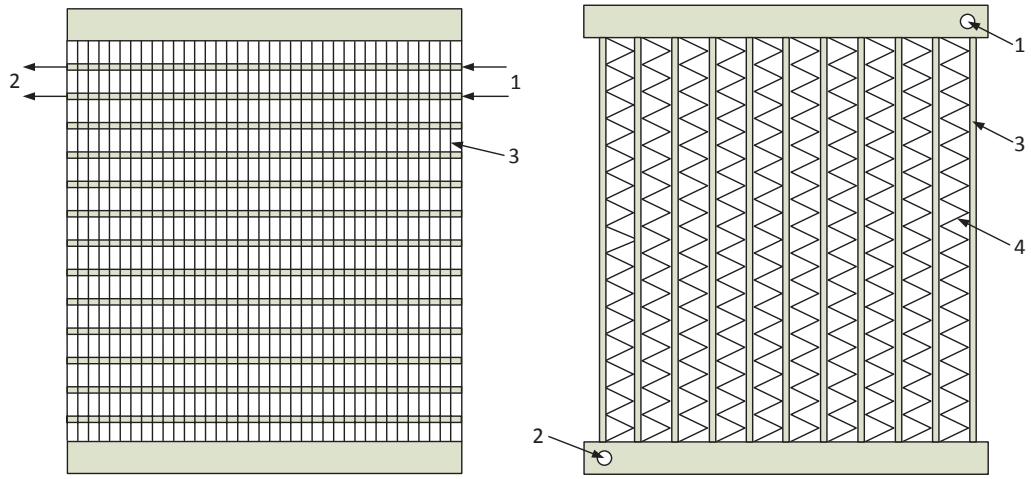

Figure 1.2. Left: The concept of a fin-and-tube cross-flow heat exchanger. Right: The concept of a cross-flow microchannel heat exchanger.

In Figure 1.2, the fin-and-tube heat exchanger concept on the left hand side has the following points: [1] is refrigerant inlet, [2] is refrigerant outlet and [3] is fins. The microchannel heat exchanger concept to the right has the following points: [1] is refrigerant inlet, [2] is refrigerant outlet, [3] is microchannels and [4] is microchannel fins.

Fin-and-tube heat exchangers can have different fin types and the choice of fin affects the frost formation. An experimental investigation on the choice of fins in a frosted fin-and-tube heat exchanger has been performed by Yan et al. (2005). A comparison of flat plate fins without louvers, with one-sided louvers and with re-direction louvers was conducted. The conclusion to the work was that the pressure drop is lowest for flat plate fins without any

louvres, indicating that the amount of frost formation is lowest for this design. It was also found that heat exchangers with a narrow fin spacing are more vulnerable to frost formation than heat exchangers with a wider spacing. (Yan et al., 2005)

Defrost Methods for ASHP Systems

Different defrost methods are utilised in ASHP applications where the most common method used is the reverse cycle defrost (RCD), but several alternative methods have been investigated and tested in previous studies. In the RCD, the heat pump cycle is reversed so that the evaporator operates as condenser and heats the evaporator coil. This is done using a 4-way valve that can reverse the heat pump operation. Different control strategies are applied in order to control the RCD. Alternative methods tested in previous studies are presented below.

- Hot-gas (refrigerant) by-pass defrosting was experimentally tested by Byun et al. (2007) to slow down the frost formation and thereby increase the COP with 8.5% compared to a system without defrost over 210 minutes of operation. The hot-gas is discharged by the compressor and by-passed to the evaporator coil and heat is released to melt the frost.
- Electrical heating of the inflowing air-stream to the evaporator was investigated by Kwak and Bai (2009) and compared to operation without defrost. The method yielded an improvement of the COP at an ambient temperature of 2°C.
- A sensible heat defrosting method was developed by Liang et al. (2010) using a fuzzy control algorithm. A configuration where refrigerant was discharged from the compressor, throttled to low pressure and then sent to the evaporator coil was used for defrosting.
- Dehumidification of the inflow of air to the evaporator was tested by Wang and Liu (2003) using a solid absorbent at the entrance of the evaporator. The absorbent bed was made of zeolite plates with a carbon coat and the method yielded an increased performance of the ASHP. In their experiment, the absorbent bed had a low pressure loss thus the fan of the heat pump did not have to be changed.

Regarding the choice of defrost strategy, a control strategy must be applied in order to perform defrost in the most efficient way possible. The current methods used in ASHP applications are presented in the following.

Control Strategies and Mal-defrost Phenomena

The defrost operation can be controlled in different ways and according to Wang et al. (2011) there are currently 13 defrost strategies used in ASHP applications. A general issue for all of the strategies is that mal-defrost phenomena occurs. Mal-defrost phenomena are defined as defrost operations which are performed either a long time after a critical level of frost is formed or performed when defrosting is not necessary. These two typical mal-defrost phenomena usually occur in all practical applications. The mal-defrost phenomenon due to too late defrosting is usually a problem in humid and moderate climate regions where frost formation occurs fast. In this case defrost often performed a long time after the frost formation is severe on the evaporator surface. The other mal-defrost phenomenon usually occurs in dry and cold climate regions where defrosting is performed in conditions with no frost or only a small amount of frost formation. Mal-defrost phenomena may lead to considerable heat

capacity and energy losses and undesired and uncomfortable heating conditions. The 13 currently used control strategies are shown in Table 1.1. (Wang et al., 2011)

Table 1.1. The 13 current defrost strategies suggested by Wang et al. (2011).

Strategy No.	**Defrost control strategy**	**Defrost control parameter(s)**
Strategy 1	Time initiated - time terminated	Time
Strategy 2	Time initiated - pressure difference terminated	Time; pressure difference
Strategy 3	Using fan power sensor	Fan power
Strategy 4	Neural network techniques	Temperature; humidity; time
Strategy 5	Self-organizing fuzzy control	Pressure of evaporator; fin temperature
Strategy 6	Humidity initiated	Relative humidity
Strategy 7	Measuring thermal conductivity of ice	Thermal conductivity of ice
Strategy 8	Comparing heat transfer rate on air and refrigerant sides of evaporator	Heat transfer rate
Strategy 9	Detecting instability of refrigerant flow into evaporator	Refrigerant mass flow rate
Strategy 10	Time initiated - temperature terminated	Time; temperature of heat exchanger surface
Strategy 11	Temperature difference between air and evaporator surface	Air temperature; evaporator surface temperature
Strategy 12	The surface temperature variation rate	Time; evaporator surface temperature
Strategy 13	Photoelectric method	Frost thickness and photoelectric signals

These strategies and their associated mal-defrost phenomena are elaborated in the following.

Strategy 1: Timed defrost control is a simple and widely used strategy, but it obviously cause unnecessary defrost cycles to occur.
Strategy 2 and 3: Dust blocking of the air flow cross-section in the evaporator will affect the pressure difference which will also directly affect the fan input power. This will lead to mal-defrost operation.
Strategy 4 and 5: Using intelligent control techniques to control defrost cycles requires a certain level of accuracy and with many indirect factors that influence the frosting process this may be complicated. More sensors and advanced algorithms must be used which could increase the cost.
Strategy 6: This technique is only suitable in situations with a more or less constant environment temperature.
Strategy 7 and 8: The measurements of these parameters are very difficult to perform, both in laboratory experiments and in practical applications, so the accuracy of these control strategies are questionable.
Strategy 9: The instability of the flow in the refrigerant is not only affected by the frost formation, but also by changes in ambient conditions and heat pump operation conditions, hence mal-defrost will occur for this strategy.
Strategy 10 to 12: Strategies based on temperature control are the most widely used in ASHP applications because temperature is easily measured. It should although be noted that by controlling defrost based on temperature alone means neglecting humidity which leads to mal-defrost.

Strategy 13: In this method, photoelectric signals measure the thickness of the frost layer. This technique is developed by Byun et al. (2006) and described as a suitable method to control defrost, but there is still no published work on using this method in practical situations.

Current Defrost Strategies in ASHP on the Danish Market
The following section describes the defrost strategies currently used by some of the manufacturers that deliver heat pumps for the Danish market.

Bosch Termoteknik uses the temperature difference between the ambient air and the evaporation temperature to determine when to initiate the defrost cycle. They have a maximum allowed temperature difference as function of the ambient air, and the defrost cycle is initiated when this maximum value is exceeded. Afterwards the condensation temperature is used to terminate the cycle at 20°C. This method corresponds to strategy 11 in Table 1.1, Section 1.2. (Henrik Hansen, 2014)

Danfoss is using an approach similar to that of Bosch Termoteknik, where they compare the temperature of the refrigerant leaving the evaporator to the ambient temperature. Whenever this temperature difference exceeds a specific limit the defrost cycle is initiated. The temperature difference limit is determined by experiments conducted at Danfoss' laboratory in Sweden. The most significant difference in the strategy compared to Bosch Termoteknik, is that Danfoss terminates the defrost cycle when the condensation temperature reaches 38°C. (Christian Hedegaard, 2014)

Operating Characteristics of the Defrost Process
Different operating characteristics are used to determine the efficiency of the defrost process. Defrost time is essential to keep low so that production of heat can continue as soon as possible after defrost has been performed. Obviously it is desired to keep the power consumption of the defrosting process as low as possible to minimise the operation costs. The heat energy utilised during defrost should be kept as low as possible in order to achieve the best possible efficiency and to minimise heat losses. The operating characteristics are listed below.

- Defrost and settle time
- Power consumption of defrosting
- Heat energy utilised during defrosting

Main Observations of the Literature Study
The following is a list of the main observations found throughout the literature study.

- Frost formation decreases the heat capacity and COP of an ASHP (Don et al., 2011).
- Fin-and-tube heat exchangers have proved to perform better than microchannel heat exchangers for ASHP applications under frost conditions (Moallem et al., 2010) (Xu et al., 2012) (Padhmanabhan et al., 2008).
- Situations where the heat pump initiates a defrost cycle either too early or too late is known as mal-defrost phenomena (Wang et al., 2011).
- There are currently 13 control strategies, none of which can eliminate the occurrence of mal-defrost phenomena (Wang et al., 2011).

1.3 Frost Formation Phenomenon

As stated in Section 1.2, the frost formation occurs when the temperature of the evaporator surface is below the freezing point of water and below the dew-point temperature of the atmospheric air that passes through the evaporator. According to Cui et al. (2010), frost formation occurs in three characteristic periods; the crystal growth period, the frost growth period and the fully development period.

The Crystal Growth Period
At the first stage of the frost formation process, small water vapour droplets condensates or deposits from the atmospheric air flow onto the surface of the evaporator. This thin layer of ice acts as the core for further crystallisation of ice and frost. This initial process is known as nucleation. The frost layer grows and the crystals connects with their neighbouring crystals and forms a frost crystal layer which spreads in all directions. This period influences the further frost formation process significantly and the frost thickness increases and the surface becomes rough. (Cui et al., 2010)

The Frost Growth Period
In this period, the frost layer is characterised by growth of a porous layer where liquid water droplets, ice crystals and air molecules fills up the small gaps in the rough ice crystal layers. During this period, the major part of the mass transferred from the atmospheric air to the frost layer contributes to increasing the density rather than increasing the thickness of the frost layer. (Cui et al., 2010)

The Fully Development Period
When the growth of frost develops, latent heat releases and increases the surface temperature of the frost layer. When the surface temperature reaches the melting point of water, the fully developed period occurs and the outer layers of frost will melt and penetrate the gaps in the porous layers underneath, until it reaches a colder surface where it re-freezes. The process of deposition, melting and re-freezing is cyclic and occurs until thermodynamic equilibrium is reached. In the fully developed period, the surface of the frost becomes more smooth. (Cui et al., 2010)

Frost growth is a complicated transient phenomenon in which heat- and mass transfer occurs simultaneously. Most studies conducted on the topic are performed for frost formation over a cold surface exposed to forced or free convective flow of atmospheric air. To illustrate this, frost on a flat plate is shown in Figure 1.3. (Prölss and Schmitz, 2006)

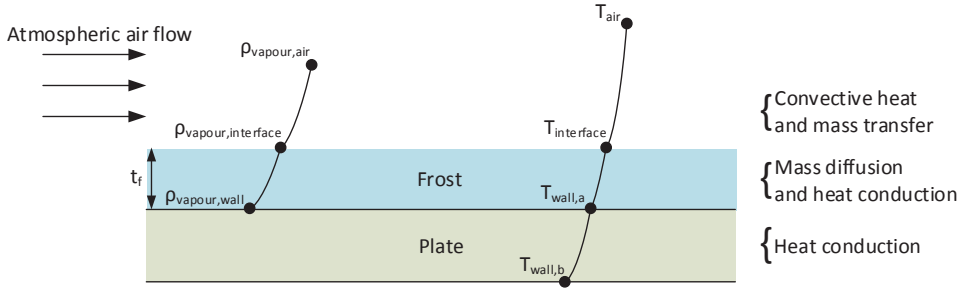

Figure 1.3. Frost deposition on a flat plate caused by an atmospheric airflow. (Prölss and Schmitz, 2006)

As shown in Figure 1.3, a flow of atmospheric air results in convective heat and mass transfer because of a temperature gradient from the air flow to the plate surface. This builds up the frost layer where mass diffusion and heat conduction occurs through the frost layer with the thickness t_f. Part of the water vapour freezes at the surface and increases the frost layer thickness while it releases latent heat. Mass diffusion occurs by means of water vapour diffusion through the pores in the porous frost layer, hence part of the water vapour contributes to densification of the frost layer. Heat conduction occurs through the plate as a result of the temperature difference on the plate walls. (Prölss and Schmitz, 2006)

The frost formation process has a great impact on the conductivity of the frost layer. The temperature at which the frost crystals form influences the type of crystal formation that formates and therefore also the conductivity of the frost layer. The shape and orientation of the frost crystals in the frost layer structure also has an impact on the frost conductivity. This makes it difficult to select an accurate correlation for the frost conductivity, which is why many different correlations have been proposed. (Sahin, 2000)

Chapter 2

Problem Statement

As stated in the previous sections, frosting of evaporator surfaces in ASHP applications is a well-known issue that manufacturers have to account for when developing the control strategy of the ASHP. The objective of such a control strategy is to minimise the amount of mal-defrost occurrences and thereby maximise the heat pump performance. Since it is difficult and impractical to measure the direct parameter, the frost thickness, control strategies are usually based on indirect parameters such as temperature, pressure and humidity.

DVI Energi, a Danish heat pump manufacturer, has agreed to provide a heat pump and facilities for test purposes, hence the project will be based on one of their products, the DVI LV9 Combi heat pump, which is an AWHP with a fin-and-tube evaporator. The DVI LV9 Combi heat pump uses a time initiated defrost cycle which is initiated once every hour, hence it has no control strategy that attempts to continuously assess the amount of frost on the evaporator. Therefore, the main objective of this project is:

To develop a reverse cycle defrost control strategy for an ASHP that can improve the performance of the DVI LV9 Combi heat pump compared to its current strategy.

The main objective is to be reached through the minor objectives listed below:

- Develop a model that can predict the amount of frost on the evaporator within an accepted error. This model is to be based on indirect parameters that are easily measured and thereby work as basis for a new control strategy. The model should be able to determine the optimal point of when to initiate the defrost process of the DVI LV9 Combi heat pump.
- Verify the model through experiments on the DVI LV9 Combi heat pump at varied ambient conditions using a climate chamber.
- Applying the developed control strategy to the DVI LV9 Combi heat pump and determine the performance of the developed control strategy and compare it to the original strategy.

This project will focus on the reverse cycle defrost method and a strategy for when to initiate the defrost process. Other ways to improve or perform the defrost process is not investigated further. During the project and experiments, the defrost process itself will be used the way it has already been programmed by DVI Energi and not altered in any way. Also the geometry and surface of the evaporator is not investigated further, despite research has revealed that these are important factors to consider in order to minimise frost formation.

Chapter 3

The DVI LV9 Combi Heat Pump

The configuration and design of the DVI LV9 Combi heat pump is presented in this chapter where the overall configuration of the components and the operation strategy is explained. The design of the evaporator is stated and geometrical parameters are described. Furthermore the control and defrost strategy is explained.

3.1 The DVI LV9 Combi Heat Pump Unit

The heat pump used for this project is delivered by the Danish heat pump manufacturer DVI Energi. The model is a DVI LV9 Combi, an AWHP with a rated heating capacity of 9 kW. The heat pump is build and sold as an all-in-one solution, completely equipped with a 300 litre storage tank and circulation pumps, making it easy to connect to an existing water and heating system of a house. The storage tank is divided into two parts and holds 250 litres of hot water for tap water use and 50 litres for space heating use. The heat pump configuration is illustrated in Figure 3.1 which shows all the components of the heat pump unit. The main components in the heat pump are the compressor (15), the condenser (11), the expansion valve (28) and the evaporator (10). Figure 3.1 is attached in large scale in the enclosure for convenience.

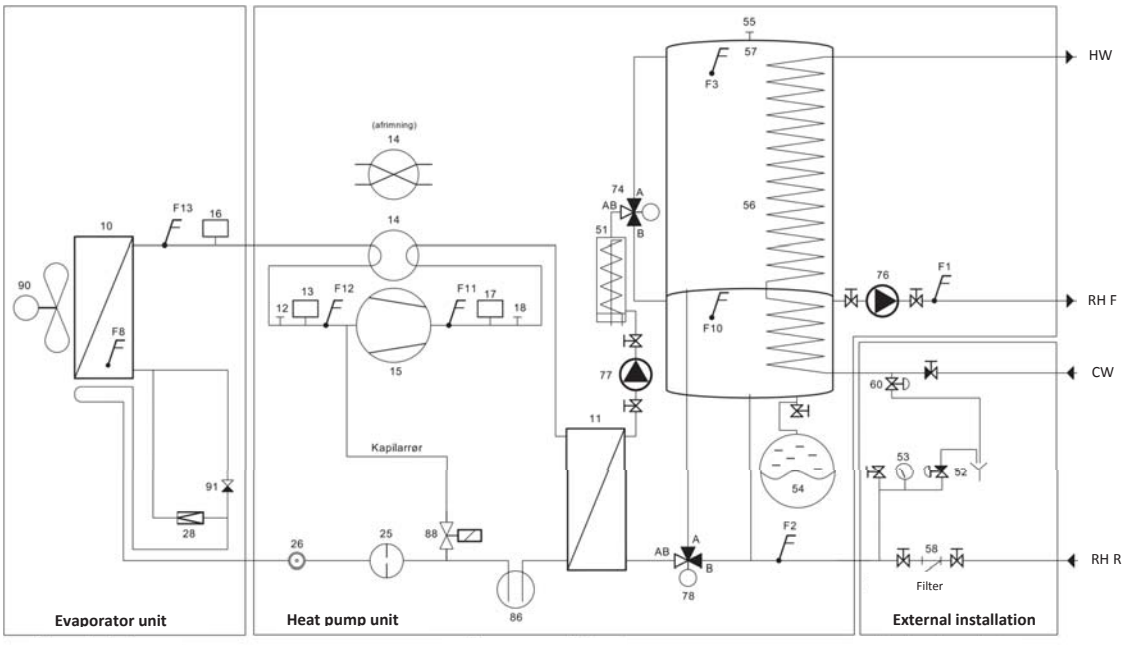

Figure 3.1. Process diagram of the DVI LV9 Combi heat pump (DVI Energi, 2014).

The heat pump uses R407c as refrigerant and a brief explanation of the properties of this refrigerant is given in Appendix B. In the heat pump cycle, the refrigerant is initially pressurized by the compressor (15), after which the temperature (F11) and pressure (17) are measured. The refrigerant then reaches a 4-way valve (14) which determines if the heat pump operates in normal or reversed mode. In case the heat pump operates normally, the refrigerant flows to the condenser (11) and exchanges heat to the central heating return water of the household. This is done with a brazed plate heat exchanger. After the condenser, the refrigerant reaches a receiver (86), a filter (25) and an inspection glass (26). The refrigerant is then passed through the gap between the bottom of the fins and the drain collector of the evaporator in order to keep the water in the drain collector from freezing. The refrigerant then reaches the expansion valve (28) where the refrigerant expands to a lower pressure and temperature. After the expansion valve, the refrigerant reaches the evaporator (10) to exchange heat with the ambient air. This is done by forcing air through the evaporator channels using a fan. On the DVI LV9 model this fan normally operates at 6.5 V as control signal, corresponding to 573 rpm. A temperature sensor (F8) is located on the evaporator surface, as well as at the evaporator outlet, to determine the current level of superheat. Also the pressure is measured (16) before the refrigerant returns to the compressor. The 4-way valve (14) operates in reversed mode when a defrost cycle is performed.

In connection with the heat pump cycle in Figure 3.1 is a storage tank (56), a circulation pump (77), an electrical heater (51), and two electrical 3-way valves (74, 78). The settings of the two 3-way valves determines if the heat pump produces heat for the central heating system or for tap water. Setting the valves to 74-B and 78-A will circuit water from the lower part of the storage tank through the condenser, while setting 74-A and 78-B will circuit water from the upper part of the storage tank through the condenser.

Some of the main components in the heat pump configuration are listed in Table 3.1.

Table 3.1. The main components of the DVI LV9 Combi heat pump.

Component	**No.**	**Manufacturer**	**Model**	**Notes**
Compressor	15	Danfoss	HHP038T4LC6	2900 rpm, 57 cm^3
4-way valve	14	Ranco	V6-412080100RV	
Condenser	11	Alfa Laval	CB62-50AH-F	A: 2.91 m^2
				U: 1072 W/(m^2K)
Expansion valve	28	Danfoss	ETS 6-18	Controller: EIM336
Evaporator	10	3T Ltd	DX-ST-3.2-890-800-5R-	A: 41.33 m^2
			8-S-Cu 0.30/Al 0.20	U: 33 W/(m^2K)
Evaporator fan	90	Ziehl-Abegg	FN063-ZII.DC.V7P2	6.5V, 573 rpm

In Table 3.1, the overall heat transfer coefficients, U, for condenser and evaporator, are given for the design operation of the heat pump. For the evaporator, this is specified to be at a rated capacity of 7.22 kW and at an air temperature of 15°C for a clean heat exchanger surface. For the condenser, this is specified at a capacity of 9 kW and at an inlet temperature of 75°C for a clean heat exchanger surface.

3.2 The DVI LV9 Combi Evaporator

The evaporator of the DVI LV9 Combi heat pump is a louvered fin-and-tube cross-flow heat exchanger which transfers heat from a forced air flow to the refrigerant in the heat pump cycle. It is manufactured by the British company Thermal Transfer Technology Limited (3T Ltd.) specifically for the DVI LV series. The evaporator is equipped with a 630 mm fan from the German manufacturer Ziehl-Abegg with a maximum capacity of 10,000 m^3/h. The fan speed is controlled by a 0-10V signal from the heat pump control, which can also be manually adjusted to avoid noise problems. The evaporator and the louvered fin-and-tube configuration are shown in Figure 3.2.

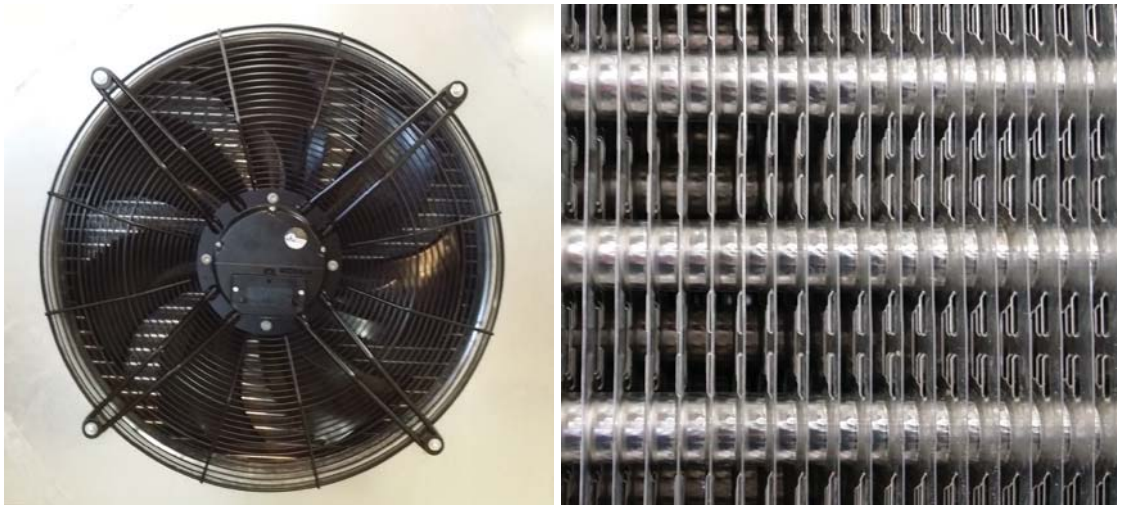

Figure 3.2. Left: The evaporator with the fan. Right: The louvered fin-and-tube configuration.

As seen in the right part of Figure 3.2, the evaporator fins have one-sided louvers which increase the heat transfer coefficient of the heat exchanger (Thulukkanam, 2013). Of practical reasons it has not been possible to determine the geometry of the louvers and they are therefore not considered further in the project. Geometrical specifications on the evaporator are listed in Table 3.2. (Thermal Transfer Technology Limited, 2014)

Table 3.2. Geometrical specifications on the DVI LV9 Combi evaporator. (Thermal Transfer Technology Limited, 2014)

Parameter	Value	Unit	Description
H_{eva}	800	mm	Evaporator height
L_{eva}	890	mm	Evaporator length
D_{eva}	100	mm	Evaporator depth
A_{eva}	41.33	m^2	Evaporator surface area
H_{fin}	800	mm	Fin height
D_{fin}	100	mm	Fin depth
t_{fin}	0.2	mm	Fin thickness
x_{fin}	3.1	mm	Distance between fins
n_{fin}	270	-	Number of fins
k_{fin}	205	W/(mK)	Fin conductivity (Aluminium)
L_{tube}	890	mm	Tube length
$D_{\text{tube,o}}$	9.5	mm	Tube outer diameter
$D_{\text{tube,i}}$	8.9	mm	Tube inner diameter
n_{tube}	160	-	Number of tubes
k_{tube}	401	W/(mK)	Tube conductivity (Copper)
S_{T}	24.90	mm	Transverse tube spacing
S_{L}	22.65	mm	Longitudinal tube spacing
S_{D}	25.85	mm	Diagonal tube spacing

A conceptual sketch of the fins and tubes in the evaporator is shown in Figure 3.3 from the front and from the side respectively.

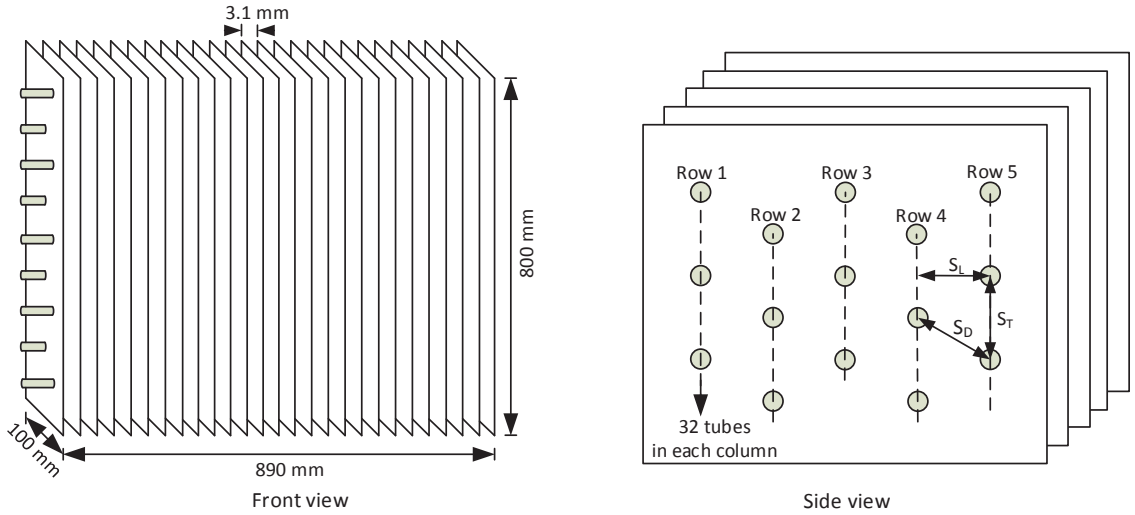

Figure 3.3. A conceptual sketch of the fins and tubes in the evaporator of the DVI LV9 Combi heat pump. Left: The evaporator fins from the front. Right: The evaporator fins from the side with the staggered tube configuration.

As seen in Figure 3.3, a fin in the evaporator is made up of one whole plate that has multiple tubes going through it. It is also seen how the tubes are arranged in a staggered grid with five tube rows of 32 tubes in each, yielding a total of 160 tubes.

The tubes are divided into six stacked vertical sections where the refrigerant is distributed in. Each section has its own inlet and outlet where the refrigerant flows through the staggered tube configuration. This is illustrated in Figure 3.4.

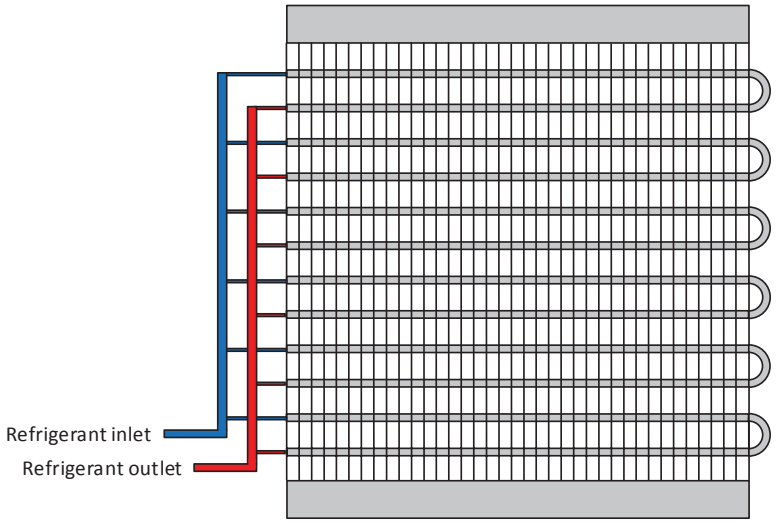

Figure 3.4. Illustration of the six stacked vertical sections that the refrigerant is distributed in.

3.3 Control and Defrost Strategy of the DVI LV9 Combi Heat Pump

The Danfoss compressor used in the DVI LV9 heat pump is of constant speed. This means that the heat pump is designed to on/off operation from a few parameters without any advanced variable control. However, an electronic expansion valve makes it possible to continuously adjust the opening degree of the valve in order to achieve optimal performance. Adjusting the opening degree affects the pressure and temperature on both sides of the heat pump cycle, and is therefore directly linked to the performance of the heat pump. The main control parameter is the level of superheat. Superheat is a measure of how much heat is added to the refrigerant after the phase change in the evaporator. The current level of superheat is determined by measuring the pressure in the evaporator, which determines the temperature of the phase change. This temperature is then compared to a measurement at the evaporator outlet. The difference between these two is usually preferred to be 5°C. From a performance perspective it is desired to have a low level of superheat. This is primarily because the refrigerant has better heat transfer properties when it is partly in the liquid state, compared to a pure gas state. However, it is necessary to have a high enough level of superheat to ensure only gas enters the compressor, since liquid refrigerant is damaging to the compressor parts and must be avoided.

Naturally, during a defrost cycle the valve controller is having difficulties controlling the level of superheat. Figure 3.5 shows a defrost cycle while logging the superheat reference (blue), current level of superheat (purple) and the valve opening degree (cyan).

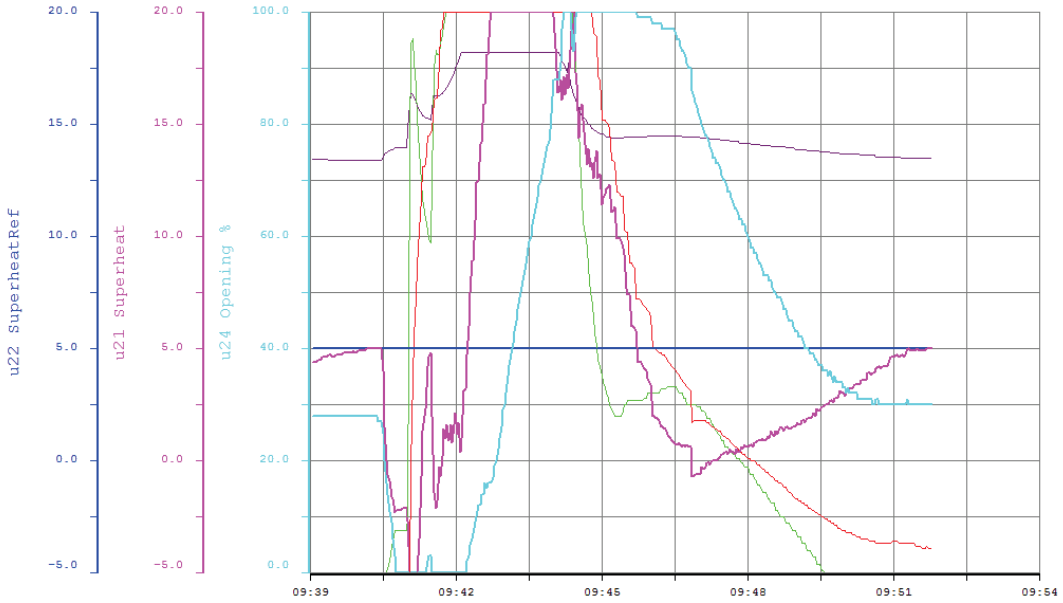

Figure 3.5. An example of the superheat level and valve opening degree during a defrost cycle. The relevant curves are: Superheat reference (blue), current level of superheat (purple) and valve opening degree (cyan).

As seen in Figure 3.5, the heat pump initially operates normally and the level of superheat lies close to the reference point. At this point the heat pump is stopped and the 4-way valve is reversed and defrosting is initiated which causes a sudden increase in the superheat. To avoid this, the controller opens the valve to 100% in order to increase the mass flow rate of refrigerant and reduce the superheat. After a few minutes the defrosting is complete and the 4-way valve is reversed back to normal position. The superheat decreases along with the valve opening degree until steady operation is reached.

Current Defrosting Strategy of the DVI LV9 Combi Heat Pump

DVI Energi has more than 30 years of experience in refrigeration systems. Traditionally BWHP has been their main focus, but in the last few years they have started to put more resources into ASHP units. So far they have not developed a successful control strategy that adapts the defrost process to the current environmental conditions. DVI Energi uses a time initiated and temperature terminated strategy, similar to strategy 10 as described in Section 1.2. Defrost mode is activated on the heat pump when the fin surface temperature is below 1°C. In defrost mode, a reverse cycle defrost process is initiated every 60 minutes and terminated when the surface temperature of the evaporator reaches 20°C. At this temperature it is assumed that all frost has melted and the evaporator is allowed to drain off for 90 seconds before returning to normal operation. During the defrost process the fan is switched off.

The defrost process is shown below as a stepwise procedure.

1. Check if fin temperature is less than or equal to 1°C.
2. If yes, start countdown timer from 60 minutes.
3. When countdown is finished, stop heat pump operation.
4. Reverse 4-way valve.
5. Start reverse heat pump operation and perform defrosting.
6. Check if evaporator surface temperature has reached 20°C.
7. If yes, stop heat pump operation.
8. Reverse 4-way valve and wait 90 seconds to allow water to drain off.
9. Start heat pump operation.

The strategy is not adjusted according to the given weather conditions, or any other varying parameters that might affect the formation of frost. Occasionally, some customers complain about noise from the evaporator fan, which is usually solved by reducing the fan speed. A reduction of the air flow means a reduced heat exchanging capacity which impacts the development of the frost layer. The fact that DVI Energi keeps the defrost cycle timer constant at 60 minutes is expected to cause a relatively high number of mal-defrost occurrences.

Chapter 4

Modelling of the DVI LV 9 Combi Heat Pump Cycle

The model of the DVI LV9 Combi heat pump cycle is presented in this chapter. The heat pump cycle is modelled in steady state in MATLAB. REFPROP is used in the MATLAB model as a calculation tool for thermodynamic properties for refrigerant, air, and water.

4.1 The DVI LV9 Combi Heat Pump Cycle

The DVI LV9 Combi heat pump utilises the energy in the ambient air from [7] to [8] and exchanges it to the refrigerant in the evaporator from [4] to [1]. The refrigerant is evaporated and superheated through the evaporator stage and afterwards compressed in a compressor stage from [1] to [2] where it reaches a high pressure and temperature. The refrigerant releases heat in the condenser from [2] to [3] which is exchanged to the accumulation tank from [5] to [6]. After the condenser stage, the refrigerant is throttled in an expansion valve to a lower pressure and temperature from [3] to [4] after which the operation cycle starts over. The heat pump cycle is illustrated in Figure 4.1. Figure 4.1 is attached in large scale for convenience.

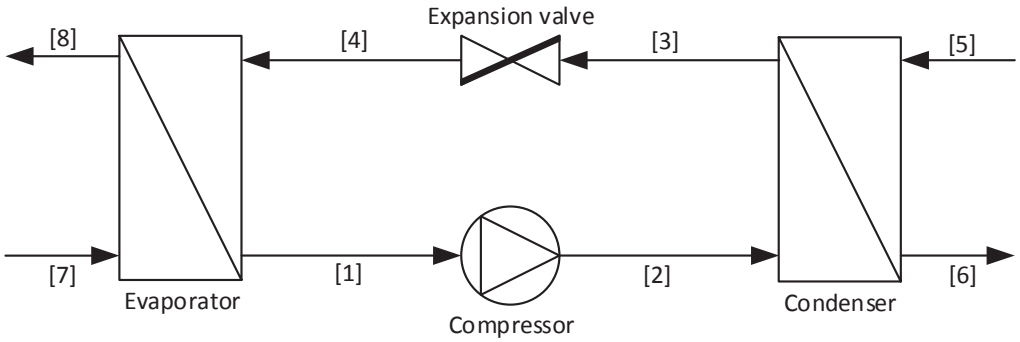

Figure 4.1. The basic concept of the operation cycle in the DVI LV9 Combi heat pump.

A set of input parameters are used in the heat pump cycle model. These are based on constants and empirical values obtained for rated performance of the DVI LV9 Combi heat pump. Since many of these input parameters change according to the given ambient conditions and operation conditions, the a set of typical input parameters are given in Table 4.1.

Table 4.1. Typical input parameters used in the model of the DVI LV9 Combi heat pump cycle.

Parameter	Value	Unit	Description
p_5, p_6, p_7	101.325	kPa	Pressure
$\dot{V}_5$, $\dot{V}_6$	823	L/h	Volumetric flow rate
Δp_{eva}	30	Pa	Pressure drop
x_1	1	-	Quality
x_3	0	-	Quality
T_5	35	°C	Temperature
T_7	-1	°C	Temperature
SH	6	°C	Level of superheat
SC	3	°C	Level of subcooling
ET	-8	°C	Evaporation temperature
CT	39	°C	Condensation temperature

The pressure drop across the evaporator is set to 30 Pa which is the rated pressure drop of the evaporator according to the manufacturer. The volumetric flow rate, $\dot{V}_7$, is found using the performance curve of the fan on the evaporator, which yields a flow of approximately 1.36 m^3/s. The pressure of the air flow at the outlet of the evaporator, p_8, is given as p_7-Δp_{eva} which yields a pressure of 101.295 kPa at rated performance.

The inlet temperatures, T_5 and T_7, and the flow rate, $\dot{m}_5$, can be varied and set to a given heat production and ambient situation both in the heat pump model and in the experiments performed on the DVI LV9 Combi heat pump.

Mass and energy must be conserved in the heat pump model at steady state operation, hence this is governed by mass and energy balance equations. The mass balances are given in Equation (4.1) and Equation (4.2).

$$\dot{m}_4 + \dot{m}_7 = \dot{m}_1 + \dot{m}_8 \qquad [\text{kg/s}] \quad (4.1)$$

$$\dot{m}_2 + \dot{m}_5 = \dot{m}_3 + \dot{m}_6 \qquad [\text{kg/s}] \quad (4.2)$$

Where:
$\dot{m}$ is mass flow rate [kg/s]

Initially the heat pump model is calculated without accounting for frost formation on the evaporator surface. Therefore $\dot{m}_7$ is set equal to $\dot{m}_8$. When accounting for frost formation on the evaporator surface, the mass flow rate of frost formation will be subtracted from $\dot{m}_7$.

The energy balances are given in Equation (4.3) and Equation (4.4).

$$\dot{m}_4 \cdot h_4 + \dot{m}_7 \cdot h_7 = \dot{m}_1 \cdot h_1 + \dot{m}_8 \cdot h_8 \qquad [\text{W}] \quad (4.3)$$

$$\dot{m}_2 \cdot h_2 + \dot{m}_5 \cdot h_5 = \dot{m}_3 \cdot h_3 + \dot{m}_6 \cdot h_6 \qquad [\text{W}] \quad (4.4)$$

Where:
h is enthalpy [kJ/kg]

4.2 Modelling of Components in the DVI LV9 Combi Heat Pump

The modelling of the main components in the heat pump cycle is explained in this section. The components considered are the compressor, the condenser, the expansion valve and the evaporator. The components are modelled in steady state using an iteration procedure.

Iteration Procedure

The numerical model of the heat pump cycle and the main components is performed using an iteration procedure to ensure that convergence is obtained. The iteration procedure is performed using a start guess on the refrigerant mass flow rate, $\dot{m}_{\mathrm{r}}(x)$, to the time x. With the start guess, calculations are performed on the heat pump cycle and the mass flow rate of refrigerant is calculated in the end of the calculation routine. The new value of the refrigerant mass flow rate, $\dot{m}_{\mathrm{r}}(x+1)$, is updated and used in the next iteration. This is done until a residual error is within the tolerance of 0.001 which is the difference in refrigerant mass flow rate in iteration $x = n$ and iteration $x = n - 1$. The iteration procedure is illustrated in the flow diagram in Figure 4.2.

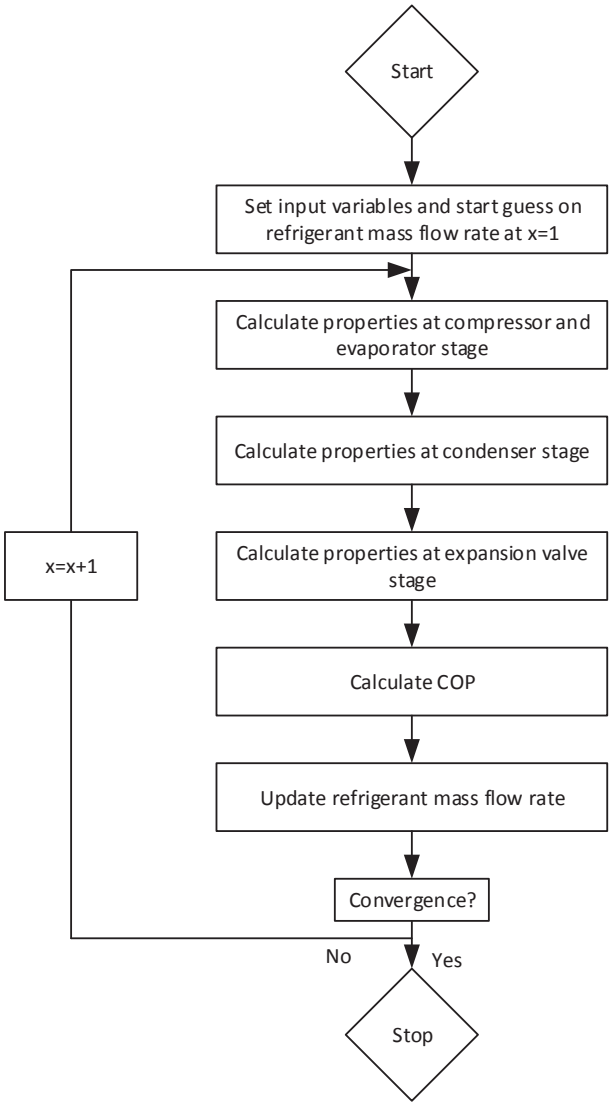

Figure 4.2. The iteration procedure for the heat pump cycle.

Compressor and Evaporator
The compressor used in the DVI LV9 Combi heat pump is a Danfoss scroll compressor with constant speed. Initially the evaporation and condensation temperatures are used to determine the electricity consumption and heat capacity of the compressor, P_{comp} and Q_{cond}, which are looked up in the data sheet for the compressor and used as input variables. A function is made in MATLAB for looking up these properties as function of evaporation and condensation temperature in order to be able to run the model at values not given in the data sheet. The function is shown below and is valid for evaporation temperatures in the range of -25°C to 15°C and for condensation temperatures in the range of 35°C to 65°C.

$$P_{\text{comp}}, Q_{\text{cond}} = f(ET, CT)$$

The function is made in MATLAB using the *meshgrid* and *griddata* functions.

The compressor stage is modelled by setting an evaporation temperature, ET, corresponding to the expected average evaporation temperature. Knowing the evaporation temperature and quality, $x_1 = 1$, at this point yields the enthalpy and temperature of saturation which are calculated using REFPROP.

The temperature at the inlet to the compressor is superheated with approximately 6°C in order to avoid any liquid refrigerant entering the compressor which can be damaging to it. The opening degree on the expansion valve is controlled and determines the level of superheat after the evaporator. The temperature at [1] is therefore modelled as in Equation (4.5).

$$T_1 = T_{\text{sat,eva}} + SH \qquad [^\circ\text{C}] \quad (4.5)$$

Where:
T_1 is temperature at compressor inlet [°C]
$T_{\text{sat,eva}}$ is saturation temperature at evaporator [°C]
SH is level of superheat [°C]

The pressure and entropy at [1] are calculated for the saturation temperature and the quality. The enthalpy is calculated using the pressure and the temperature at [1].

In order to determine thermodynamic properties at [2], an isentropic compression over the compressor is assumed, yielding that the entropy, $s_{s,2}$, is equal to the entropy, s_1. The enthalpy, $h_{s,2}$, is calculated using REFPROP for the entropy, $s_{s,2}$, and the pressure at [2]. Using the start guess value for the refrigerant mass flow rate and the electricity input to the compressor from the data sheet provided from Danfoss, the enthalpy can be calculated. This is done using Equation (4.6).

$$h_2 = \frac{P_{\text{comp}}}{\dot{m}_{\text{r}}} + h_1 \qquad [\text{kJ/kg}] \quad (4.6)$$

The pressure at [2] is calculated for the condensation temperature and a quality of $x = 0.5$. This is done assuming that the temperature glide is linear from $x = 0$ to $x = 1$, yielding that the average saturation pressure is at $x = 0.5$. In reality there will be a variation on a few degrees between the saturation points due to zeotropic mixing. This is further elaborated

in Appendix B. Knowing the enthalpies at [1] and [2], the compressor efficiency can be calculated as given in Equation (4.7).

$$\eta_{\text{comp}} = \frac{h_{s2} - h_1}{h_2 - h_1} \quad [\text{-}] \quad (4.7)$$

The temperature at [2] is looked up using the enthalpy and pressure.

The heat transfer rate in the evaporator is calculated using the enthalpy difference over the refrigerant flow as shown in Equation (4.8).

$$\dot{Q}_{\text{eva}} = \dot{m}_{\text{r}}(h_1 - h_4) \quad [\text{W}] \quad (4.8)$$

Condenser
The condenser is a brazed plate counter-flow heat exchanger where the refrigerant exchanges heat with water. The saturation enthalpy and temperature, $h_{\text{sat,cond}}$ and $T_{\text{sat,cond}}$, at the condenser stage are found using the pressure, p_3, and the quality, $x_3 = 0$. The temperature at [3] is calculated using the level of subcooling, as shown in Equation (4.9).

$$T_3 = T_{\text{sat,cond}} - \text{SC} \quad [^\circ\text{C}] \quad (4.9)$$

Where:
T_3 is temperature at condenser outlet [°C]
$T_{\text{sat,cond}}$ is saturation temperature at condenser [°C]
SC is level of subcooling [°C]

The enthalpy and entropy at [3] are calculated using the pressure, p_3, and the temperature, T_3.

Expansion Valve
The expansion valve is modelled assuming an isenthalpic process, hence h_3 is set equal to h_4. With the enthalpy and pressure known at [4], other thermodynamic properties can be found using REFPROP.

4.3 Initial Results for the Heat Pump Cycle

Initial results for the heat pump cycle, before frost formation is considered on the evaporator surface, are given for the conditions set in Section 4.1. With these settings, thermodynamic properties are calculated in the model which are given in Table 4.2. The numeration in this section corresponds to the one given for the heat pump cycle shown in Figure 4.1 in Section 4.1.

Table 4.2. Thermodynamic properties calculated for the heat pump cycle.

Point	Temperature [°C]	Enthalpy [kg/kJ]	Entropy [kJ/(kgK)]	Pressure [kPa]
[1]	-3.00	409	1.78	344
[2]	77.05	466	1.78	1603
[3]	33.50	249	1.16	1603
[4]	-12.57	249	1.19	344
[5]	35.00	146	0.50	101
[6]	43.30	181	0.61	101
[7]	-1.00	398	3.78	101
[8]	-4.45	394	3.77	101

The initial results for the heat pump cycle without frost on the evaporator are used as reference for the model of the frost formation. The heat pump cycle is updated in each iteration step as the frost layer builds up.

The heat pump cycle is illustrated on a log p-h diagram in Figure 4.3.

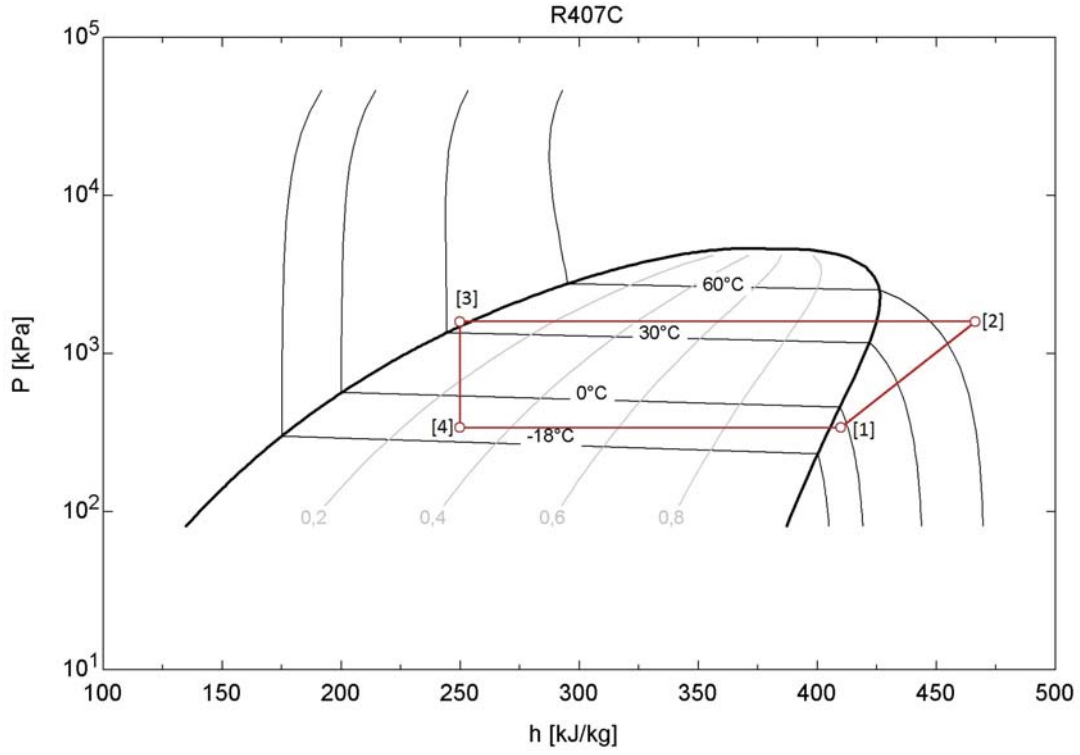

Figure 4.3. The heat pump cycle in the DVI LV9 Combi heat pump on a log p-h diagram.

The heat pump cycle is shown in a T-s diagram in Figure 4.4.

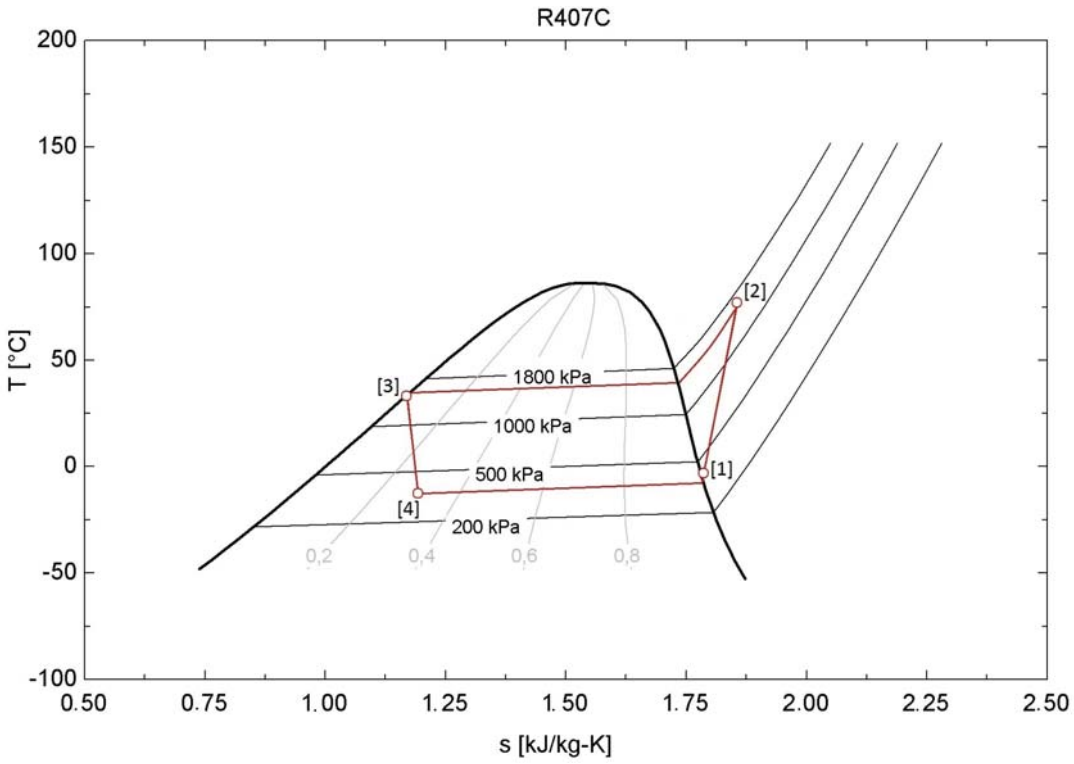

Figure 4.4. The heat pump cycle in the DVI LV9 Combi heat pump on a T-s diagram.

Chapter 5

Modelling of Frost Formation on the DVI LV9 Combi Evaporator

The model of the frost formation process on the DVI LV9 Combi evaporator is presented in this chapter. The modelling procedure and assumptions are initially presented where after the model is presented step by step for the different sub-models and model parts.

5.1 Modelling Procedure

The model of the frost formation is based on the model of the DVI LV9 Combi heat pump cycle, presented in Chapter 4, where properties such as temperatures, pressures and mass flows are used. Furthermore, the frost formation model is based on the geometry of the evaporator given in Section 3.2.

The frost formation model is initiated by calculating thermodynamic properties for the heat pump cycle in order to determine temperatures, pressures and other relevant properties in the cycle. With a reference point for the heat pump cycle, the frost model is initiated using a loop where a frost layer growth occurs on the frosted surface of the evaporator. This is done by setting frost properties to zero and calculating geometrical properties for the evaporator. The geometrical properties are found with no frost present and are used as an initial point to calculate flow properties for the air flow through the evaporator. Heat transfer coefficients, pressure drop, and flow properties are then calculated for the air flow. With known flow properties and geometrical properties, mass of frost is calculated for each time step, which allows for calculations of other frost properties and eventually a frost thickness. The frost thickness changes the geometrical properties and thereby the air flow properties, and gradually the growth of frost affects the performance of the evaporator.

A flow diagram of the model procedure is shown in Figure 5.1.

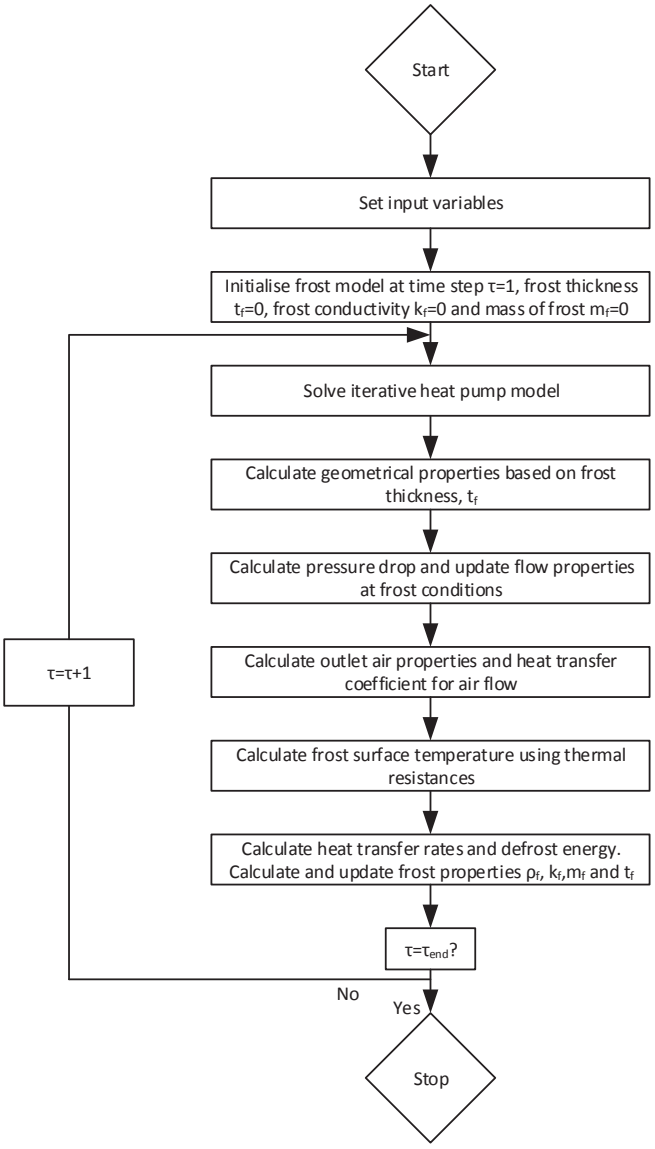

Figure 5.1. Flow diagram illustrating the modelling procedure for the frost formation on the evaporator surface.

The model is presented in the following sections in the order displayed below:

- Geometrical parameters
- Convective heat transfer coefficients
- Pressure drop and volume flow reduction through evaporator
- Surface efficiency
- Frost surface temperature
- Overall heat transfer coefficient and heat transfer rate
- Thermal properties for frost
- Sensitivity Analysis of properties for frost
- Determination of defrost time interval

5.2 Modelling Assumptions and Overview

Several assumptions are set for the modelling of frost formation on the evaporator surface in order to be able to perform systematic calculations on the process. These assumptions are presented in the following.

1. **Atmospheric air flow is assumed to be uniform**
   The atmospheric air flow is assumed to be uniform and equally distributed over the inlet of the evaporator. Gravity and compressibility of the air flow is neglected. In reality, the air flow distribution will not be uniform because the fan that forces the air flow through the evaporator is circular and the inlet to the evaporator is rectangular which causes a lower air flow rate in the corners of the evaporator inlet. Since the fan is a radial flow fan, there will also be a point in the middle of the evaporator where the air flow rate will be lower. The air flow will most likely also be influenced by the walls in the climate chamber which is relative small compared to having the evaporator placed outdoor. This means that the distribution of the air flow is expected to be non-uniform, but this is neglected for simplicity. Thermodynamic properties such as density and viscosity are also considered uniform.

2. **The frost formation process is considered uniform**
   The frost formation process is considered uniform so that the thickness of the frost layer is the same everywhere where frost is deposited. In reality, the frost formation will depend on local temperature variations on the evaporator surface and the air flow distribution through the evaporator. The geometry of the evaporator also affects the frost formation.

3. **The frost is assumed to deposit at the air outlet side of the evaporator**
   The frost is assumed to deposit on the outlet part of the evaporator where the air flow temperature is lowest. The lowest evaporator surface temperature is also obtained in the outlet air side of the evaporator, since this is where the refrigerant enters the evaporator and has the lowest temperature.

4. **Water vapour diffusion in the frost layer is neglected**
   Water vapour diffusion through the frost layer is neglected in the model of the frost formation process in order to simplify this. In reality there will be water vapour diffusion through the porous frost layer that will yield densification of the frost layer. All frost that formates on the evaporator surface is therefore assumed to contribute to increasing the frost layer.

5. **The frost density and conductivity are considered uniform and the surface properties are always valid for the complete layer**
   The density and conductivity of the frost layer are considered uniform although there will be a variation of these parameters through the frost layer in reality. The density and conductivity will depend on the porosity and frost formation process of the frost layer as described in Section 1.3. Because the frost layers in this project will always be relatively thin, the properties calculated at the frost surface is assumed to be valid for the complete layer.

6. **The frost temperature gradient through the frost layer is assumed linear**
   The frost temperature gradient through the frost layer between the evaporator surface temperature and the frost surface temperature is assumed to be linear. This temperature gradient will not be linear in reality since the conductivities for the evaporator surface and the air flow are different. The conductivities for the tubes and fins, which are manufactured in copper and aluminium respectively, are higher than the conductivity of air, hence the frost temperature will be more affected by the fins and tubes than the air flow.

7. **Water that drains of the evaporator is assumed to be 4°C in average**
   During a defrost process, frost melts to water. It is assumed that the water that drains of the evaporator is heated to 4°C in average. This is based on measurements during experiments where the water temperature is measured continuously during the defrost process which occurs until the evaporator surface temperature is 20°C.

8. **Refrigerant is equally distributed in the evaporator tubes**
   The refrigerant is assumed to be equally distributed in the refrigerant tubes. The mass flow rate of refrigerant is therefore assumed to be the same in all tubes and it is assumed that there is an equal pressure distribution in all tubes.

5.3 Modelling of Geometrical Parameters

When the air flow enters the evaporator, the flow is separated into the narrow channels between the fins. As it travels through these channels it encounters the staggered grid of tubes with cold refrigerant flowing inside, hence some geometrical parameters, such as the hydraulic diameter, will vary throughout the channel. This is dealt with in this section. The surface area where frost is deposited is on is calculated in this section as well.

To account for the refrigerant tubes being at different locations, the depth of the channel is divided into 10,000 vertical columns, giving each column a width of 0.01 mm. The number of vertical columns is chosen as a trade off between accuracy and simulation time. Each vertical column is given a coordinate, x, where $x = 1$ corresponds to the first column, $x = 2$ is the second, and $x = n$ is the last column. This is illustrated in Figure 5.2.

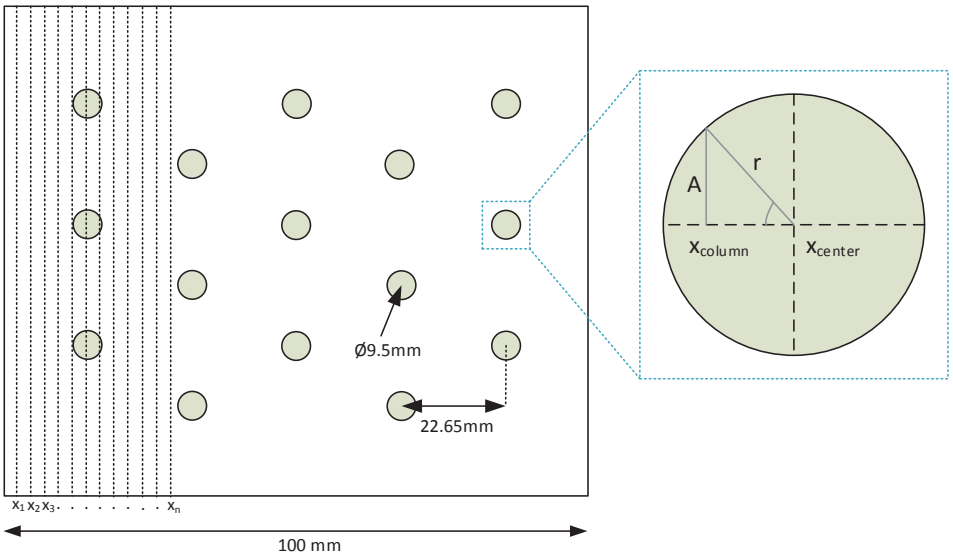

Figure 5.2. The depth of the evaporator channel is divided into 10,000 vertical columns with a with of 0.01mm and numerated $x = [1, 2, 3, 4...n]$.

The purpose of this approach is to consider each x-column individually hence allowing calculations on small sections of the evaporator.

Varying the area of frost

When performing the calculation routine in the frost formation model, the frost thickness, t_f, will be calculated from the mass of frost, the frost density, and the area that the frost is distributed over. It is therefore necessary to calculate geometrical properties in the part of the evaporator where frost is deposited. Therefore a function to determine this area is called during the calculation routine. This is done using a coordinate, x_f, which is where the frost formation is assumed to start. This is illustrated in Figure 5.3

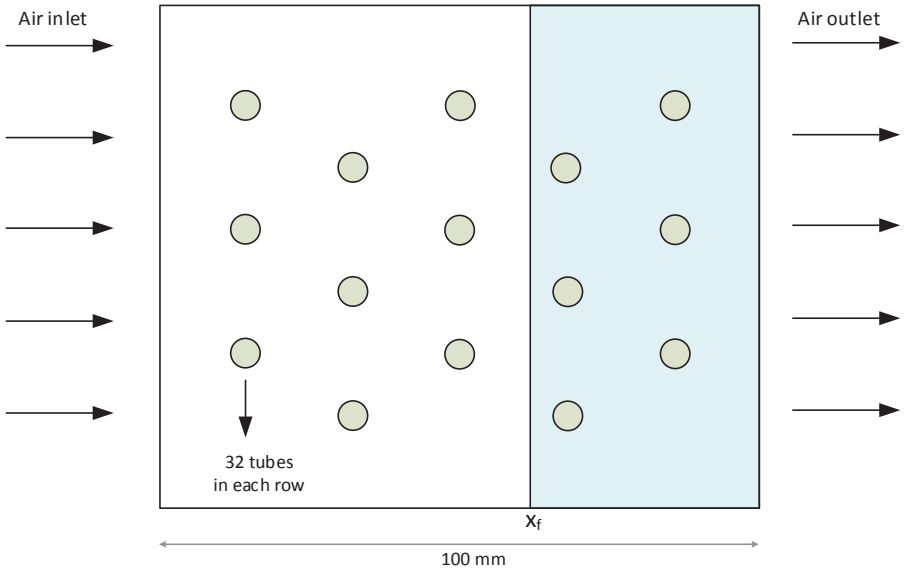

Figure 5.3. Illustration of how the frost area is determined using the coordinate x_f. The frosted area is illustrated with a blue colour.

As illustrated in Figure 5.3, the frosted area of the evaporator is set to start at x_f and continue until the evaporator outlet. The frost development is expected to be more severe at the outlet of the evaporator than at the inlet due to the dynamic effects in the frost formation process. Observations from experiments with the DVI LV9 Combi heat clearly show that more frost is deposited at the outlet of the evaporator than at the inlet. Several factors have influence on where the frost deposition occurs. The effects that might have influence on the frost formation process are given in the following.

- *Flow conditions*
  The air flow conditions at the inlet and through the evaporator are expected to affect the point where frost will begin to develop. Dynamic parameters like turbulence, shear stress, and development of boundary layer are expected to influence the frost process.

- *Surface conditions*
  The conditions of the surface where frost develops influences the frost process. A wet or dry surface will have different properties and is expected to have influence on the frosting process. The local temperature of the evaporator surface will affect the cooling of the air flow and therefore have an influence on where the frost formation will occur. The local surface temperature is affected by the pattern in which the refrigerant enters and exits the tubes in the evaporator. The refrigerant enters the tubes located closest to the air outlet side and exits in the tubes located closest to the air inlet side, hence the refrigerant is coldest near the outlet, which yields a colder surface temperature in this part of the evaporator.

- *Phase change conditions*
  In order for frost to deposit on the surface, a phase change must occur and latent heat must be released in the exothermic deposition process. For frost to deposit, the air flow must be cooled substantially below 0°C in order for nucleation to occur. Nucleation is the process by which a minimum crystal structure can be formed to be the basis of further frost growth. (Cui et al., 2010)

In the example shown in Figure 5.3, the point x_f is set at 60 mm which corresponds to the x-column equal to 6000. With this assumption it is possible to vary and calculate the total frosted surface area from x_f to the outlet of the evaporator. This is done by considering the fins and tubes separately as given in Equation (5.1).

$$A_{\text{eva,f}} = A_{\text{fin,f}} + A_{\text{tube,f}} \qquad \left[\text{m}^2\right] \quad (5.1)$$

Where:
$A_{\text{eva,f}}$ is the frosted evaporator surface area $[\text{m}^2]$
$A_{\text{fin,f}}$ is the frosted fin surface area $[\text{m}^2]$
$A_{\text{tube,f}}$ is the frosted tube surface area $[\text{m}^2]$

The surface area of the fins is calculated as a rectangle where the holes for the refrigerant tubes is subtracted before multiplying by the amount of sides and fins. If a frost layer is present, the thickness is added to the radius of the holes. This is given in Equation (5.2).

$$A_{\text{fin,f}} = H_{\text{fin}}(D_{\text{fin}} - x_f) - ((r_{\text{tube,o}} + t_f)^2 \pi n_{\text{tube}}) \qquad \left[\text{m}^2\right] \quad (5.2)$$

Where:
H_{fin} is the fin height [m]
D_{fin} is the fin depth [m]
x_{f} is the distance from the point where frost starts to deposit to the evaporator outlet [m]
$r_{\text{tube,o}}$ is the tube outer radius [m]
t_{f} is the frost thickness [m]
n_{tube} is the number of tubes through the fin [-]

Because of the possibility that the x_{f}-column is located on a row of tubes, it is necessary to perform this calculation in an *if* statement. This statement takes the location of x_{f} into account and subtracts the correct area of tube holes from the fin area.

Within the same statement, the surface area of the tubes is calculated. In case a layer of frost is present, the frost thickness is added to the radius of the tubes. This is given in Equation 5.3.

$$A_{\text{tube,f}} = 2(r_{\text{tube,o}} + t_{\text{f}})\pi L_{\text{tube}} n_{\text{tube}} \qquad \left[\text{m}^2\right] \quad (5.3)$$

Where:
L_{tube} is the tube length [m]
n_{tube} is the number of tubes [-]

Calculation of Hydraulic Diameter
When the air travels through the evaporator channels it will encounter the refrigerant tubes, which will occupy, and thereby block, some of the space. This leads to a reduction of the hydraulic diameter every time the air flow passes one of the five rows of tubes. This is accounted for by the approach of dividing the depth of the channel into vertical columns as illustrated in Figure 5.2. In this case each x-row is assigned a x-value corresponding to the total height that is blocked by the refrigerant tubes. The hydraulic diameter is then calculated for each row while considering the diameter of the tubes, and if there is frost on the tube surface this is assumed to block the air flow, hence the thickness is added to the tube diameter. The hydraulic diameter for each of the 10,000 x-rows is calculated as shown in Equation (5.4).

$$D_{\text{h}} = \frac{2ab}{a+b} \cdot n_{\text{channels}} = \frac{2(H_{\text{fin}} - H_{\text{blocked}})(x_{\text{fin}} - 2t_{\text{f}})}{(H_{\text{fin}} - H_{\text{blocked}}) + (x_{\text{fin}} - 2t_{\text{f}})} \cdot n_{\text{channels}} \qquad [\text{m}] \quad (5.4)$$

Where:
D_{h} is the hydraulic diameter [m]
H_{blocked} is the blocked height of the fin [m]
x_{fin} is distance between fins [m]
n_{channels} is the number of channels [-]

The blocked height of the fin, H_{blocked}, is only calculated if the current x-row is located upon a row of tubes, and otherwise set to zero. This is calculated as shown in Equation (5.5).

$$H_{\text{blocked}} = \sqrt{(r_{\text{tube,o}} + t_{\text{f}})^2 - (x_{\text{center}} \pm x_{\text{wall}})^2} \cdot 2n_{\text{tubes,row}} \qquad [\text{m}] \quad (5.5)$$

Where:
x_{center} is the x-coordinate of the relevant tube centre [m]
x_{wall} is the x-coordinate of the relevant tube wall [m]
$n_{\text{tubes,row}}$ is the number of tubes in a vertical row [-]

Performing this calculation for each row yields the hydraulic diameter shown in Figure 5.4.

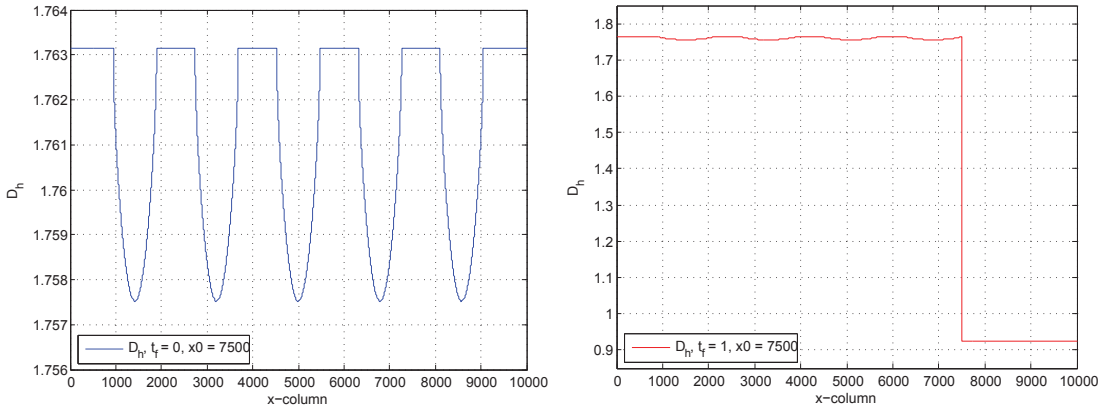

Figure 5.4. The variation in hydraulic diameter as the air travels through the evaporator. Blue is with no frost layer ($t_{\text{f}} = 0$) and red is with 1 mm of frost ($t_{\text{f}} = 0.001$). Notice the difference in the D_{h}-axes.

As seen in the right part of Figure 5.4, the hydraulic diameter is slightly lower at a row of tubes. As the frost is taken into account in the last part of the evaporator section, the hydraulic diameter drops. The hydraulic diameter used in the calculation procedure in the model is the mean of the hydraulic diameter values for all vertical columns.

5.4 Convective Heat Transfer Coefficients

The convective properties for the air flow and the refrigerant flow are modelled in order to determine the convective heat transfer coefficients for the two flows.

Refrigerant Flow
The Reynolds number for the refrigerant flow in the tubes is calculated based on the inner diameter of the tubes and is given in Equation (5.6). (Cengel et al., 2008)

$$\text{Re}_{D_{\text{t,i}}} = \frac{v_{\text{r}} D_{\text{tube,i}}}{\nu_{\text{r}}} \quad [\text{-}] \quad (5.6)$$

Where:
$\text{Re}_{D_{\text{tube,i}}}$ is Reynolds number of refrigerant flow [-]
v_{r} is flow velocity of refrigerant flow [m/s]
$D_{\text{tube,i}}$ is inner tube diameter [m]
ν_{r} is kinematic viscosity of refrigerant [m^2/s]

The Prandtl number is calculated for the refrigerant flow using Equation (5.7). (Cengel et al., 2008)

$$\mathrm{Pr_r} = \frac{\nu_\mathrm{r}}{\alpha_\mathrm{r}} \qquad [\text{-}] \quad (5.7)$$

Where:
$\mathrm{Pr_r}$ is Prandtl number for the refrigerant [-]
α_r is thermal diffusivity for the refrigerant $[\mathrm{m^2/s}]$

The Nusselt number for the refrigerant flow in the tubes is based on Gnielinski's equation which is given in Equation (5.8) for turbulent flow. (Cengel et al., 2008)

$$\mathrm{Nu_r} = \frac{(f_\mathrm{r}/8)(\mathrm{Re}_{D_\mathrm{tube,i}} - 1000)\mathrm{Pr_r}}{1 + 12.7(f_\mathrm{r}/8)(\mathrm{Pr_r}^{2/3} - 1)} \qquad [\text{-}] \quad (5.8)$$

Where:
$\mathrm{Nu_r}$ is Nusselt number for refrigerant flow [-]
f_r is a friction factor for the refrigerant flow [-]

Gnielinski's equation is valid for turbulent flow in a tube for Reynolds numbers in the range of $3{\cdot}10^3$ to $5{\cdot}10^6$ and Prandtl numbers in the range of 0.5 to 2000. The friction factor f_r can be determined with different appropriate relations where the first Petukhov equation is chosen which is given in Equation (5.9). (Cengel et al., 2008)

$$f_\mathrm{r} = (0.790\ln(\mathrm{Re}_{D_\mathrm{tube,i}}) - 1.64)^{-2} \qquad [\text{-}] \quad (5.9)$$

The Nusselt number is used to calculate the convective heat transfer coefficient for the refrigerant flow in the tubes, which is given in Equation 5.10. (Cengel et al., 2008)

$$h_\mathrm{r} = \frac{\mathrm{Nu_r} k_\mathrm{r}}{D_\mathrm{tube,i}} \qquad \left[\mathrm{W/(m^2K)}\right] \quad (5.10)$$

Where:
h_r is convective heat transfer coefficient for refrigerant flow $[\mathrm{W/(m^2K)}]$
k_r is thermal conductivity of refrigerant flow [W/(mK)]

Air Flow
The Reynolds number for the air flow through the evaporator is calculated based on the hydraulic diameter and the flow velocity and is given in Equation (5.11).

$$\mathrm{Re}_{D_\mathrm{h}} = \frac{\nu_\mathrm{a} D_\mathrm{h}}{\nu_\mathrm{a}} \qquad [\text{-}] \quad (5.11)$$

Where:
$\mathrm{Re}_{D_\mathrm{h}}$ is Reynolds number for the air flow through the evaporator [-]
D_h is hydraulic diameter [m]
V_a is air flow velocity [m/s]
ν_a is viscosity of air $[\mathrm{m^2/s}]$

The Reynolds number over a tube is calculated using the outer tube diameter which is given in Equation (5.12). (Rohsenow et al., 1998)

$$\mathrm{Re}_{D_{\mathrm{tube,o}}} = \frac{\nu_{\mathrm{a}}(D_{\mathrm{tube,o}} + 2t_{\mathrm{f}})}{\nu_{\mathrm{a}}} \quad [-] \quad (5.12)$$

Where:
$\mathrm{Re}_{D_{\mathrm{tube,o}}}$ is Reynolds number over a tube [-]
$D_{\mathrm{tube,o}}$ is the outer tube diameter [m]

In order to calculate the Nusselt number for the air flow, the Colburn j-factor must be found using Equation (5.13). (Rohsenow et al., 1998)

$$j = 0.14\mathrm{Re}_{D_{\mathrm{tube,o}}}^{-0.328}(\mathrm{S_T}/\mathrm{S_L})^{-0.502}\pi^{0.031} \quad [-] \quad (5.13)$$

Where:
j is Colburn j-factor for air flow through evaporator [-]
S_{L} is longitudinal tube spacing [m]
S_{T} is transverse tube spacing [m]

The Colburn j-factor is a dimensionless parameter that describes the ratio of convection heat transfer (per unit duct surface area) to the amount of virtually transferable (per unit of flow cross-sectional area). It is a modified version of the Stanton number where changes in Prandtl number is taken into account. In other words, the Colburn j-factor is a measure of how much convective heat transfer that occurs from the air flow to the evaporator surface per unit area, compared to the heat capacity of the air flow. The Colburn j-factor used in Equation (5.13) is suggested by Gray and Webb and is valid for plain fins on a staggered tube bank for four or more rows of tubes (Rohsenow et al., 1998).

The Prandtl number is calculated for the air flow using Equation (5.14). (Cengel et al., 2008)

$$\mathrm{Pr}_{\mathrm{a}} = \frac{\nu_{\mathrm{a}}}{\alpha_{\mathrm{a}}} \quad [-] \quad (5.14)$$

Where:
Pr_{a} is Prandtl number for the air flow [-]
α_{a} is thermal diffusivity for the air flow [m^2/s]

The Nusselt number for the air flow through the evaporator is found using Equation (5.15).

$$\mathrm{Nu}_{\mathrm{a}} = j\mathrm{Re}_{D_{\mathrm{h}}}\mathrm{Pr}_{\mathrm{a}}^{1/3} \quad [-] \quad (5.15)$$

Where:
Nu_{a} is Nusselt number for air flow though evaporator [-]

The convective heat transfer coefficient for the air flow is calculated using Equation (5.16).

$$h_{\mathrm{a}} = \frac{\mathrm{Nu}_{\mathrm{a}}k_{\mathrm{a}}}{D_{\mathrm{h}}} \quad \left[\mathrm{W}/(\mathrm{m}^2\mathrm{K})\right] \quad (5.16)$$

Where:
h_a is convective heat transfer coefficient for air flow [W/(m^{2}K)]
k_a is conductivity for air flow [W/(mK)]

The convective heat transfer coefficients are used to model the overall heat transfer coefficient.

5.5 Pressure Drop and Volume Flow Reduction Through Evaporator

When the forced air flow passes through the evaporator, a pressure drop occurs. The pressure drop is related to the volumetric flow rate of air which is forced through the evaporator by a fan as stated in Section 3.2. In order to determine the pressure drop through the evaporator, the performance curves for the fan must be used. A correlation for pressure drop as function of volumetric flow rate at different fan speeds is provided by the fan manufacturer Ziehl-Abegg. This correlation is used to find a volumetric flow rate, and thereby a mass flow rate, at a given pressure drop.

The pressure drop through the evaporator is calculated based on a friction factor recommended for flow normal to tube banks of finned tubes by Kays and London (1984). The friction factor is assumed to be constant for the evaporator channels and chosen at a Reynolds number of 1,000. This value is chosen based on a calculated Reynolds number for one channel using Equation (5.11) from Section 5.4. The friction factor is equal to 0.0379 at these conditions. The pressure drop is calculated using Equation (5.17). (Kays and London, 1984)

$$\Delta p = \frac{G_{max}^2}{2\rho_{a,in}} \left[(1+\sigma_{area}^2) \left(\frac{\rho_{a,in}}{\rho_{a,out}} - 1 \right) + f \frac{A_{eva}}{A_{min}} \frac{\rho_{a,in}}{\rho_{a,m}} \right] \quad \text{[Pa]} \quad (5.17)$$

Where:
Δp is pressure drop [Pa]
G_{max} is mass velocity at maximum air velocity [kg/(m^2 s)]
$\rho_{a,in}$ is the density of air at the inlet to the evaporator [kg/m^3]
$\rho_{a,out}$ is the density of air at the outlet to the evaporator [kg/m^3]
$\rho_{a,m}$ is the mean density of in- and outlet of the air flow [kg/m^3]
σ_{area} is area ratio [-]
f is friction factor [-]
A_{eva} is evaporator surface area [m^2]
A_{min} is minimum free-flow area [m^2]

The maximum air velocity, $v_{a,max}$, used to calculate the maximum mass velocity, is calculated as given in Equation (5.18).

$$v_{a,max} = \frac{S_T}{S_T - (D_{tube,o} + 2t_f)} v_a \quad \text{[m/s]} \quad (5.18)$$

This correlation is valid for a tube bank with staggered grid where $S_D > (S_T + D_{tube,o})/2$.

Where:
S_D is diagonal tube spacing [m]

The minimum free-flow area, A_{min}, is calculated based on the geometry of the evaporator and is given in Equation (5.19).

$$A_{\text{min}} = (H_{\text{fin}} - n_{\text{tubes,row}} D_{\text{tube,o}} + 2t_{\text{f}})(L_{\text{eva}} - n_{\text{fin}} t_{\text{fin}}) \qquad \left[\text{m}^2\right] \quad (5.19)$$

The area ratio, σ_{area}, is calculated as the ratio of the minimum free-flow area, A_{min}, and the frontal area, A_{fr}.

The frontal area is calculated using Equation (5.20).

$$A_{\text{fr}} = (H_{\text{fin}} L_{\text{eva}}) - (H_{\text{fin}} t_{\text{fin}} n_{\text{fin}}) \qquad \left[\text{m}^2\right] \quad (5.20)$$

Using this relation for the pressure drop yields that entrance and exit effects are included in the friction factor. (Kays and London, 1984)

The correlation provided by Ziehl-Abegg is used to relate the pressure drop to the volumetric flow rate. The different performance curves are shown in Figure 5.5.

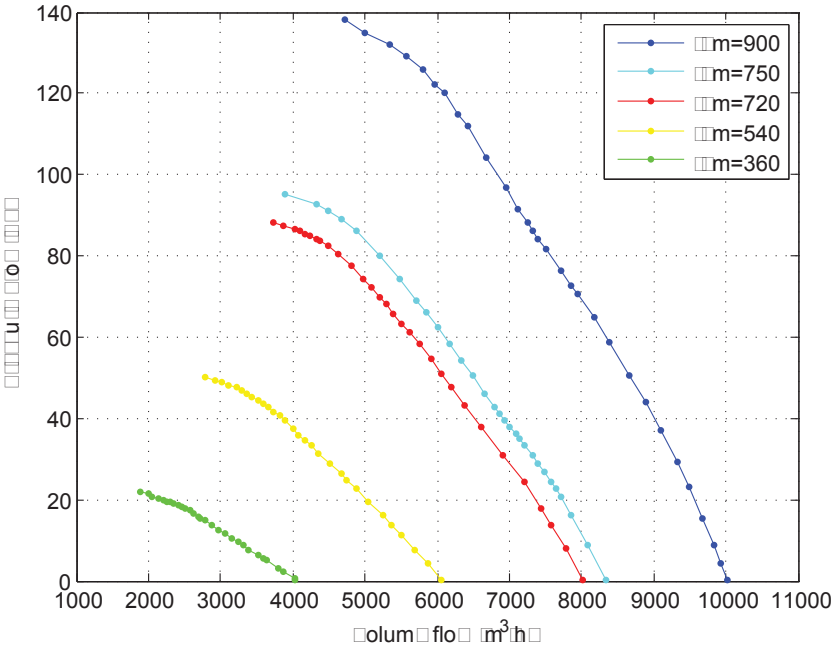

Figure 5.5. Performance curves for pressure drop as function of volumetric flow rate for the Ziehl-Abegg fan at different fan speeds (Ziehl-Abegg, 2013).

In order to determine the volumetric flow rate based on the calculated pressure drop, the curves in Figure 5.5 are interpolated using MATLAB's *meshgrid* function for the data points. This is shown in Figure 5.6.

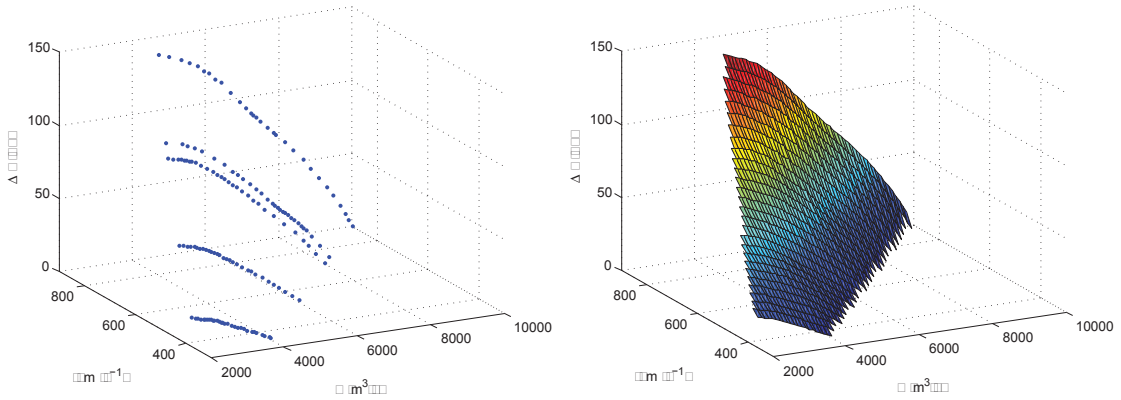

Figure 5.6. Left: The correction factor data points. Right: The created mesh using MATLAB's *meshgrid* function.

With the mesh for the fan correlation, the value for the volumetric flow rate, $\dot{V}$, can be determined using MATLAB's *griddata* function.

With this correlation between pressure drop and volumetric flow rate, it is possible to calculate a new volumetric flow rate at each time step, τ. This is done as frost formates on the evaporator surface area which gradually blocks the free air flow and reduces the volumetric flow rate. With the volumetric flow rate known at each time step, the mass flow rate is calculated using Equation (5.21).

$$\dot{m} = \dot{V}\rho_{\mathrm{a,m}} \qquad \left[\mathrm{kg/s}\right] \quad (5.21)$$

Where:
$\rho_{\mathrm{a,m}}$ is mean air flow density between inlet and outlet of the evaporator $[\mathrm{kg/m^3}]$

5.6 Modelling of Surface Efficiency

The fins in the fin-and-tube configuration in the evaporator are considered in this section in order to model the fin efficiency and overall surface efficiency.

The tubes in the evaporator of the DVI LV9 Combi heat pump are arranged in a staggered grid as stated in Section 3.2. In order to model the fins, these are divided into sections corresponding to one fin per tube. This is done using the so-called Schmidt approximation where hexagonal fins are considered. The staggered tube grid is considered with hexagonal fins symmetrically divided over the total area of a fin. This is shown in Figure 5.7. (Thulukkanam, 2013)

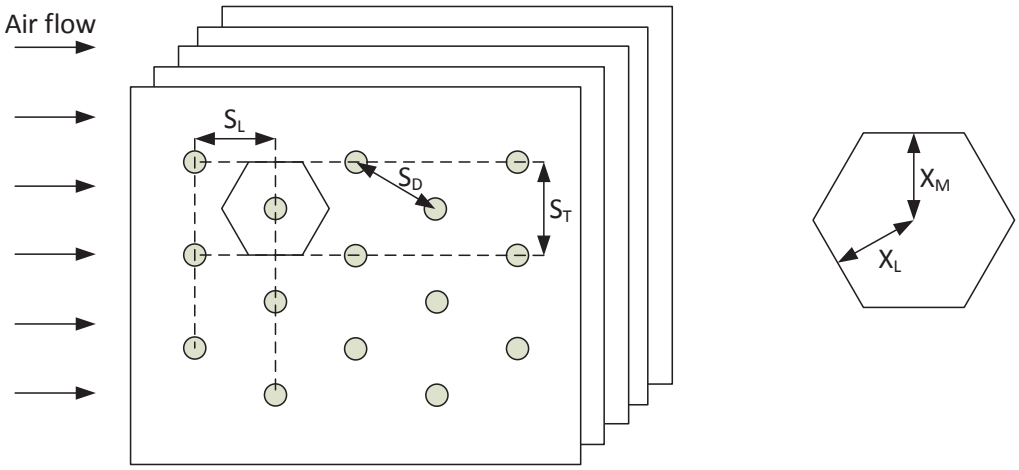

Figure 5.7. The concept of hexagonal fins in the staggered tube grid of the evaporator.

In Figure 5.7, S_L is the longitudinal tube spacing, S_T is the transverse tube spacing and S_D is the diagonal tube spacing.

The geometry of the hexagonal fin implies that a correlation to the circular fin must be considered. In order to approximate the hexagonal fin geometry, the lengths X_M and X_l are used. The definitions of X_M and X_l are given in Equation (5.22) and (5.23) respectively. (Thulukkanam, 2013)

$$X_\mathrm{M} = \frac{S_\mathrm{T}}{2} \quad [\mathrm{m}] \quad (5.22)$$

$$X_\mathrm{L} = \frac{S_\mathrm{D}}{2} \quad [\mathrm{m}] \quad (5.23)$$

The equivalent circular fin radius, r_eq, can be calculated using X_M, X_l and the outer tube radius, $r_\mathrm{tube,o}$, as given in Equation (5.24). (Thulukkanam, 2013)

$$r_\mathrm{eq} = \left(1.27\frac{X_\mathrm{M}}{r_\mathrm{tube,o}}\left(\frac{X_\mathrm{L}}{X_\mathrm{M}} - 0.3\right)^{0.5}\right) r_\mathrm{tube,o} \quad [\mathrm{m}] \quad (5.24)$$

The standard extended surface parameter, m, is calculated using Equation (5.25). (Thulukkanam, 2013)

$$m = \sqrt{\frac{2h_\mathrm{a}}{k_\mathrm{fin} t_\mathrm{fin}}} \quad [\text{-}] \quad (5.25)$$

Where:
h_air is convective heat transfer coefficient of air flow [W/(m^{2}K)]
k_fin is conductivity of the fin material which is aluminium [W/(mK)]
t_fin is fin thickness [m]

The fin efficiency, η_{fin}, can be calculated using modified Bessel functions where m and r_{eq} are used as inputs. The modified Bessel functions are found using MATLAB's *bessel* function.

The fin efficiency, η_{fin}, is given in Equation (5.26). (Theerakulpinut, 1995)

$$\eta_{\text{fin}} = \frac{2r_{\text{t,o}}}{m(r_{\text{eq}}^2 - r_{\text{t,o}}^2)} \frac{I_1(mr_{\text{eq}})K_1(mr_{\text{t,o}}) - K_1(mr_{\text{eq}})I_1(mr_{\text{t,o}})}{I_0(mr_{\text{t,o}})K_1(mr_{\text{eq}}) + I_1(mr_{\text{eq}})K_0(mr_{\text{t,o}})} \quad [\text{-}] \quad (5.26)$$

Where:
I_0 is the modified Bessel function of first kind of order zero [-]
I_1 is the modified Bessel function of first kind of order one [-]
K_0 is the modified Bessel function of second kind of order zero [-]
K_1 is the modified Bessel function of second kind of order one [-]

The calculations performed using Bessel functions are elaborated in Appendix C.

The overall surface efficiency, η_{overall}, is calculated using Equation (5.27). (Thulukkanam, 2013)

$$\eta_{\text{overall}} = 1 - \frac{A_{\text{fin}}}{A_{\text{eva}}}(1 - \eta_{\text{fin}}) \quad [\text{-}] \quad (5.27)$$

Where:
A_{fin} is the fin area [m^2]
η_{overall} is overall surface efficiency [-]

5.7 Modelling of Frost Surface Temperature

The concept of thermal resistance network is used to model the temperature of the frost surface. This is done by calculating a frost surface temperature for both the tubes and the fins in the evaporator. A combined frost surface temperature is calculated based on the frost surface temperatures for the tubes and the fins.

Frost Surface Temperature on Tubes
The thermal resistance network for a frosted tube is configured as the tube wall as the inner cylinder and the frost layer as the outer cylinder as shown in Figure 5.8.

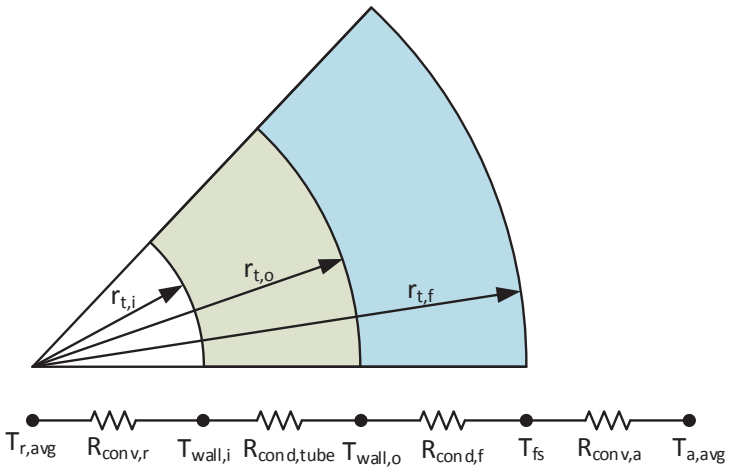

Figure 5.8. Thermal resistance network of a tube with a frost layer around it. The frost layer is illustrated with a blue colour. (Cengel and Ghajar, 2011)

The convective resistance of the refrigerant in the tubes is calculated using Equation (5.28).

$$R_{\text{conv,r}} = \frac{1}{h_{\text{r}} A_{\text{tube,i}}} \quad [\text{K/W}] \quad (5.28)$$

Where:
$R_{\text{conv,r}}$ is convective resistance of refrigerant in the tubes [K/W]
$A_{\text{tube,i}}$ is inner tube area [m^2]

The conductive resistance through the tube wall is given in Equation (5.29).

$$R_{\text{cond,tube}} = \frac{\ln(r_{\text{tube,o}}/r_{\text{tube,i}})}{2\pi L_{\text{tube}} k_{\text{tube}}} \quad [\text{K/W}] \quad (5.29)$$

Where:
$R_{\text{cond,tube}}$ is conductive resistance through the tube wall [K/W]
$r_{\text{tube,o}}$ is outer tube radius [m]
$r_{\text{tube,i}}$ is inner tube radius [m]
L_{tube} is total tube length [m]
k_{tube} is thermal conductivity of the tube copper wall [W/(mK)]

The conductive resistance through the frost layer on the tubes is given in Equation (5.30).

$$R_{\text{cond,tube,f}} = \frac{\ln(r_{\text{tube,f}}/r_{\text{tube,o}})}{2\pi L_{\text{tube}} k_{\text{f}}} \quad [\text{K/W}] \quad (5.30)$$

Where:
$R_{\text{cond,tube,f}}$ is conductive resistance through the frost layer [K/W]
$r_{\text{tube,f}}$ is frost layer radius [m]
k_{f} is thermal conductivity of frost [W/(mK)]

If no frost is present, the conductive resistance for frost is set to zero using an *if/else* statement in the model.

The convective resistance of the air flow over the tubes is calculated using Equation (5.31).

$$R_{\text{conv,tube,a}} = \frac{1}{h_{\text{a}} A_{\text{tube,f}}} \quad [\text{K/W}] \quad (5.31)$$

Where:
$R_{\text{conv,tube,a}}$ is convective resistance of the air flow over the tubes [K/W]
$A_{\text{tube,f}}$ is outer frost layer area on the tubes [m^2]

If no frost is present on the tubes, the area, $A_{\text{tube,f}}$, is equal to the outer tube surface area.

The total thermal resistance through the tubes is given in Equation (5.32).

$$R_{\text{tube,tot}} = R_{\text{conv,r}} + R_{\text{cond,tube}} + R_{\text{cond,tube,f}} + R_{\text{conv,tube,a}} \quad [\text{K/W}] \quad (5.32)$$

Where:
$R_{\text{tube,tot}}$ is total thermal resistance through the tubes [K/W]

The average air and refrigerant temperatures are calculated as logarithmic mean temperature differences as shown in Equation (5.33) and Equation (5.34) respectively.

$$T_{\text{a,avg}} = \frac{T_{\text{a,in}} - T_{\text{a,out}}}{\ln \frac{T_{\text{a,in}}}{T_{\text{a,out}}}} \quad [\text{K}] \quad (5.33)$$

$$T_{\text{r,avg}} = \frac{T_{\text{r,in}} - T_{\text{r,out}}}{\ln \frac{T_{\text{r,in}}}{T_{\text{r,out}}}} \quad [\text{K}] \quad (5.34)$$

The heat transfer rate through the tubes is calculated using Equation (5.35).

$$\dot{Q}_{\text{tube,tot}} = \frac{T_{\text{r,avg}} - T_{\text{a,avg}}}{R_{\text{tube,tot}}} \quad [\text{W}] \quad (5.35)$$

Where:
$\dot{Q}_{\text{tube,tot}}$ is total heat transfer rate through tubes [W]

The outer temperature of the tube wall is found using Equation (5.36).

$$T_{\text{tube,wall,o}} = T_{\text{r,avg}} - (\dot{Q}_{\text{tube,tot}}(R_{\text{conv,r}} + R_{\text{cond,tube}})) \quad [\text{K}] \quad (5.36)$$

Where:
$T_{\text{tube,wall,o}}$ is outer tube wall temperature [K]
$T_{\text{r,avg}}$ is average refrigerant temperature [K]
$T_{\text{a,avg}}$ is average air temperature [K]

The frost surface temperature of the frost layer on the tubes is given in Equation (5.37).

$$T_{\text{tube,fs}} = T_{\text{tube,wall,o}} - (\dot{Q}_{\text{tube,tot}} R_{\text{cond,f}}) \quad [\text{K}] \quad (5.37)$$

Where:
$T_{\text{tube,fs}}$ is frost surface temperature of frost on tubes [K]

Frost Surface Temperature on Fins
The temperature distribution over the fins is calculated in order to model the frost surface temperature on the fins.

The temperature distribution throughout a fin is calculated using Bessel functions. This is done for an equivalent circular fin with an equivalent fin radius, approximated by the hexagonal fin as stated in Section 5.6. The temperature distribution is calculated using Equation (5.38). (Myers, 1998)

$$T_{\text{fin}} = T_{\text{a,avg}} + (T_{\text{tube,wall,o}} - T_{\text{a,avg}}) \frac{K_1(mr_{\text{o}})I_0(mr) + I_1(mr_{\text{o}})K_0(mr)}{I_0(mr_{\text{i}})K_1(mr_{\text{o}}) + I_1(mr_{\text{o}})K_0(mr_{\text{i}})} \quad [\text{K}] \quad (5.38)$$

The temperature distributions is calculated for an inlet air temperature of 0°C and a wall temperature of -7.45°C and shown in Figure 5.9.

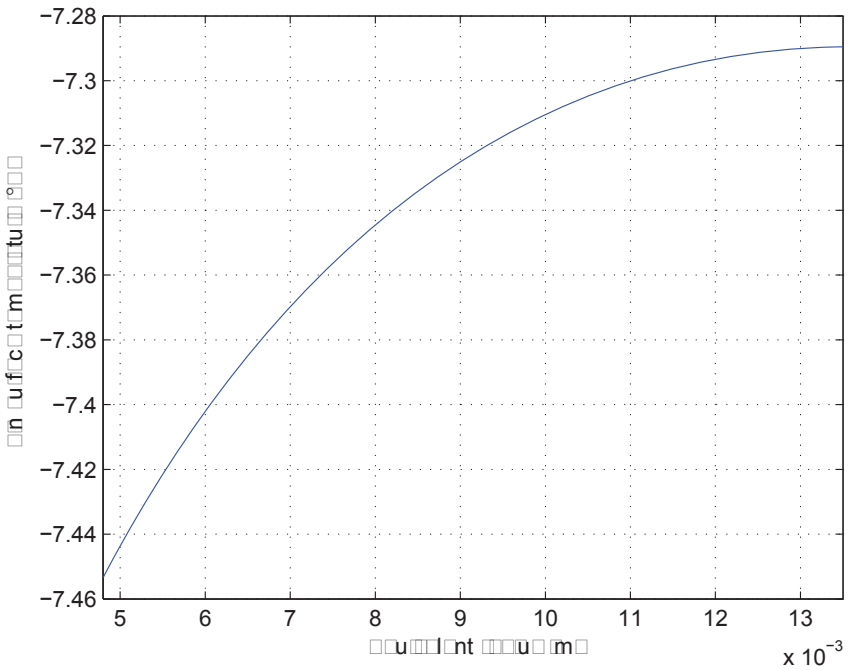

Figure 5.9. Temperature distribution throughout the equivalent circular fin.

As seen in Figure 5.9, the temperature increase throughout the fin is less than 0.16°C. A relative small temperature increase is expected since the distance from the tube wall to the edge of the equivalent circular fin is only 8.8 mm.

The thermal resistances through the fins, the frost layer on the fins, and through the convective air flow over the fins are found in order to determine the frost surface temperature on the fins.

The conductive resistance through the fins is calculated in Equation (5.39).

$$R_{\text{cond,fin}} = \frac{t_{\text{fin}}}{k_{\text{fin}} A_{\text{fin}}} \quad [\text{K/W}] \quad (5.39)$$

Where:
$R_{\text{cond,fin}}$ is conductive resistance through the fins [K/W]
t_{fin} is the thickness of a fin [m]
k_{fin} is the conductivity of the aluminium fin [W/(mK)]
A_{fin} is the fin area [m^2]

The conductive resistance through the frost layer on the fins is calculated in Equation (5.40).

$$R_{\text{cond,fin,f}} = \frac{t_{\text{f}}}{k_{\text{f}} A_{\text{fin,f}}} \quad [\text{K/W}] \quad (5.40)$$

Where:
$R_{\text{cond,fin,f}}$ is conductive resistance through the frost layer on the fins [K/W]
$A_{\text{fin,f}}$ is the area of the frosted fins [m^2]

The convective resistance of the air flow over the fins is calculated using Equation (5.41).

$$R_{\text{conv,fin,a}} = \frac{1}{h_{\text{a}} A_{\text{fin,f}}} \quad [\text{K/W}] \quad (5.41)$$

Where:
$R_{\text{conv,fin,a}}$ is convective resistance of the air flow over the fins [K/W]

The total thermal resistance through the frost and air flow on the fins is calculated using Equation (5.42).

$$R_{\text{fin,tot}} = R_{\text{cond,fin}} + R_{\text{cond,fin,f}} + R_{\text{conv,fin,a}} \quad [\text{K/W}] \quad (5.42)$$

Where:
$R_{\text{fin,tot}}$ is total thermal resistance through the frost and air flow on the fins [K/W]

The heat transfer rate through the fins is calculated in Equation (5.43).

$$\dot{Q}_{\text{fin,tot}} = \frac{T_{\text{a,avg}} - T_{\text{fin,avg}}}{R_{\text{fin,tot}}} \quad [\text{W}] \quad (5.43)$$

Where:
$\dot{Q}_{\text{fin,tot}}$ is heat transfer rate through the fins [W]
$T_{\text{fin,avg}}$ is average fin surface temperature [K]

The fin surface temperature, $T_{\text{fin,avg}}$, is averaged over the fin temperature increase shown in Figure 5.9. This is regarded to be a valid assumption since the temperature drop throughout the fin is only approximately 0.16°C.

The frost surface temperature on the fins is calculated in Equation (5.44).

$$T_{\text{fin,fs}} = T_{\text{a,avg}} - (\dot{Q}_{\text{fin,tot}} R_{\text{conv,fin,a}}) \quad [\text{K}] \quad (5.44)$$

Where:
$T_{\text{fin,fs}}$ is frost surface temperature of frost on fins [K]

Combined Frost Surface Temperature
The frost surface temperatures for frost on the tubes and on the fins are combined to a weighed frost surface temperature. The frost surface temperatures are weighed using the fraction of the total frosted area that frosted tubes and frosted fins constitute. This is given in Equation (5.45).

$$T_{\text{fs}} = T_{\text{tube,fs}} \frac{A_{\text{tube,f}}}{A_{\text{eva,f}}} + T_{\text{fin,fs}} \frac{A_{\text{fin,f}}}{A_{\text{eva,f}}} \quad [\text{K}] \quad (5.45)$$

Where:
T_{fs} is combined frost surface temperature of frost on both tubes and fins [K]

With the frost surface temperature known it is possible to calculate the frost surface density.

5.8 Modelling of Overall Heat transfer Coefficient and Heat Transfer Rate

The overall heat transfer coefficient for the evaporator, U_{eva}, is calculated based on the convective heat transfer coefficients, the thermal resistances and the overall surface efficiency.

The convective heat transfer coefficients were presented in Section 5.4 and the overall surface efficiency was calculated in Section 5.6. The thermal resistances for the total frost layer and the thermal resistance for the tube walls and the fins are calculated in the following.

The thermal resistance through the total frost layer is found using the frost conductivity and the surface area of the evaporator where frost is deposited. This is calculated using Equation (5.46).

$$R_{\text{f}} = \frac{t_{\text{f}}}{k_{\text{f}} A_{\text{eva,f}}} \quad [\text{K/W}] \quad (5.46)$$

The thermal resistance through the tube walls and the fins is found using the conductive wall resistance from the tubes and the conductive resistance through the fins. The two resistances are used to find a weighted average using the areas of the tubes and the fins. This is given in Equation (5.47).

$$R_{\text{w}} = R_{\text{cond,tube,w}} \frac{A_{\text{tube,o}}}{A_{\text{eva}}} + R_{\text{cond,fin}} \frac{A_{\text{fin}}}{A_{\text{eva}}} \quad [\text{K/W}] \quad (5.47)$$

The overall heat transfer coefficient is calculated using Equation (5.48).

$$\frac{1}{U_{\text{eva}} A_{\text{eva}}} = \frac{1}{h_{\text{a}} A_{\text{eva}} \eta_{\text{overall}}} + R_{\text{w}} + R_{\text{f}} + \frac{1}{h_{\text{r}} A_{\text{tube,i}}} \quad [\text{K/W}] \quad (5.48)$$

Where:
U_{eva} is overall heat transfer coefficient for the evaporator [W/(m^{2}K)]
A_{eva} is heat transfer surface area of evaporator [m^2]
R_{w} is weighted average thermal resistance through the tube walls and the fins [K/W]
R_{f} is thermal resistance through frost layer on the frosted area of the evaporator [K/W]
$A_{\text{tube,i}}$ is inner surface area of the tubes in the evaporator [m^2]
η_{overall} is overall surface efficiency [-]

The overall heat transfer coefficient, U_{eva}, is solved in Equation (5.48) and used to model the heat transfer rate using the Log Mean Temperature Difference method.

LMTD Method
In heat exchangers, the temperature of the hot and cold fluids varies throughout the exchanger, and it is therefore useful to have an expression for the mean temperature difference. In parallel-flow and counter-flow heat exchangers, the LMTD method is a common way to achieve this mean temperature difference. Such an expression can be derived from relatively simple energy balances to yield the heat transfer rate in Equation (5.49) where LMTD is expressed in Equation (5.50). (Cengel et al., 2008)

$$\dot{Q} = UA_{\text{s}}\Delta T_{\text{LMTD}} \quad [\text{W}] \quad (5.49)$$

$$\Delta T_{\text{LMTD}} = \frac{\Delta T_a - \Delta T_b}{\ln(\frac{\Delta T_a}{\Delta T_b})} \quad [\text{K}] \quad (5.50)$$

Where:
$\dot{Q}$ is heat transfer rate [W]
U is overall heat transfer coefficient [W/m^2]
A_{s} is surface area [m^2]
ΔT_{LMTD} is the Logarithmic Mean Temperature Difference [K]
ΔT_a is temperature difference [K]
ΔT_b is temperature difference [K]

In these equations, ΔT_a and ΔT_b, represents the temperature difference at the two ends of the heat exchanger. For the evaporator, this will be the inlet and outlet temperatures of refrigerant and air. Note that Equation (5.51) and Equation (5.52) are only valid for counter-flow heat exchangers.

$$\Delta T_a = T_{\text{a,in}} - T_{\text{r,out}} \quad [\text{K}] \quad (5.51)$$
$$\Delta T_b = T_{\text{a,out}} - T_{\text{r,in}} \quad [\text{K}] \quad (5.52)$$

Where:
$T_{\text{a,in}}$ is air temperature at inlet [K]
$T_{\text{a,out}}$ is air temperature at outlet [K]
$T_{\text{r,in}}$ is refrigerant temperature at inlet [K]
$T_{\text{r,out}}$ is refrigerant temperature at outlet [K]

The evaporator is a cross-flow fin-and-tube heat exchanger where the refrigerant exchanges heat with the ambient air. As mentioned, the LMTD method can only be used for parallel

and counter-flow heat exchangers. This means that another approach is required for the evaporator. Using a similar approach to derive expressions for a cross-flow heat exchanger, as for a counter-flow heat exchanger, leads to very complicated expressions due to the complex flow conditions. In cross-flow applications it is therefore practical to relate a correction factor to the LMTD approach, as shown in Equation (5.53). (Cengel et al., 2008)

$$\Delta T_{\text{LMTD,CF}} = F \Delta T_{\text{LMTD}} \quad [\text{K}] \quad (5.53)$$

Where:
$\Delta T_{\text{LMTD,CF}}$ is log mean temperature difference for a cross-flow heat exchanger [K]
F is Cross-flow correction factor [-]

The correction factor is always less than one and depends on the geometry of the heat exchanger and the inlet and outlet temperatures of both streams. The correction factor is a measure of deviation from a corresponding case of a counter-flow heat exchanger.

To determine the F-value, the P and R temperature ratios from the inlet and outlet temperatures must be calculated. These are given in Equation (5.54) and Equation (5.55) respectively. (Cengel et al., 2008)

$$P = \frac{T_{\text{r,out}} - T_{\text{r,in}}}{T_{\text{a,in}} - T_{\text{r,in}}} \quad [-] \quad (5.54)$$

$$R = \frac{T_{\text{a,in}} - T_{\text{a,out}}}{T_{\text{r,out}} - T_{\text{r,in}}} \quad [-] \quad (5.55)$$

Once the P and R ratios are found, the correction factor can be determined using the diagram in Figure 5.10.

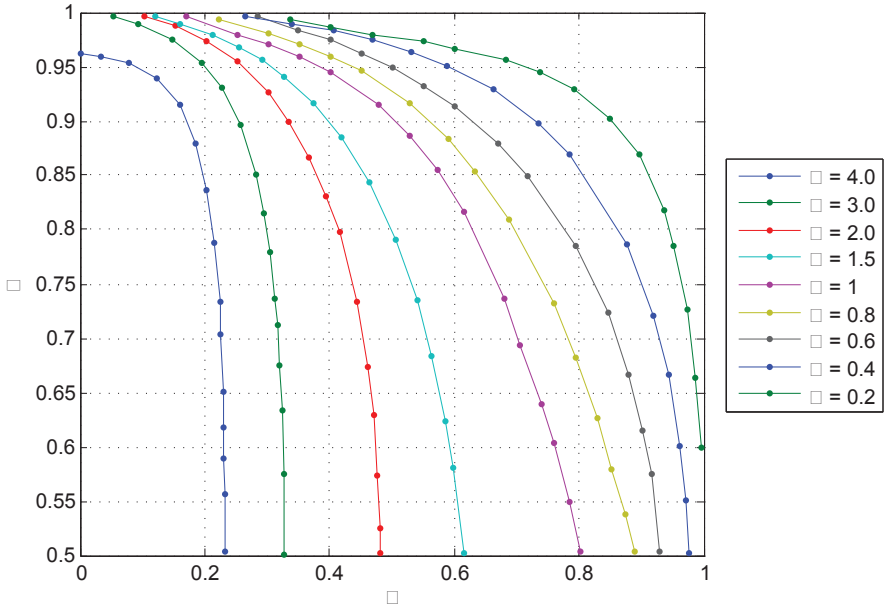

Figure 5.10. Correction factor as function of P and R values. Data is scanned from Cengel et al. (2008).

To enable the model to determine the correction factor it is necessary to use interpolation. This will allow the model to calculate the correction factor at any P and R values within the range, and not just for the nine R-curves shown in Figure 5.10. The interpolation is done by reading 15 data points for each R-curve and afterwards use MATLAB's *meshgrid* function to create a mesh from the data points. This is shown in Figure 5.11.

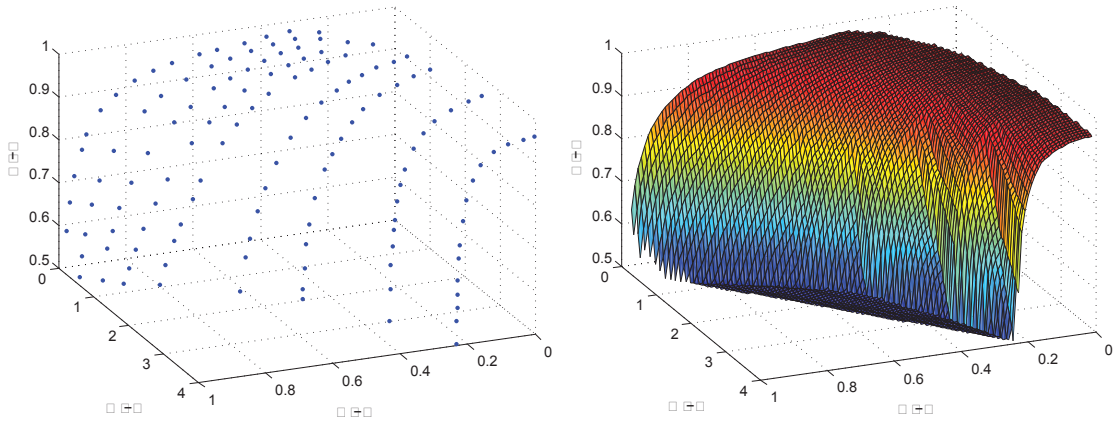

Figure 5.11. Left: The correction factor data points. Right: The created mesh using MATLAB's *meshgrid* function.

Once the mesh is created, MATLAB's *griddata* function can determine the F-value from the P and R input values.

5.9 Properties for Frost

The frost layer that formates on the evaporator surface is described through thermal properties of frost. These properties include frost surface temperature, frost density, frost conductivity, thickness of frost layer and mass of frost.

Frost Density
The frost density and frost conductivity are used to calculate the frost thickness and to update the frost properties with the time step τ.

The correlation used to model the frost density is suggested by Hayashi et al. (1977) and is given in Equation (5.56).

$$\rho_f = 650\exp(0.227(T_{fs} - 273.15)) \qquad \left[\mathrm{kg/m^3}\right] \quad (5.56)$$

Where:
ρ_f is frost density $[\mathrm{kg/m^3}]$
T_{fs} is frost surface temperature [K]

The frost density correlation is a function of the frost surface temperature, T_{fs}, and it is valid for -25°C $< T_{fs} <$ 0°C. The correlation is plotted in this range in Figure 5.12. (Hayashi et al., 1977)

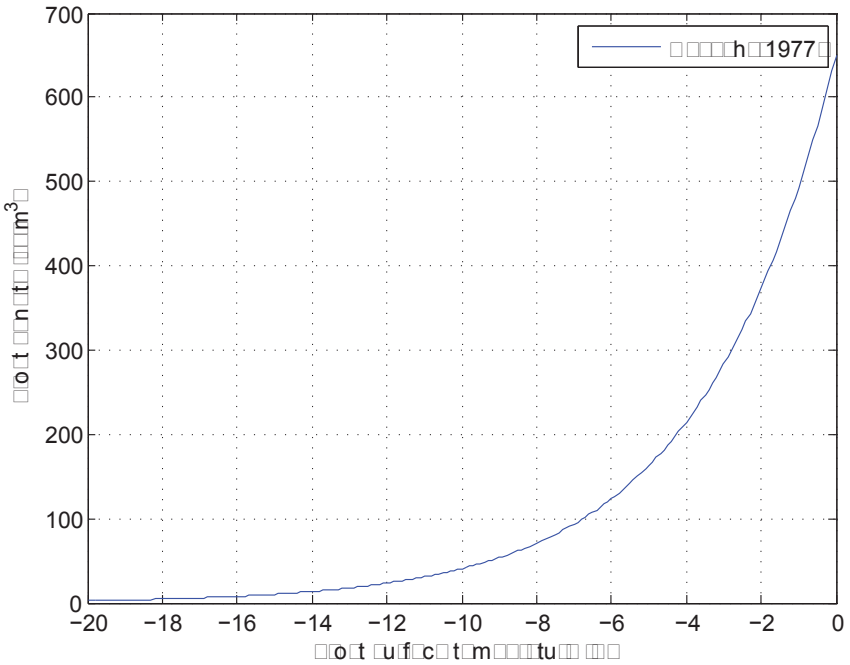

Figure 5.12. Frost density as function of frost surface temperature. (Hayashi et al., 1977)

The frost density increases exponentially with increased frost surface temperature. The frost density is therefore expected to vary significantly with ambient conditions. This will be investigated and elaborated further in the sensitivity analysis in Section 5.10.

Frost Thermal Conductivity

The frost thermal conductivity, k_f, can be calculated through several empirical correlations which has been proposed in previous research within the field. Some of the most documented correlations are considered and compared by Kandula (2010) for NASA. These are discussed in the following.

The correlation from Van Dusen (1929) is based on data from six other investigators and it has no restriction on the range of frost density. It is given in Equation (5.57). Kandula (2010)

$$k_f = 0.029 + 0.403 \cdot 10^{-3} \rho_f + 0.2367 \cdot 10^{-8} \rho_f^3 \qquad [\mathrm{W/(mK)}] \quad (5.57)$$

The correlation from Yonko & Sepsy (1967) is valid for frost densities lower than 573 kg/m^3 with no lower limit and is given in Equation (5.58). Kandula (2010)

$$k_f = 0.024248 + 0.731 \cdot 10^{-3} \rho_f + 0.1183 \cdot 10^{-5} \rho_f^2 \qquad [\mathrm{W/(mK)}] \quad (5.58)$$

The correlation from Östin & Anderson (1991) is valid for frost densities in the range of 50 to 680 kg/m^3 and is given in Equation (5.59). Kandula (2010)

$$k_f = -8.71 \cdot 10^{-3} + 4.39 \cdot 10^{-4} \rho_f + 1.05 \cdot 10^{-6} \rho_f^2 \qquad [\mathrm{W/(mK)}] \quad (5.59)$$

The correlation from Sturm (1997) is considered the standard reference for snow thermal conductivities.

The correlation is combined from two functions which are given in Equation (5.60) and Equation (5.61) respectively. (Kandula, 2010)

$$k_f = 0.138 - 1.01 \cdot 10^{-3}\rho_f + 3.233 \cdot 10^{-6}\rho_f^2 \qquad 156 \leq \rho_f \leq 600 \qquad [\mathrm{W/(mK)}] \quad (5.60)$$

$$k_f = 0.023 + 0.234 \cdot 10^{-3}\rho_f \qquad \rho_f < 156 \qquad [\mathrm{W/(mK)}] \quad (5.61)$$

The correlations are plotted as function of the frost density correlation in Equation (5.56) and shown in Figure 5.13. Notice that the Sturm correlation is plotted for both functions with a change at the frost density of 156 kg/m^3. (Kandula, 2010)

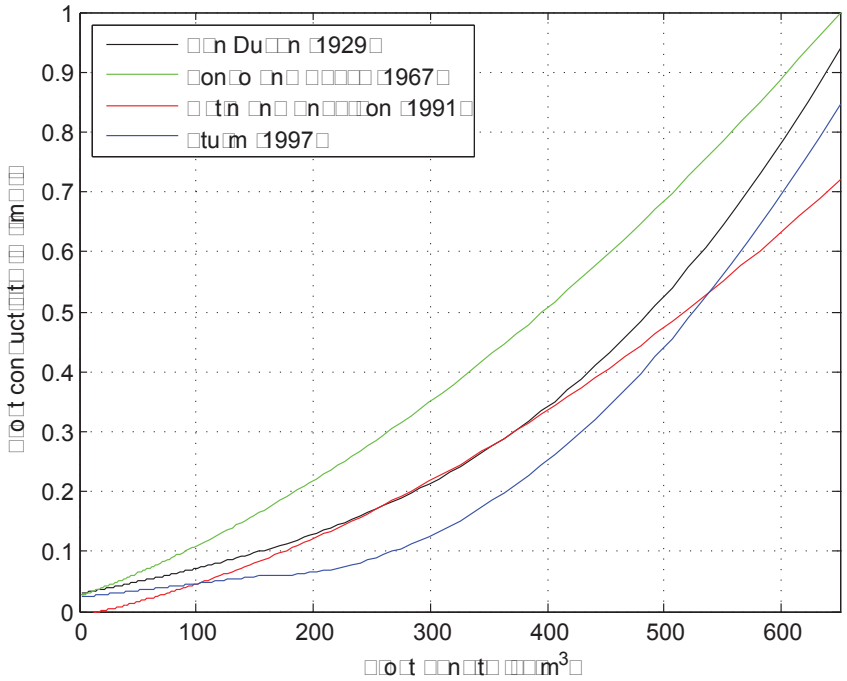

Figure 5.13. Frost conductivity correlations as function of frost density. (Kandula, 2010)

As seen in Figure 5.13, there are relative large deviations between the correlations at some densities. In the frost density range from approximately 100 kg/m^3 to 550 kg/m^3, the correlation from Sturm (1997) gives the lowest frost conductivity. The correlation from Yonko & Sepsy (1967) gives the highest frost conductivity in the full frost density range. The correlations from Van Dusen (1929) and Östin & Anderson (1991) has almost the same frost conductivity in the frost density range from approximately 225 kg/m^3 to 375 kg/m^3. The choice of frost conductivity correlation will have a great impact on the thermal resistance trough the frost layer which again will affect the overall heat transfer coefficient. This will be investigated and elaborated further in the sensitivity analysis in Section 5.10.

Mass of Frost

The mass of frost is modelled using the absolute humidity content and mass flow rate of atmospheric air at inlet and outlet of the evaporator. The theoretical maximum mass of frost is calculated using Equation (5.62). (Qu et al., 2011)

$$m_{f,max} = \frac{\dot{m}_a \tau}{1 + \omega_{in}} \cdot (\omega_{in} - \omega_{out}) \qquad [\mathrm{kg}] \quad (5.62)$$

Where:
$m_{f,max}$ is the theoretical maximum mass of frost increment in time τ [kg]
$\dot{m}_a$ is mass flow rate of atmospheric air [kg/s]
τ is the time step size [s]
ω_{in} is absolute humidity content in atmospheric air at inlet [kg/kg]
ω_{out} is absolute humidity content in atmospheric air at outlet [kg/kg]

The absolute humidities are calculated based on the saturation pressure at the inlet and outlet of the evaporator. The way these are calculated is elaborated in Appendix A.

Since the mass of frost calculated in Equation (5.62) is the theoretical maximum amount of frost that can formate on the surface of the evaporator, a fraction is introduced that describes the percentage of the evaporator area where frost is deposited. This is done using x_f and is given in Equation (5.63).

$$m_f = m_{f,max} \frac{x_f - 1}{D_{fin}} \quad [kg] \quad (5.63)$$

Where:
m_f is the mass of frost increment in time τ [kg]
D_{fin} is the depth of a fin [m]
x_f is the distance from the point where frost starts to deposit to the evaporator outlet [m]

In this way it is possible to adjust the mass of frost using x_f.

Frost Layer Thickness
With the mass of frost known it is possible to calculate the thickness of the frost layer using Equation (5.64). (Yang and Lee, 2004)

$$t_f = \frac{m_f}{A_{eva,f}\rho_f} \quad [m] \quad (5.64)$$

With the frost thickness calculated, all relevant frost properties has been determined. The values for frost conductivity, k_f, mass of frost, m_f, and frost thickness, t_f, are used to update the iteration procedure in each time step.

5.10 Sensitivity Analysis of Properties of Frost

A sensitivity analysis is performed for some of the properties of frost in order to identify and discuss the influence and variation of these parameters.

Frost Surface Temperature and Frost Density
The frost surface temperature is very dependent on the evaporation temperature and will therefore vary accordingly. As the air temperature varies, this affects the evaporation temperature directly and therefore also the frost surface temperature and density. In order to investigate these variations, three scenarios with air temperatures of -4°C, 0°C, and 4°C are simulated at a constant relative humidity of 75%. The tendencies are shown in Figure 5.14.

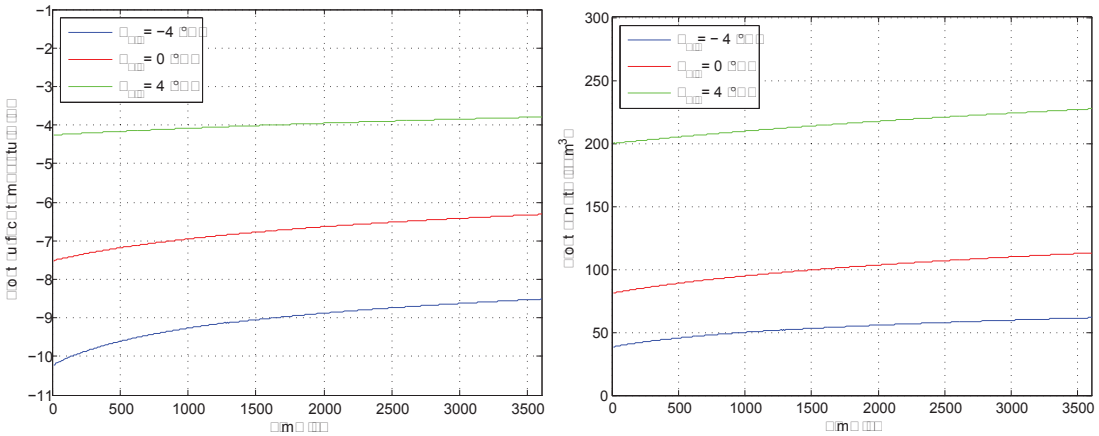

Figure 5.14. Left: Variation of frost surface temperature. Right: Frost density at different air temperatures.

As seen in the left part of Figure 5.14, an increased air temperature results in a higher frost surface temperature. Over time, the frost surface temperature increases slightly due to the frost layer thickness increase and change of thermal resistance for the frost layer. An increased frost surface temperature yields an increased frost density. Hence, the temperature that the frost development occurs at determines the density of the frost layer and therefore also the frost layer thickness. A frost layer of a specific mass developed at a high frost density will have a thinner frost layer thickness than a frost layer developed at a low frost density. This means that an increased mass of frost not necessarily yields a higher pressure drop over the evaporator, if the frost thickness does not increase due to a more dense frost layer. The frost density will have a great influence on the frost conductivity where a high frost density will result in a high frost conductivity, dependent on which correlation that is considered for frost conductivity.

Frost Thermal Conductivity

A sensitivity analysis is performed for the frost thermal conductivity and the influence it has on the reduction of the heat transfer rate in the evaporator.

The correlations for frost conductivity, and the deviation between them, implies that the thermal resistance in the frost layer will vary depending on which correlation that is used. This will directly affect the overall heat transfer coefficient. In order to quantify the deviation of the different frost conductivities, the overall heat transfer coefficients are simulated for one hour with the different frost conductivity correlations. This is done for a relative humidity of 80% and an ambient temperature of 3°C. The deviation for the overall heat transfer coefficients are shown in Figure 5.15. Notice that the y-axis starts at 18 W/(m^{2}K).

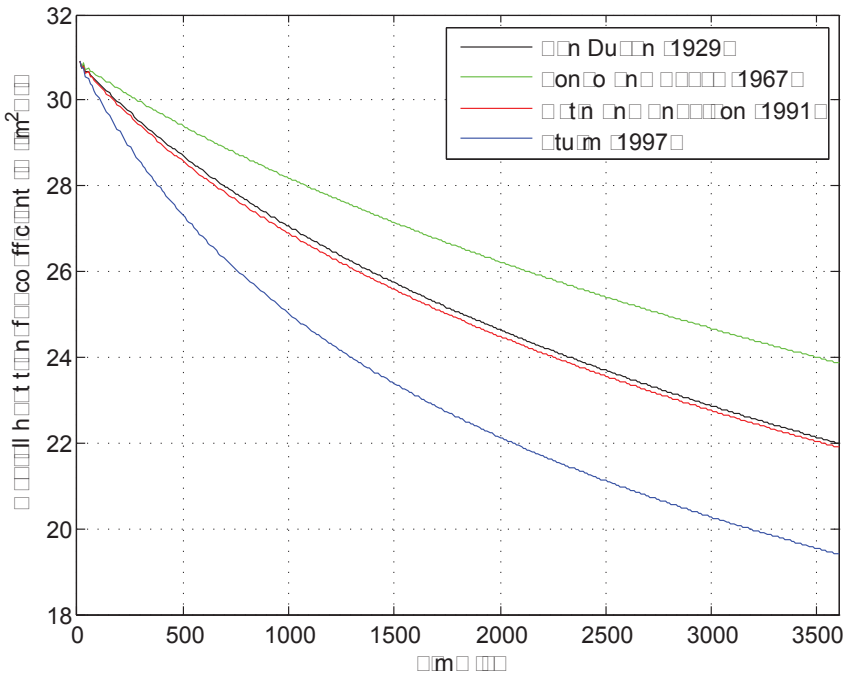

Figure 5.15. Deviation of overall heat transfer coefficient at different frost conductivity correlations. The simulation is done at $\phi = 80\%$ and T = 3°C. Notice that the y-axis starts at 18 W/(m^{2}K).

The overall heat transfer coefficients, shown in Figure 5.15, yields different drops according to the frost conductivity correlation used. The correlation from Sturm (1997) yields the greatest drop in overall heat transfer coefficient and has a value of approximately 19.5 W/(m^{2}K) after one hour which corresponds to a drop of approximately 33%. The lowest drop in overall heat transfer coefficient is found for the correlation from Yonko & Sepsy (1967) which yields a drop to approximately 24 W/(m^{2}K). This corresponds to a drop of approximately 20%. The correlations from Van Dusen (1929) and Östin & Anderson (1991) yields a drop in overall heat transfer coefficient to approximately 22 W/(m^{2}K) which corresponds to drops of 26%.

It is necessary to determine which correlation that is most suitable for the frost conditions that the experiments with the DVI LV9 Combi heat pump are performed at. This is done by comparing the performance patterns that the different correlations gives with the measured performance of the DVI LV9 Combi heat pump at similar operation conditions.

5.11 Determination of Defrost Initiation Point

The point of defrost cycle initiation is considered in this section and the objective is to determine the point of initiation of the defrost cycle based on an energy comparison. The heat energy exchanged in the evaporator will be compared to the energy that is required to perform a defrost cycle in order to determine when it is beneficial to perform a defrost cycle. The heat energy exchanged in the evaporator is considered in the following.

Heat Energy Exchanged in Evaporator

The heat energy exchanged in the evaporator is considered. With frost deposition on the evaporator surface, the performance of the evaporator will drop over time and the energy exchanged in it will therefore decrease with time as well. This scenario is simulated for one hour with a relative humidity of 80% and an ambient temperature of 3°C. The performance for the evaporator with and without frost for this scenario is plotted in Figure 5.16. $\dot{Q}_{\text{rated}}$ corresponds to the performance of the evaporator without frost on it and $\dot{Q}_{\text{eva}}$ corresponds to the evaporator performance which is gradually decreased due to frost formation.

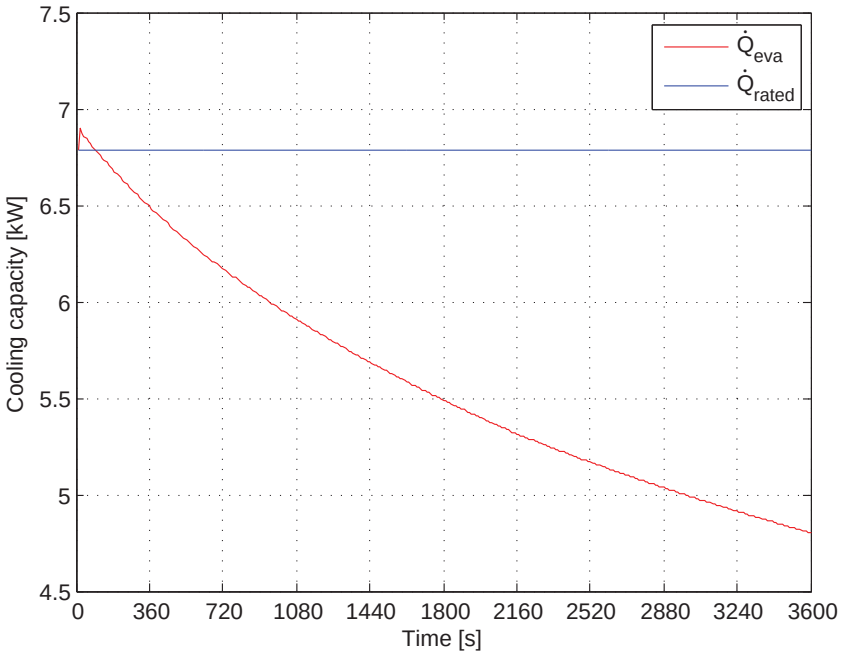

Figure 5.16. Performance for the evaporator with and without frost for a one hour simulation at $\phi = 80\%$ and T = 3°C. The simulation is done with the frost conductivity correlation suggested by Östin and Anderson.

The performance clearly drops as the frost layer increases with time. After one hour, the performance is approximately 29% lower than the maximum performance.

The corresponding amount of heat energy that is exchanged in the evaporator is plotted in Figure 5.17. Q_{rated} corresponds to the energy exchange in the evaporator without frost on it and Q_{eva} corresponds to the evaporator energy exchange at frosted conditions.

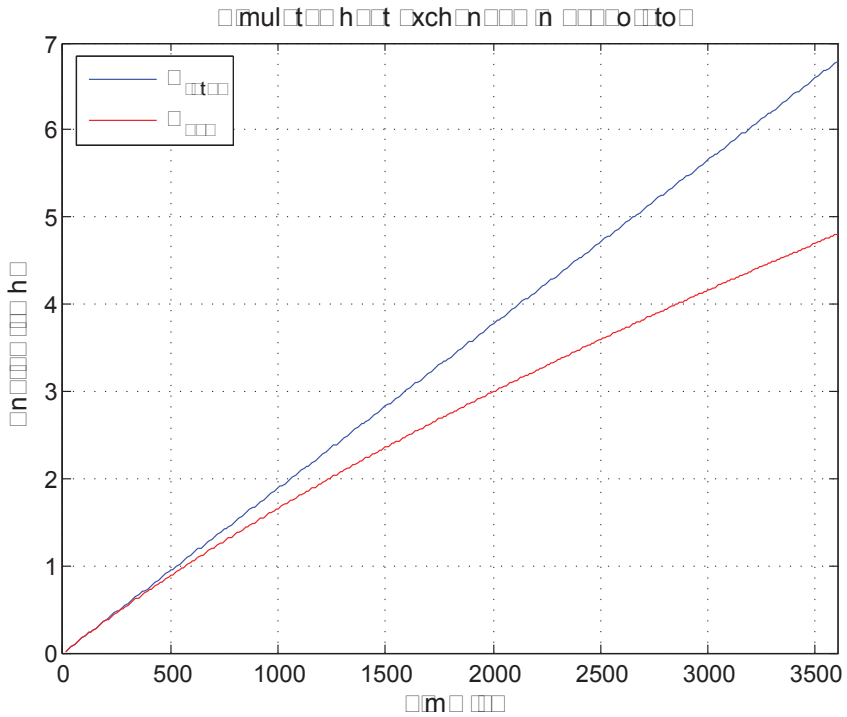

Figure 5.17. Heat energy exchanged in the evaporator with and without frost for a one hour simulation at $\phi = 80\%$ and T = 3°C. The simulation is done with the frost conductivity correlation suggested by Östin and Anderson.

The energy exchanged in the evaporator drops when the frost layer increases with time. The energy that could have been produced on the heat pump, but is not produced because the performance is reduced due to frost, is calculated in Equation (5.65).

$$Q_{\text{difference}} = Q_{\text{rated}} - Q_{\text{eva}} \quad [\text{J}] \quad (5.65)$$

Where:
$Q_{\text{difference}}$ is the amount of energy that the heat pump is reduced with due to frost [kWh]
Q_{rated} is the energy exchange in the evaporator without frost [kWh]
Q_{eva} is the energy exchange in the evaporator at frosted conditions [kWh]

The heat energy that the heat pump is reduced with due to frost, $Q_{\text{difference}}$, is compared to the energy that is required in order to perform a defrost cycle. The defrost cycle is considered in the following.

Energy Required to Perform Defrost Cycle
When a defrost cycle is performed, the energy production on the heat pump unit is stopped for the time it takes to perform the defrost cycle. During the defrost cycle, energy is required to melt the frost that has deposited on the evaporator surface during normal operation. This energy is taken from the storage tank in the heating system and energy is consumed in the compressor as well. The energy that is taken from the storage tank must be reproduced after the defrost cycle in order to restore the energy that is available for the consumer.

The energy needed to melt the frost on the evaporator surface is calculated by considering the mass of frost on the frosted evaporator surface and an enthalpy balance for the frost. The temperature of the melting water that drains of the evaporator during defrost is measured during the experiments and the temperature of it increases during the defrost from approximately 0°C to 8°C. It is therefore assumed that the frost melted to water is heated to 4°C in average. It is also assumed that the temperature of the frost is equal to the average temperature between the evaporator surface temperature and the frost surface temperature.

The energy required to melt the frost on the evaporator is calculated as the mass of frost multiplied with the enthalpy difference between melted water at 4°C and frost, plus the latent heat of melting. The latent heat of melting is equal to 334 kJ/kg for water which is absorbed in the endothermic melting process. This is calculated using Equation (5.66).

$$Q_{\text{defrost}} = m_{\text{f}}((h_{\text{water}} - h_{\text{f}}) + h_{\text{melting}}) \quad [\text{J}] \quad (5.66)$$

Where:
Q_{defrost} is the energy required to melt frost [J]
h_{water} is the enthalpy of the melted frost at 4°C [kJ/kg]
h_{f} is the enthalpy of the frost at the average frost temperature [kJ/kg]
h_{melting} is the latent heat of melting for water [kJ/kg]

The heat supplied from the storage tank during the defrost cycle is calculated by considering the heat transfer rate from the storage tank to the condenser. These properties are measured during the experiments and used as inputs in the model. The heat supplied from the storage tank during defrost is calculated using Equation (5.67).

$$\dot{Q}_{\text{tank}} = \dot{m}_{\text{tank}} c_{\text{p,tank}} \Delta T_{\text{tank}} \quad [\text{W}] \quad (5.67)$$

Where:
$\dot{Q}_{\text{tank}}$ is the heat transfer rate from the storage tank during defrost [W]
$\dot{m}_{\text{tank}}$ is the mass flow rate of the heat flow from the storage tank [kg/s]
$c_{\text{p,tank}}$ is average specific heat capacity of in- and outflow from the storage tank [J/(kgK)]
ΔT_{tank} is the temperature difference between the in- and outflow from the storage tank [K]

Besides the heat taken from the storage tank, the compressor utilises electricity during the defrost. The input power to the compressor during defrost operation is assumed to be equal to the compressor power at normal operation. The total heating capacity supplied to the system during a defrost cycle is given in Equation (5.68).

$$\dot{Q}_{\text{supply}} = \dot{Q}_{\text{tank}} + P_{\text{comp}} \quad [\text{W}] \quad (5.68)$$

Where:
$\dot{Q}_{\text{supply}}$ is the total heating capacity supply to the system during defrost [W]
P_{comp} is the compressor power [W]

Using the energy required to melt the frost on the evaporator surface and the power supplied to the system during a defrost cycle yields the defrost time τ_{defrost} which is given in Equation (5.69).

$$\tau_{\text{defrost}} = \frac{Q_{\text{defrost}}}{\dot{Q}_{\text{supply}}} \quad [\text{s}] \quad (5.69)$$

Where:
τ_{defrost} is defrost time [s]

The energy that is taken from the storage tank must be reproduced after the defrost cycle has been performed. The amount of energy that must be reproduced is found using Equation 5.70.

$$Q_{\text{reproduced}} = \dot{Q}_{\text{tank}} \tau_{\text{defrost}} \quad [\text{J}] \quad (5.70)$$

Where:
$Q_{\text{reproduced}}$ is the amount of energy that must be reproduced [J]

The energy that is lost due to production stop while the defrost cycle is performed is calculated based on the defrost time, τ_{defrost}, and an additional time, τ_{reverse}, in which the 4-way valve is reversed and the evaporator is allowed to drain off. These times are used to perform the defrost process which is described step by step in Section 3.3. The energy lost due to production stop is found using the performance curve for the frosted evaporator shown in Figure 5.16. The energy lost due to production stop is calculated in Equation (5.71).

$$Q_{\text{stop}} = \dot{Q}_{\text{eva}}(\tau_{\text{defrost}} + \tau_{\text{reverse}}) \quad [\text{J}] \quad (5.71)$$

Where:
Q_{stop} is the amount of energy that could have been produced on the heat pump [J]
τ_{reverse} is the time in which the production is stopped to perform the defrost cycle [s]

The total energy required in a defrost cycle is calculated in Equation 5.72.

$$Q_{\text{total,defrost}} = Q_{\text{defrost}} + Q_{\text{reproduced}} + Q_{\text{stop}} \quad [\text{J}] \quad (5.72)$$

Where:
$Q_{\text{total,defrost}}$ is the total amount of energy that is required in a defrost cycle [J]

Determination of Defrost Initiation Point

The point where it is no longer beneficial to run the heat pump with the decreasing performance due to frosting, but instead perform a defrost cycle is the point where the defrost cycle should be initiated. This point is found by comparing the energy required for defrost with the amount of energy that the heat pump is reduced with due to frost.

The total energy required for a defrost cycle is calculated for a simulation with the same conditions as for the heat energy exchange in the evaporator. This is plotted in Figure 5.18 together with the amount of energy that the heat pump is reduced with due to frost, $Q_{\text{difference}}$.

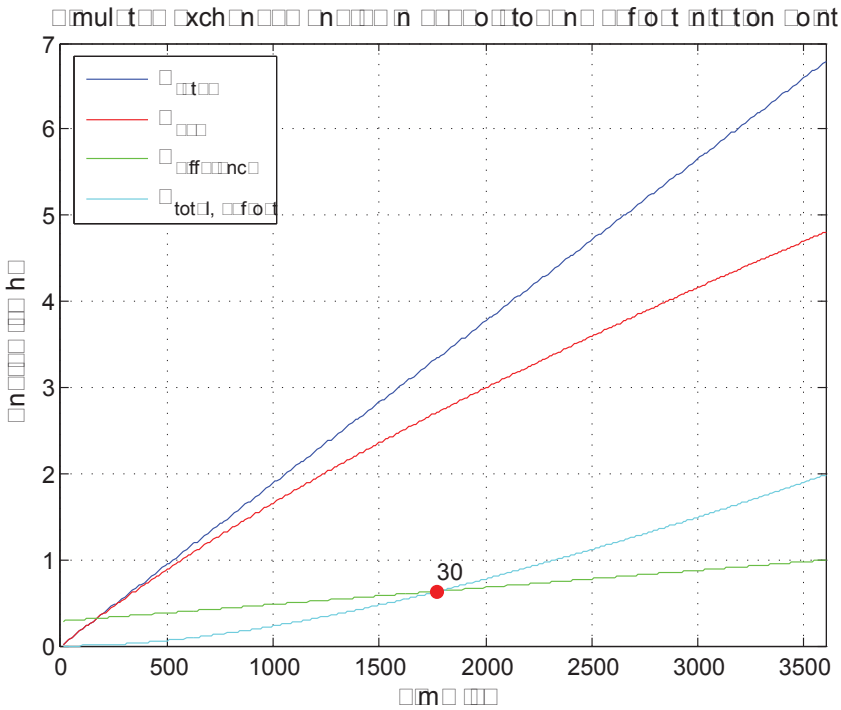

Figure 5.18. Total amount of energy required for a defrost cycle and amount of energy the heat pump is reduced with due to frost. The red dot indicate the defrost initiation point and the corresponding time in minutes.

As expected, the amount of energy required for a defrost process increases with time due to an increasing amount of frost. A larger mass of frost requires more energy to melt it, hence more energy must be added to the system during the defrost cycle. Adding more energy to the system during defrost yields taking more energy out of the storage tank which has to be reproduced. The point where $Q_{\text{difference}}$ exceeds the defrost energy, $Q_{\text{total,defrost}}$, is the point where it is more beneficial to perform a defrost cycle than continue operating the heat pump with a reduced performance. In this simulation it occurs after approximately 30 minutes.

Chapter 6

Test of the DVI LV9 Combi Heat Pump

The tests and experiments performed on the DVI LV9 Combi heat pump are described in this chapter. The purpose of the experiments, the experimental set-up, and a description of the approach are given. Additionally, the data acquisition using LabVIEW is explained and an uncertainty analysis is performed.

6.1 Purpose of Experiments

Performing experiments in this project has several purposes. First of all it is intended to validate the results of the model by comparing measurable parameters. These are the cooling capacity for the evaporator and the pressure difference across the evaporator air side. The cooling capacity of the evaporator is a major point of interest because this value is used to determine the point of defrost initiation in the model. Since it is not possible to measure the cooling capacity directly, it will be verified through measurements on the heating capacity for the condenser and the electrical power input to the compressor. Once the model is verified, the objective is to compare the defrost strategy of the model to the current defrost strategy of the DVI LV9 Combi heat pump. This will be done by comparing the total amount of energy delivered by the heat pump with the two strategies. Additionally, it is of interest to determine how the relative humidity and air temperature are affecting the frost formation and where on the evaporator the frost is deposited. The frosting and defrosting processes are expected to have a repeating pattern which is also investigated. The main goals for the experiments are given below:

- Investigation of repetitive pattern of multiple subsequent defrost cycles.
- Investigation of cooling capacity reduction as function of time without performing defrost.
- Investigate the frost formation process and distribution of frost on the evaporator surface using images.
- Determining the influence of relative humidity and air temperature on the frost formation process and on the performance reduction of the heat pump.
- Validation of the frost formation model using experimental results.
- Comparison of DVI Energi's current defrost strategy and the defrost strategy determined by the frost formation model.

A list of the experiments and their settings is set up to provide an overview. In order to investigate if there is a repeating pattern of the operation cycles, one experiment with four subsequent operation and defrost cycles will be conducted. To investigate the cooling capacity reduction as function of time without performing defrosting, a two hour experiment with

no defrost process is conducted. To investigate the influence of the air temperature, three experiments will be conducted where the relative humidity is kept constant and the air temperature is varied. Similarly, the influence of the relative humidity will be investigated through three experiments with constant air temperature and varied relative humidity. The six experiments with varied air temperature and relative humidity will be used to validate the frost formation model. During these six experiments, a USB camera will take an image of the evaporator surface in the bottom of the evaporator with an interval of 5 minutes. This is done in order to investigate and illustrate the rate of frost formation and the thickness and variation of the frost layer. Finally, two experiments of 5 hours duration will be conducted to compare the defrost strategies. Table 6.1 contains a list of the experiments and their settings.

Table 6.1. The experiments performed on the DVI LV9 Combi heat punmp and their corresponding settings.

Experiment No.	ϕ_{set} [%]	T_{set} [°C]	Duration [h]	Purpose
1	65	0	1	Study influence of relative humidity
2	75	0	1	Study influence of relative humidity
3	85	0	1	Study influence of relative humidity
4	75	-4	1	Study influence of temperature
5*	75	0	1	Study influence of temperature
6	75	4	1	Study influence of temperature
7	75	0	4	Demonstrate repetitive pattern
8	90	0	2	Study performance without defrost
9	80	3	5	Comparison of strategy
10	80	3	5	Comparison of strategy

*Experiment 5 is similar to experiment 2 and is only conducted once, but will be shown for both variations for comparison.

6.2 Experimental Set-up

The experiments on the DVI LV9 Combi heat pump are performed at DVI Energi's location in Barmer, near Nibe. DVI Energi has provided a climate chamber equipped with control units for temperature and humidity, allowing the heat pump to be tested in a controlled environment. The climate chamber is also equipped with various sensors, providing the possibility of logging data of temperatures, pressures and other relevant measurements. The evaporator is mounted on a wall with a distance of 0.3 m from the wall and 0.4 m over the floor. This allows the fan to suck in air from the backside of the evaporator and blow it out into the chamber. This is usually the way the evaporator is mounted on house walls when DVI Energi installs a heat pump at a costumer.

In order to determine the mass of frost deposited on the evaporator surface during the experiments, an open plastic box is placed on an electronic scale beneath the evaporator. This box collects the water when it drains of the evaporator surface during the defrost process. The scale can be continuously monitored throughout the experiments.

The humidity content in the climate chamber is controlled by a humidification control unit from Neptronic. The humidification control unit can supply steam to the climate chamber with a relative humidity in the range from 10% to 95%.

The temperature in the climate chamber is controlled using an electrical heating device that ensures that the temperature is kept at a specified level. As the evaporator cools the air inside the chamber, the electrical heater counters this by supplying heat to the chamber. When a defrost cycle is performed, the temperature in the chamber is raised because heat is supplied to the evaporator. It is not possible to keep the temperature at a specified level during the defrost cycles since no external cooling device is present in the chamber. After a defrost cycle, the temperature drops to the specified level when the evaporator continues normal operation and cools the air in the chamber. The set-up is illustrated in Figure 6.1.

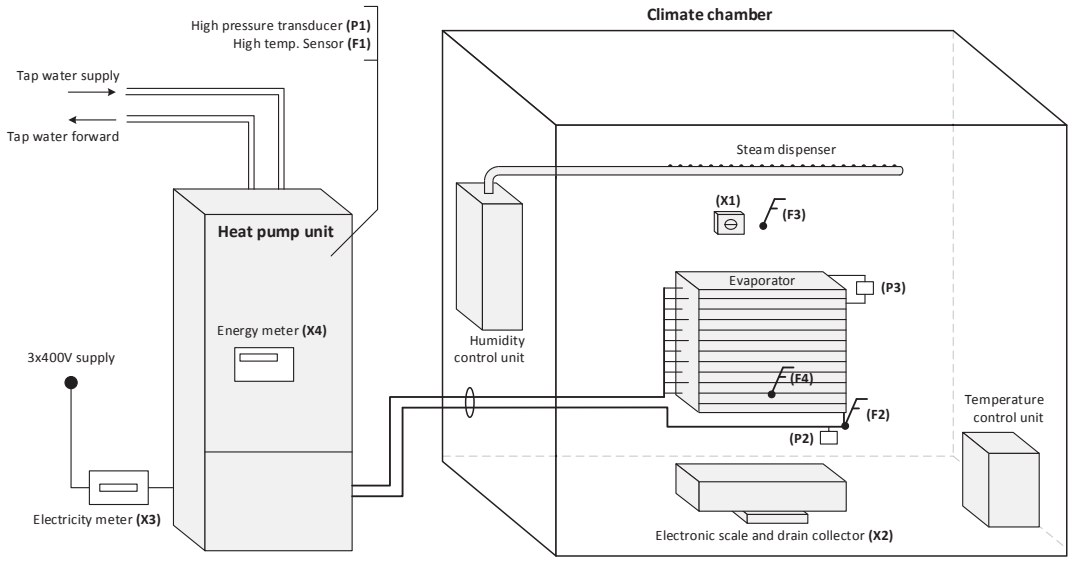

Figure 6.1. A sketch of the experimental set-up with the location of the sensors in the climate chamber and on the heat pump unit. Sensors are identified by their numbers stated in paranthesis. *F* indicates a temperature sensor, *P* indicates a pressure transducer while *X* indicates a sensor of other type.

Besides the sensors in the chamber, the heat pump unit also provides information about temperatures and pressures throughout the system. The power supply to the heat pump unit is monitored by an electricity meter with a digital pulse output. The heat delivered by the heat pump is determined by an energy meter that calculates the delivered heat from measurements on the volumetric flow rate and the temperature difference on the flow. Table 6.2 contains a list of the sensors with their location, range, and uncertainty specified. Note that the uncertainties of P1, P2 and P3 are calculated as an absolute uncertainty by using the relative full scale maximum error found in the respective data sheets. The data sheets are found on the attached CD.

Table 6.2. Sensors used during the experiment with their location, range, and uncertainty specified.

No.	Type	Location	Model	Range	Uncertainty
P1	Pressure trans.	High pressure	AKS 32	0 to 4200 kPa	±33.6 kPa
P2	Pressure trans.	Low pressure	NSK-BE010I-U009	0 to 1034 kPa	±25.85 kPa
P3	Pressure diff.	Evaporator	Prignitz DDPT	0 to 250 Pa	±6.25 Pa
F1	Temperature	High pressure	AKS 11 084N0003	-50 to 100°C	±0.5°C
F2	Temperature	Low pressure	AKS 11 084N0003	-50 to 100°C	±0.5°C
F3	Temperature	Room wall	Dixell S6 PTC	-55 to 150°C	±1.9°C
F4	Temperature	Evap. surface	Dixell S6 PTC	-55 to 150°C	±1.9°C
X1	Humidity	Room wall	Neptronic SHR10	0-100% RH	±3% RH
X2	Electronic Scale	Under drain	ITE-Tools WS-150	0-150 kg	±1%
X3	Electricity meter	Power supply	ABB DBB-23200	-	±5%
X4	Energy meter	Heat capacity	Kamstrup Multical 401	-	±2%

Calibration of Data Acquisition Equipment

To ensure the experiments to be as accurate as possible, most of the sensors are calibrated before the experiments are conducted. The temperature sensors are all calibrated by submerging them into a bowl of ice water and offset the temperature readings to zero degrees. The pressure difference sensor (P3) is calibrated by pressing the "zero-button" with the measuring channels next to each other in atmospheric pressure. The scale (X2) is calibrated by placing a known weight of 1 kg on the scale and adjusting the offset correspondingly. The humidity sensor from Neptronic was delivered factory calibrated and was further compared to a LAE HT2W humidity sensor. It has not been possible to calibrate both the high and low pressure transducers, since no pressure system with a known and accurate pressure has been available for calibration.

6.3 Experimental Approach

In this section it will be explained how the experiments are conducted. Also some practical issues and how they are solved will be addressed.

Conduction of Experiments

Before the experiments are initiated, the air temperature and relative humidity in the climate chamber are allowed to settle to a repeating pattern around the set points. The heat pump is then defrosted by using its *manual defrost* function and the data acquisition is initiated the moment the compressor starts the normal operation. All experiments are therefore initiated with a wet evaporator surface. Most of the experiments have a duration of approximately 70 minutes which corresponds to one hour of operation and a defrost process followed by three minutes of normal operation. The last three minutes of normal operation is performed in order to allow water from the defrost process to drain off the evaporator surface and into the plastic box.

Practical Issues and Solutions

In order to achieve comparable results from the experiments, it is necessary to keep some parameters constant. One of the most important parameters is the condensation temperature, which has a direct influence on the compressor performance and the exchanged energy in the condenser. It is therefore desirable to keep the condensation temperature as constant as possible to ensure that reduced performance of the heat pump is mainly a consequence of frost formation on the evaporator surface.

To keep changes in condensation temperature to a minimum, the tap water storage tank is heated to its maximum and the heat pump is set to only heat on the central heating storage tank. At the same time the central heating storage tank is cooled by exchanging with a brine that circulates through a geothermal piping system. Thereby heat is moved from the central heating storage tank to the ground at approximately the same rate as the tank is being heated. By this approach the cold inlet to the condenser (T_5) is kept close to 35°C. With a level of subcooling of approximately 3°C, this yields a condensation temperature of approximately 39°C.

Both the relative humidity and air temperature are desired to keep constant at their set points. The air temperature is controlled by an electrical heater which has a power supply connected through a temperature controlled relay. This means that every time the air temperature in the chamber drops below the set point, the heater will turn on and heat the climate chamber until the temperature is at the set point again. The humidity control unit operates in a similar way, where steam is added to the chamber when the relative humidity drops below the set point. However, because the humidity sensor has a relatively slow response time, the relative humidity in the chamber will vary around the set point. This variation is minimised by adjusting the rate of which steam is added to the chamber.

During the experiments, the evaporator performance is determined by measuring the energy delivered to the condenser and the electricity supplied to the heat pump. By assuming no heat losses in the piping system between the heat pump and the evaporator, the evaporator performance is calculated by subtracting the compressor power from the heating capacity in the condenser. The electrical energy supplied to the compressor is measured by an electricity meter mounted on the main power supply. However, other components in the heat pump also use electricity, and these will have to be accounted for when determining the compressor input power. The electrical input to the other components are determined by disconnecting the compressor and measuring the input power to the remaining system components. Other components that utilises electricity are the evaporator fan, circulation pumps and the internal control system and display.

The energy delivered by the condenser is measured by a Kamstrup Multical 401 energy meter. The energy meter is factory configured to measure megawatt-hours with three decimal points, yielding a poor resolution and accuracy for reading the heat production. Therefore, the instantaneous heating capacity of the condenser is manually read once every minute throughout the experiments, accept for the 5-hour experiments where it is read every 3 minutes. It is assumed that the heating capacity at a reading is valid for the time interval between the given reading and the previous reading.

The heat pump operates with an electronic expansion valve from Danfoss that uses the evaporation pressure and temperature of the refrigerant leaving the evaporator to control the superheat. The controller has an associated software named Minilog where it is possible to adjust the control parameters of the expansion valve. Initially it was desired to use the same control parameters as DVI Energi uses in their current heat pumps. However, the controller had difficulties keeping the reference of the level of superheat at 5°C. This resulted in a significant influence on the heat pump performance and reliability of the data measurements. It was therefore necessary to adjust the control parameters and increase the level of superheat to 6°C. This yielded a more stable control of the level of superheat, but some fluctuations were

still observed. To illustrate this, a logged session of the expansion valve control is shown in Figure 6.2 which is extracted from Minilog.

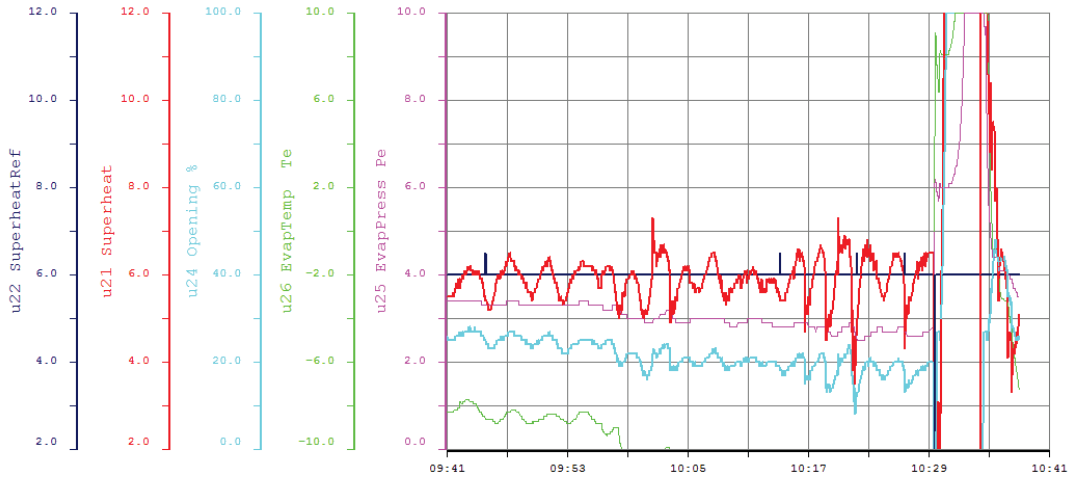

Figure 6.2. The history of the expansion valve during experiment 3, $\phi_{\text{set}} = 75\%$ and $T_{set} = 0$. The graph is printed from the associated software - Minilog.

The session is from experiment 3, $\phi_{\text{set}} = 75\%$ and $T_{\text{set}} = 0$. The red line shows the current level of superheat, the blue shows the superheat reference, and the cyan is the valve opening degree. As seen on the red line, the level of superheat has some peaks just before 10.05 and after 10.17. These fluctuations and some potential reasons for them to occur are discussed in Chapter 8.

6.4 Data Acquisition Using NI LabVIEW

When conducting the experiments in this project there is a lot of data to keep track of. It is therefore necessary to develop a data acquisition software specifically for these experiments. This software is developed using LabVIEW from National Instruments (NI). In this section it is described how the data acquisition is handled and how the user interface is designed.

Data Acquisition - Overview
The data acquisition software is developed with four purposes:

- Acquire data from the sensors and display the current values.
- Display measuring data to make it easy to monitor recent changes.
- Display timers for the total run time and time since last defrost.
- Save the data to a file that is easily managed and analysed in MATLAB.

In order to develop a software for acquiring the measurement data, it is practical to know exactly what is going to be measured, which sensors that are going to be used, and what output signals these sensors produce. Therefore, a list of all sensors and their input/output signals is created. The output signals determines what equipment that is required to perform the data acquisition. A list of sensors and their location was given in Table 6.2 in Section 6.2, while Table 6.3 is a list of the sensors, their output signals, and what unit from NI that is used to acquire the data.

Table 6.3. Sensors used in the experiment, their range, and accuracy.

Sensor No.	Output signal	Acquisition unit
P1	0.5-4.5V	NI 9215
P2	0.5-4.5V	NI 9215
P3	4-20mA (0.4-2.0V)	NI 9201
F1	843-1385Ω	NI 9219
F2	843-1385Ω	NI 9219
F3	485-2189Ω	NI 9219
F4	485-2189Ω	NI 9219
X1	0-10V	NI 9215
X2	0-30mV	NI 9211
X3	500 pulses/kWh	NI 9215
X4	Manual reading at 1 min interval	-

As seen in Table 6.3, all measuring equipment use an output signal of voltage or resistance, with the exception of the P3 sensor. However, by setting a resistor of known value in series with the P3 sensor, the output signal can be measured as a voltage difference across the resistor. Five NI units are used in total: NI 9215, NI 9219, NI 9201, NI 9211, and a NI cDAQ-9172.

Development of LabVIEW Program

Besides acquiring data, the LabVIEW program is designed with a user interface, to allow continuous monitoring of the experiment. The interface consists of numerical indicators of all data (1), graphical indicators for the data (2), timers for total run time and time since last defrost (3), and a save function (4) with enable/disable button and a LED indicator. The interface is shown in Figure 6.3.

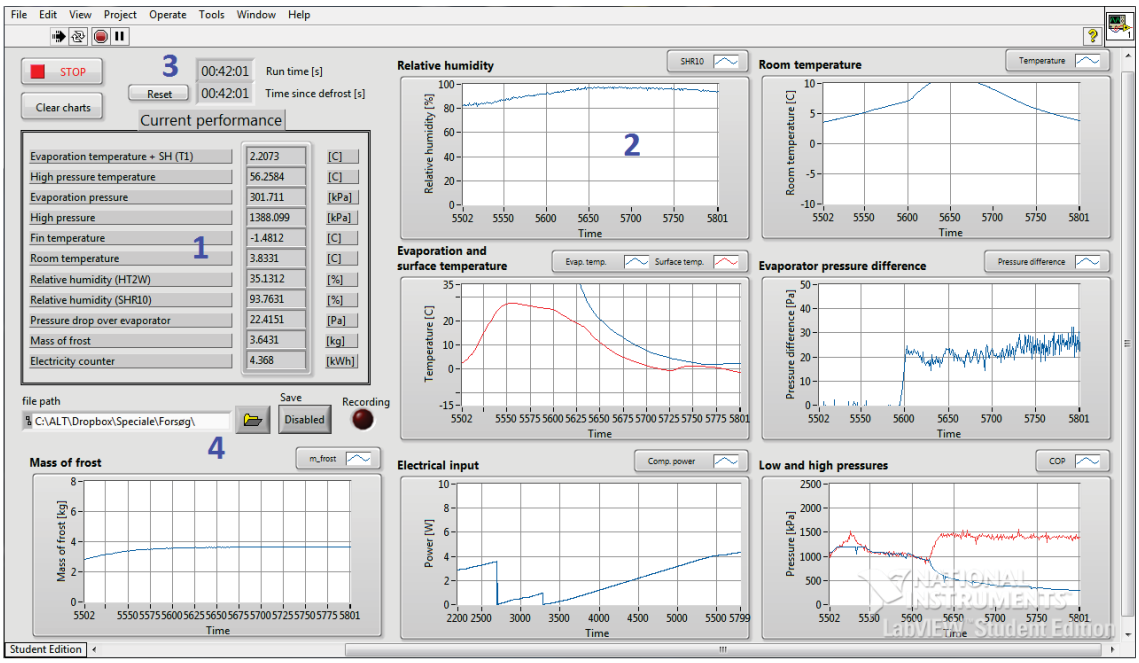

Figure 6.3. The LabVIEW user interface for monitoring data during the experiment.

Behind this interface is a program based on blocks and visual programming. All sensors have their own channel, each of which is initially set to acquire data from a specific input of a NI unit. Additionally, the signal type and the expected minimum and maximum values are set. When all channels are defined, the sample rate, sample length, and buffer size are set and the channels can be started. The data reading is done inside a while loop where each channel is treated individually. Some of the data acquisition blocks and the channel division is shown in Figure 6.4.

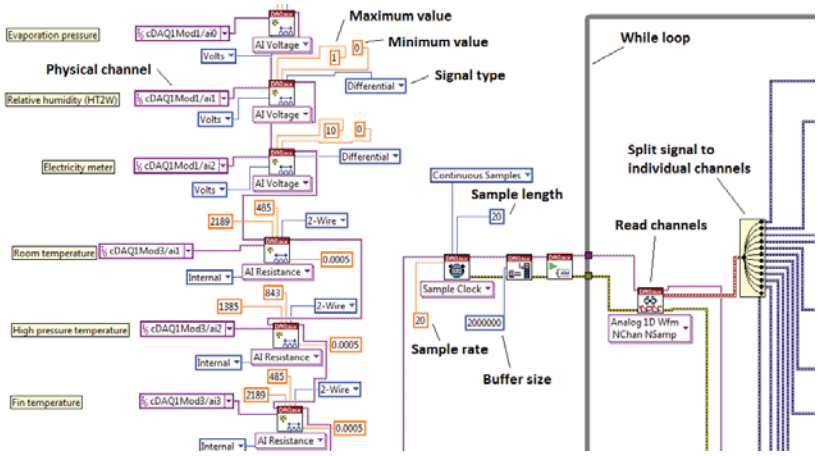

Figure 6.4. The LabVIEW data acqusition block and the signal division into seperate channels.

The data is acquired with a rate of 20Hz and length of 20 samples. After the channel division, each data channel is handled separately. Firstly, the 20 data samples are converted from the measured type (voltage or resistance) to the scaled values (temperature, pressure, humidity, etc.). For all channels, this is a linear relationship that is usually found in the data sheet. After the scaling, the 20 samples are averaged to a single value that is displayed in the numerical interface, graphical interface, and saved to the file. This yields one data point per second. The data handling is shown in Figure 6.5.

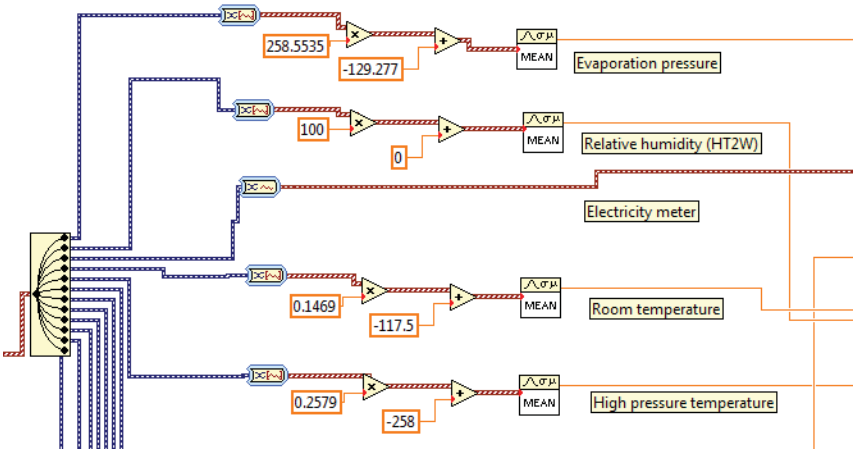

Figure 6.5. The data channels are handled separately and converted to their corresponding units.

A true/false case structure is checking if the electricity meter has send a pulse. Each pulse from the electricity meter is a relay that closes, hence the true/false statement checks if any of the 20 samples have a value less than 0.1. If this is the case, 0.002 kWh is added to the previous value of the counter. In order to analyse all the data in Matlab, each experiment can have the acquired data saved in separate .lvm files, where each column corresponds to one sensor channel. These can then easily be read and analysed in MATLAB. The electricity pulse case structure and save file structure is shown in Figure 6.6.

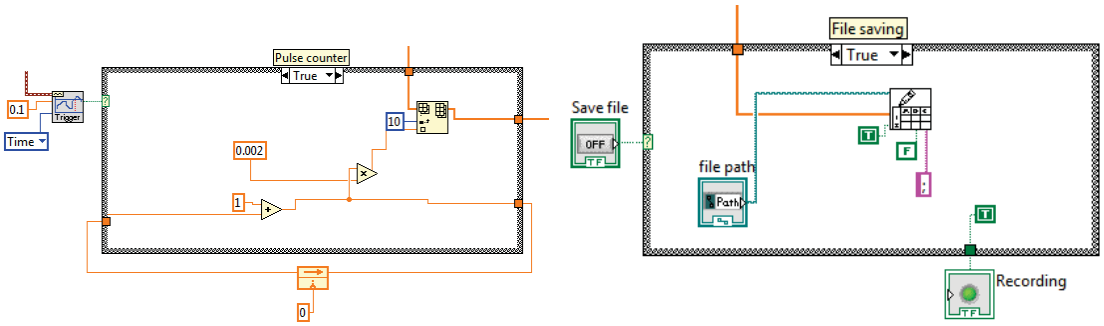

Figure 6.6. Left: Case structure checking for electricity pulse. Right: Case structure for file saving.

The complete LabVIEW software is attached on the CD.

6.5 Uncertainty Analysis

When conducting experiments there will always be uncertainties associated with the equipment. In order to evaluate the accuracy and validity of the experiments, it is necessary to quantify the influence of the uncertainties. The accuracy of all the acquisition equipment was shown in Table 6.2 in Section 6.2. Most of these accuracies are shown as absolute values, meaning that the uncertainty is in the same unit as the data reading. A large part of the data acquired in these experiments are not going to be used in calculations during the data analysis, and it is therefore relatively easy to account for these uncertainties. However, the energy meter use several sensors and a function to determine the produced heat, which makes it a more complicated matter to quantify the uncertainty. As the cooling capacity will be determined by subtracting the electrical input to the compressor from the heating capacity, this parameter will also be under the influence of several uncertainties. The uncertainty of the heating and cooling capacities will therefore be determined by the Propagation of Error method.

When calculating the propagation of error of these parameters, it is assumed that all variables are independent. It is then possible to calculate the total uncertainty on the parameter when the uncertainties of all variables are known. The errors for the individual components of the Kamstrup Multical 401 is found in the data sheet, which makes it possible to estimate the total error based on Equation (6.1). (Barry N. Taylor and Chris E. Kuyatt, 1994)

$$u = \sqrt{\left(\frac{\partial f_1}{\partial x_1}\right)^2 \Delta x_1^2 + \left(\frac{\partial f_2}{\partial x_2}\right)^2 \Delta x_2^2 \ldots + \left(\frac{\partial f_n}{\partial x_n}\right)^2 \Delta x_n^2} \tag{6.1}$$

Where:
u is the absolute standard deviation [-]
x is the variable of interest [-]
f is the function solved for the corresponding variable [-]
Δx is the absolute error of the variable [-]

The heating capacity is measured and calculated by the energy meter using Equation (6.2). Additionally the cooling capacity is found using Equation (6.3), which accounts for the electricity input to the compressor that must be subtracted.

$$\dot{Q}_{\text{heating}} = \dot{m} c_{\text{p}} \Delta T \tag{6.2}$$

$$\dot{Q}_{\text{cooling}} = \dot{m} c_{\text{p}} \Delta T - P_{\text{comp}} \tag{6.3}$$

Where:
$\dot{Q}_{\text{heating}}$ is the heating capacity [W]
$\dot{Q}_{\text{cooling}}$ is the cooling capacity [W]
$\dot{m}$ is the mass flow of water [kg/s]
c_{p} is the specific heat capacity [kJ/(kgK)]
ΔT is the temperature difference between the cold and hot flow [K]
P_{comp} is the electricity input to the compressor [W]

According to the data sheet for the Kamstrup Multical 401, the components have the following minimum accuracy at a flow of 823 L/h:

- Flow sensor: $\approx \pm 2\%$
- Calculator: $\approx \pm 1\%$
- Temperature sensor set: $\approx \pm 2\%$

Additionally, the electricity meter has a maximum error of 5%, as stated in Table 6.2 in Section 6.2. Performing the error calculation of the heating and cooling capacity yields an uncertainty of approximately 240 W and 283 W, respectively. This corresponds to 3.58% and 5.93%.

Since all other equipment has their corresponding errors stated as absolute values, it is now possible to display the uncertainties on figures with the measured data. A visual representation of the influence of the uncertainties is shown on measured data from experiment 2 in Figure 6.7.

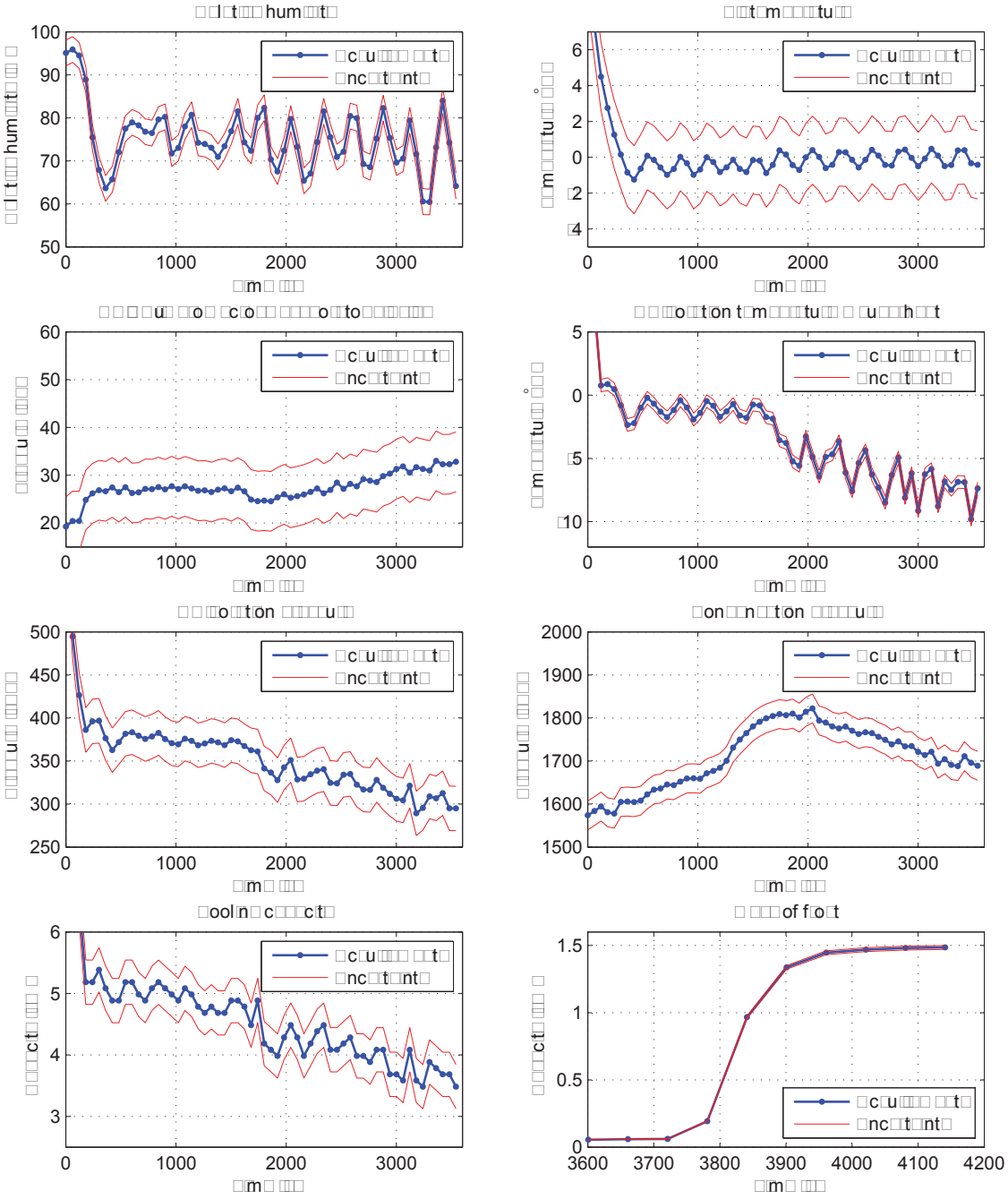

Figure 6.7. The data from experiment 2 and the corresponding uncertainties of the acquisition equipment.

Figure 6.7 clearly shows that the uncertainties are most significant on the measurements of air temperature, pressure drop, evaporation pressure, and cooling capacity. Notice that the uncertainty of the pressure drop over the air side of the evaporator is only calculated as the uncertainty regarding the measurement equipment. The location of the sensors, and the uncertainty this introduces, is therefore not account for. The uncertainties will be further discussed when comparing the experimental results to the model.

Chapter 7

Results

Results from the experiments with the DVI LV9 Combi heat pump and from the frost formation model are presented in this chapter. Firstly, results from the experiments are presented and analysed with the purpose of determining the heat pump performance under different conditions. The model is verified through experimental results, and simulation results from the model are presented and analysed. Results from experiments with the current control strategy and the control strategy given from the frost formation model are compared and analysed.

7.1 Development of Frost Layer on the Evaporator Surface

The frost formation on the evaporator surface is documented through images in the bottom of the evaporator at the air outlet side. This is done using a USB camera that takes an image with an interval of 5 minutes. The position of the image frame from the webcam is illustrated in Figure 7.1.

Figure 7.1. The position of the webcam in the bottom of the evaporator where the image frame is illustrated with the red square.

Images from an experiment with a relative humidity of 86.25% and an air temperature of 1.04°C are shown in Figure 7.2.

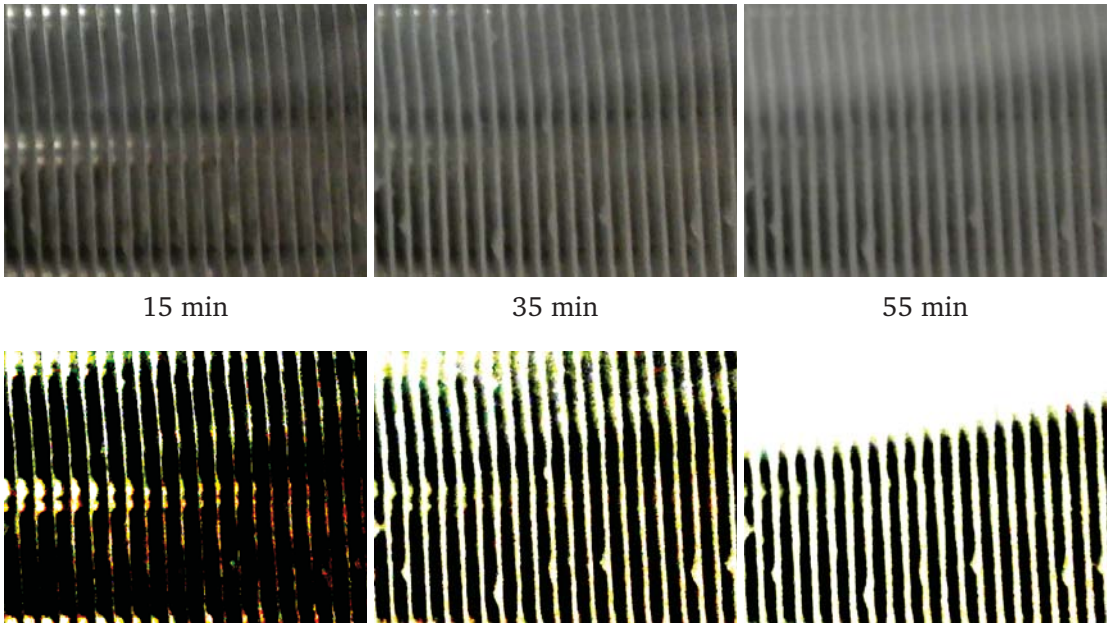

Figure 7.2. Images of the frost layer in the bottom of the evaporator taken at a 5 minutes interval at a relative humidity of 86.25% and an air temperature of 1.04°C. The upper three images are original, while the lower three images are post processed. Notice that the white shadow in the post processed image at 55 min is casued by frost on the fan blades.

The images in Figure 7.2 are taken after 15 minutes, 35 minutes and 55 minutes respectively. Thee upper images are the original ones and the lower images are the same images, but where contrast and brightness has been adjusted so that the frost layer is more visual.

At 0 minutes, some droplets are still falling off the evaporator surface after the defrost process that was executed just before the images were taken. Already after 5 minutes, these droplets refreeze on the evaporator surface, indicating that a fraction of the frost remains on the evaporator surface after a defrost process. A frost layer starts to build up on the evaporator fins and tubes. As time passes, the frost layer grows and the images gets more and more blurred with a white colour which is due to frost on the fan blades. The frost layer thickness seems to have a variation where the thickness increases in the bottom of the evaporator. This is observed to be a clear tendency both through the images and trough visual observations of the evaporator. The frost formation on the tubes seems to be most significant on the upstream side of the tubes, compared to the downstream side which is the side that is visualized in the images.

A comparison of the frost layer thickness is done for relative humidities of 65.97%, 75.19% and 86.25% and air temperatures of -0.25°C, 0.21°C and 1.04°C respectively. It was intended to keep the relative humidities at 65%, 75% and 85%, but the on/off control of the humidity controller caused a slight variation. The air temperature was set to 0°C, but a small variation was obtained for the air temperatures as well, due to the on/off control of the electric heater. For these scenarios, images were taken after 55 minutes. The images are shown in Figure 7.3

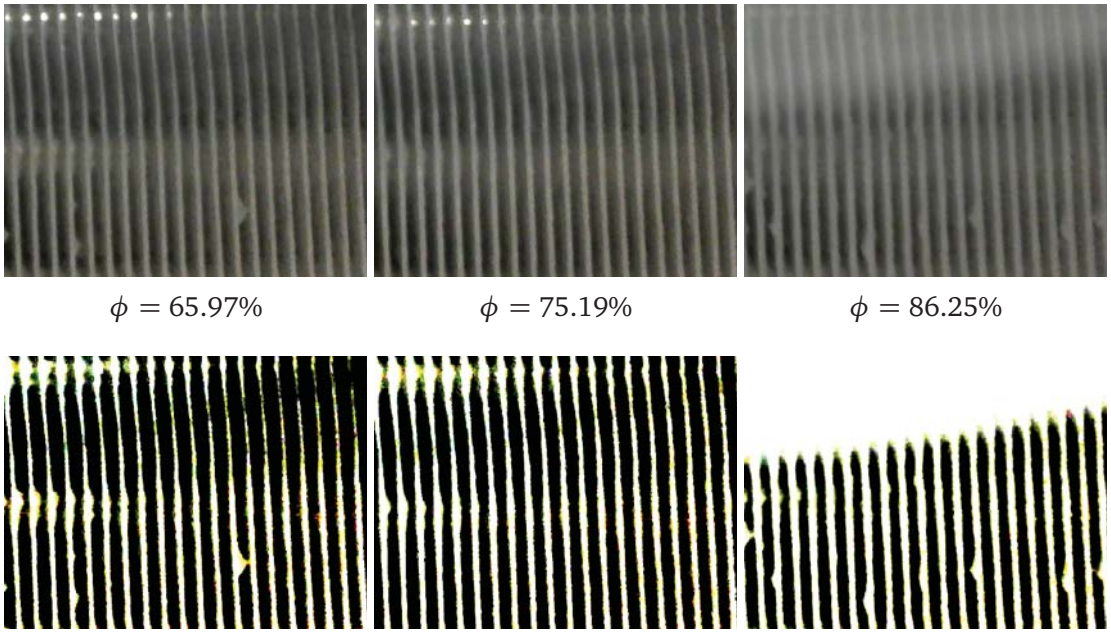

Figure 7.3. Images of the frost layer in the bottom of the evaporator at relative humidities of 65.97%, 75.19% and 86.25% and air temperatures of -0.25°C, 0.21°C and 1.04°C respectively. The upper three images are original, while the lower three images are post processed. Notice that the white shadow in the post processed image at $\phi = 86.25\%$ is casued by frost on the fan blades.

The frost thickness seems to increase as the relative humidity is increased. This is expected since the absolute humidity increases in the air flow when the relative humidity is increased, hence more water vapour is carried in the air flow that passes through the evaporator.

7.2 Experimental Results for Repetitive Defrost Cycles

An experiment with four defrost cycles is conducted in order to investigate the performance behaviour when multiple defrost cycles are repeated. The experiment is performed with an average relative humidity of 75.61% and an average air temperature of -0.44°C. The data presented for this experiment are mean values where one data point is a mean value of 60 measurements in order to lower the number of data points. The experiment is started immediately after a defrost cycle has finished and is continued for four defrost cycles and ended a few minutes after the last defrost cycle. Figure 7.4 shows results from the experiment for air temperature, relative humidity and mass of frost.

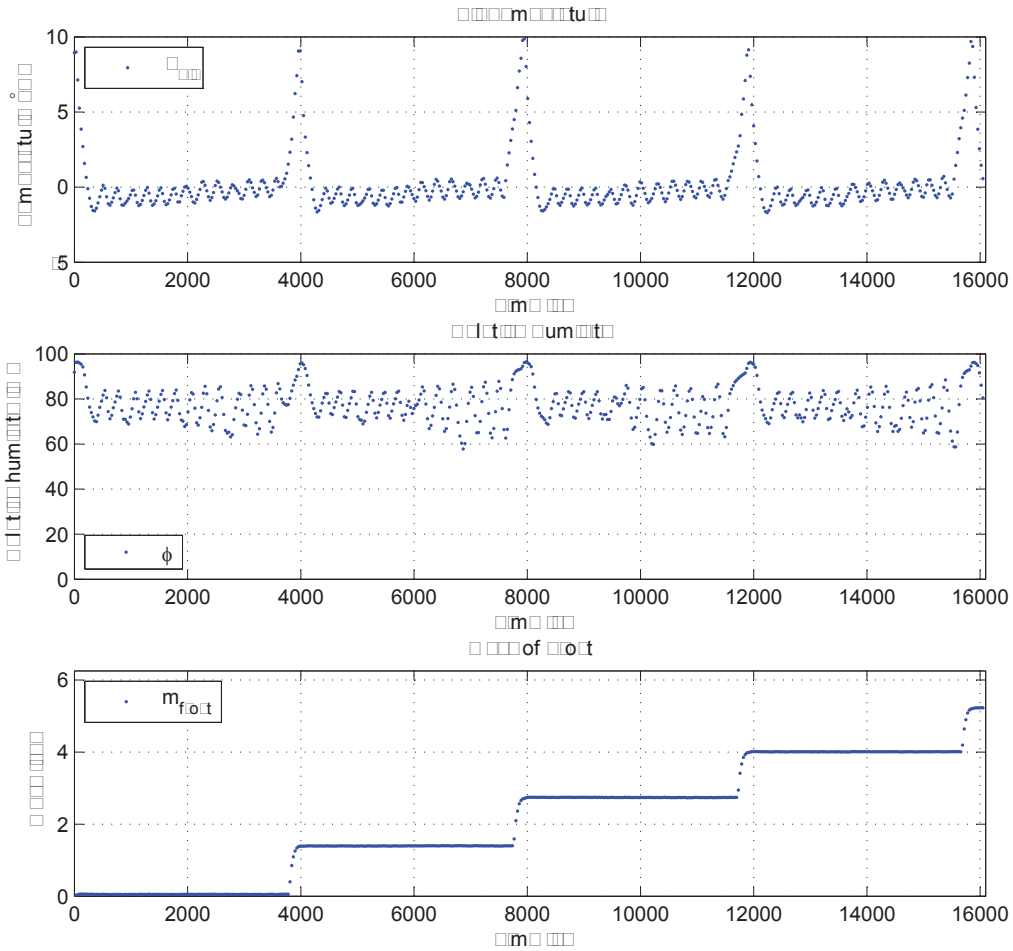

Figure 7.4. Air temperature, relative humidity and mass of frost for four defrost cycles at an average relative humidity of 75.61% and an average air temperature of -0.44°C.

The results in Figure 7.4 clearly indicates that there is a cyclic behaviour for the four cycles. The relative humidity has some variations around the mean of 75.61%. These variations are caused by the humidity control unit which attempts to keep the relative humidity constant using an on/off regulation. The air temperature also show some variations which is caused by both the humidity control unit, the evaporator and the electrical heater. The humidity control unit supplies hot steam to the climate chamber, the evaporator cools the air flow through it and the electrical heater compensates for the temperature drop caused by the evaporator using an on/off control. During the defrost cycles, the relative humidity increases because the defrost process results in evaporation of some of the frost. The air temperature also increases during defrost which is caused by the heat release that occurs during the melting process of frost. In this period, no cooling is supplied to the room because the evaporator is in defrost mode. After the defrost period, both the relative humidity and air temperature drops to the same level as before the defrost process.

The mass of frost is weighed during the four hour experiment which results in a frost mass increase each time a defrost cycle is performed. The difference in the mass of frost is relatively constant between the cycles. The mass of frost for each cycle is plotted in Figure 7.5 in order to compare the measurements.

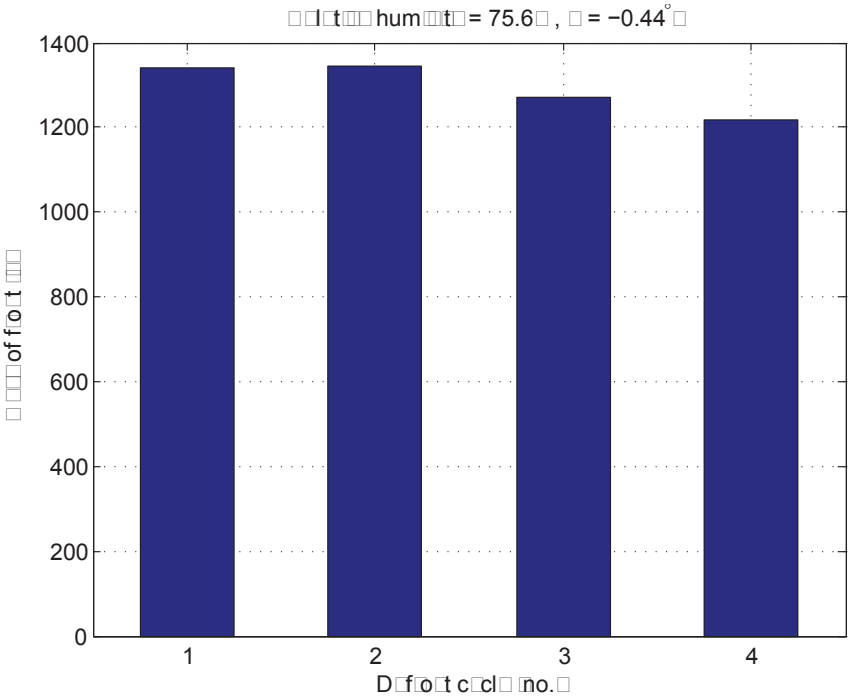

Figure 7.5. The mass of frost for the four defrost cycles.

There is a small deviation between the four cycles where most mass of frost is obtained in the two first cycles, while it decreases slightly in the two last cycles. The frost masses are 1341 g, 1345 g, 1270 g and 1217 g for the four cycles respectively. The average mass of frost is 1293 g while the standard deviation is 61 g which corresponds to an average deviation of 4.7%. There is a tendency for the mass of frost to decrease slightly for the different defrost cycles, but this might be random. More cycles should be performed in order to ensure that random deviations are eliminated in order to yield a clear pattern.

Figure 7.6 shows the results from the experiment for evaporation and condensation pressures, evaporator pressure difference and evaporator temperatures.

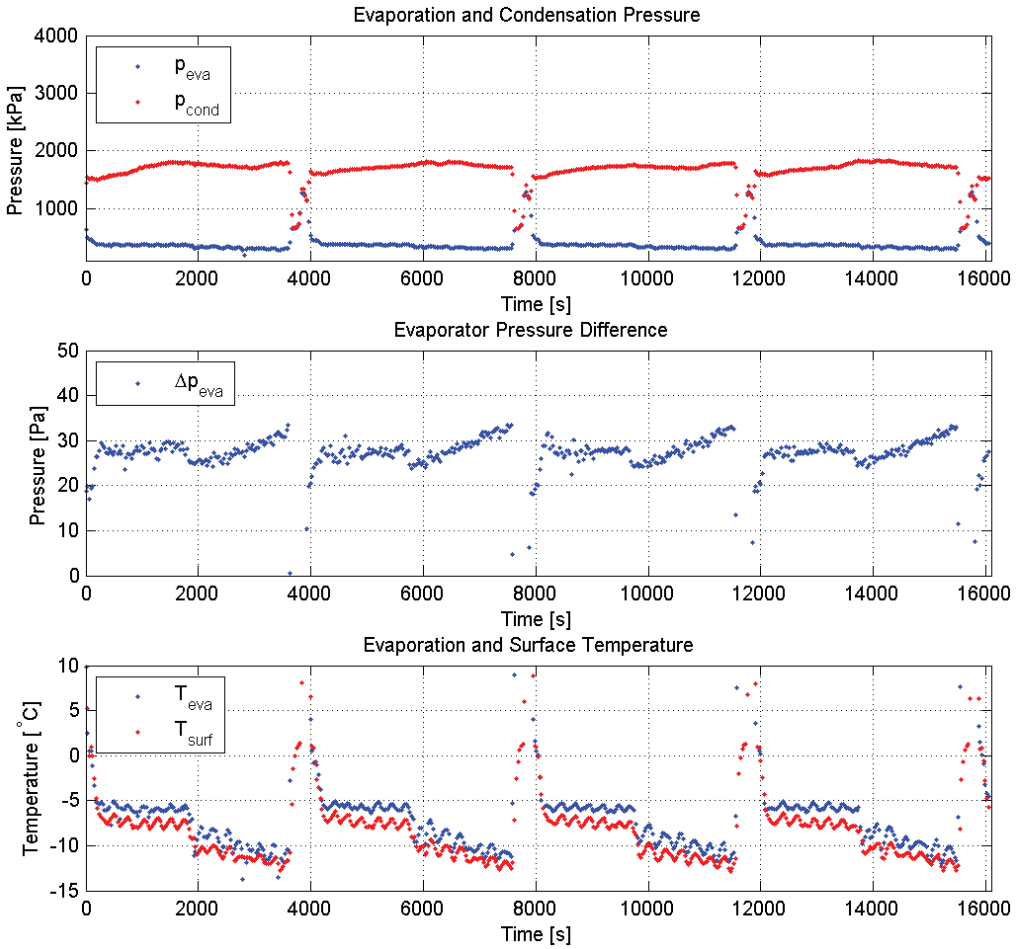

Figure 7.6. Pressures and temperatures for four defrost cycles at an average relative humidity of 75.61% and an average air temperature of -0.44°C.

Again, the results show a cyclic behaviour where the pattern is repeated in the four cycles. The evaporation pressure decreases slightly through the periods with normal operation, and during the defrost periods the evaporation pressure increases because hot refrigerant is passed through the evaporator tubes in order to melt the frost. The condensation pressure increases slightly during the operation period. During the defrost process, the 4-way valve is reversed, causing the high and low pressure transducers to measure on the same pipeline. These pressure transducers are placed at the same location as component 16 and 17 in Figure 3.1 in Section 3.1. The slight increase in condensation pressure and drop in evaporation pressure during the operation periods are caused by the expansion valve which reduces the opening degree in order to maintain a level of superheat of 6°C by lowering the mass flow rate of refrigerant.

The pressure difference over the evaporator air side has very large fluctuations in the beginning of each period, which causes the mean value to be high. Approximately half way though the operation periods, the pressure seems to have a sudden drop and a more clear behaviour until defrost is initiated. There can be several reasons to the fluctuations and one is expected to be changes in the flow velocity. This will be further discussed in Chapter 8. It should also be noted that the pressure difference measured is in the range of 35 Pa or

less which is a relatively low pressure. Small disturbances or fluctuations in the measuring equipment or in the air flow might easily cause a deviation. The general increase in pressure difference indicates that the frost layer increases on the evaporator surface over time which gradually blocks the air-passage in the evaporator.

The evaporation temperature is found by subtracting the level of superheat from the temperature measured on the refrigerant tube at the evaporator outlet. The evaporation temperature varies as a results of the valve control. The same does the surface temperature on the evaporator. The variations in the temperatures increase in the last part of the periods which indicates that the over- and undershoot around the superheat reference increases. Generally, the temperatures decrease with time which is a direct result of frost on the evaporator surface which means that the superheat can only be maintained by lowering the mass flow rate of refrigerant through the evaporator due to a decreased performance.

7.3 Experimental Results Without Defrosting

An experiment was conducted where defrosting was manually turned off in order to investigate the performance degradation when the heat pump was operating for more than one hour at frost conditions. A two hour experiment was performed at an average relative humidity of 88.48% and an average air temperature of 0.65°C. The set points were 90% relative humidity and 0°C air temperature.

The cooling capacity and the difference between air temperature and evaporation temperature are calculated from measurements. The cooling capacity is found by subtracting the measured electricity consumed by the compressor from the measured heating capacity of the condenser. The difference between air temperature and evaporation temperature is found by subtracting the measured evaporation temperature from the measured air temperature. The cooling capacity and the difference between air temperature and evaporation temperature are plotted in Figure 7.7.

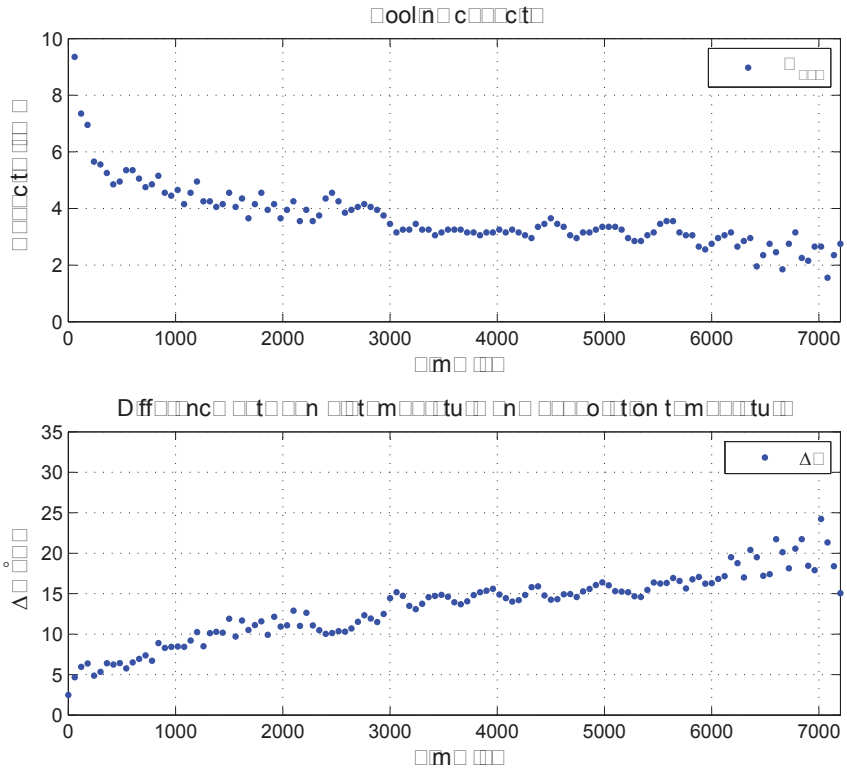

Figure 7.7. Cooling capacity and difference between air temperature and evaporation temperature from a two hour experiment without defrosting.

The cooling capacity shown in the upper part of Figure 7.7 decreases with time and therefore with the increasing amount of frost that deposits over time. The cooling capacity is approximately 5.6 kW after the initial period where the expansion valve controller reaches steady operation at a superheat reference of 6°C. After two hours, the cooling capacity drops to approximately 2.3 kW which corresponds to a degradation of approximately 59%. The degradation is approximately 42% after one hour of operation.

The temperature difference shown in the lower part of Figure 7.7 increases with time. This means that the evaporation temperature drops with time which is a direct consequence of frost formation on the evaporator surface which forces the expansion valve controller to lower the mass flow rate of refrigerant in order to maintain the superheat reference. Using this temperature difference to determine the defrost point might be a good practical solution for DVI Energi. This is the temperature difference that both Danfoss and Bosch Termoteknik use to identify the need of a defrost process.

The mass of frost drained of the evaporator at the defrost after the two hour experiment yielded a mass of 3227 g.

7.4 Experimental Results at Varied Relative Humidity and Constant Air Temperature

Experimental results with the DVI LV9 Combi heat pump at varied relative humidity and constant air temperature are presented in this section. Three different relative humidities were tested at an air temperature of approximately 0°C. The relative humidities tested were set to 65%, 75%, and 85%. It was not possible to keep the air temperature and the relative humidities perfectly constant, hence the measured relative humidities deviated slightly. The settings and average values obtained during the experiments are given in Table 7.1. Note that ET corresponds to evaporation temperature and SH corresponds to level of superheat.

Table 7.1. The experiments and their set points.

Exp. no.	ϕ_{set} [%]	ϕ_{avg} [%]	T_{set} [°C]	T_{avg} [°C]	ET_{avg} [°C]	SH_{avg} [°C]
1 (△)	65	65.97	0	-0.25	-8.61	4.72
2 (□)	75	75.19	0	0.21	-7.98	4.02
3 (○)	85	86.25	0	1.04	-9.81	4.51

The results shown in this section are for cooling capacity, pressure difference across the evaporator air side, evaporation temperature, difference between air temperature and evaporation temperature, and the mass of frost. These results are either directly measured or calculated based on other measured parameters. In order to reduce the data, the evaporator pressure difference, evaporation temperature, and difference between air temperature and evaporation temperature are plotted as mean values for each minute of the raw data points measured during the experiments. One data point in the plots is therefore a mean value of 60 raw data points. The raw data is presented in Appendix D. The cooling capacities are manually read every 60 second during the experiments and all data points are therefore shown.

The cooling capacity is found by subtracting the measured electricity input to the compressor from the measured heat capacity of the condenser. The pressure difference across the evaporator air side is measured directly. The evaporation temperature is found by measuring the evaporation pressure and calculating the evaporation temperature from the properties for R407c using EES. The difference between air temperature and evaporation temperature is found by subtracting the measured air temperature from the evaporation temperature found using EES. The cooling capacity and evaporator pressure difference are shown in Figure 7.8.

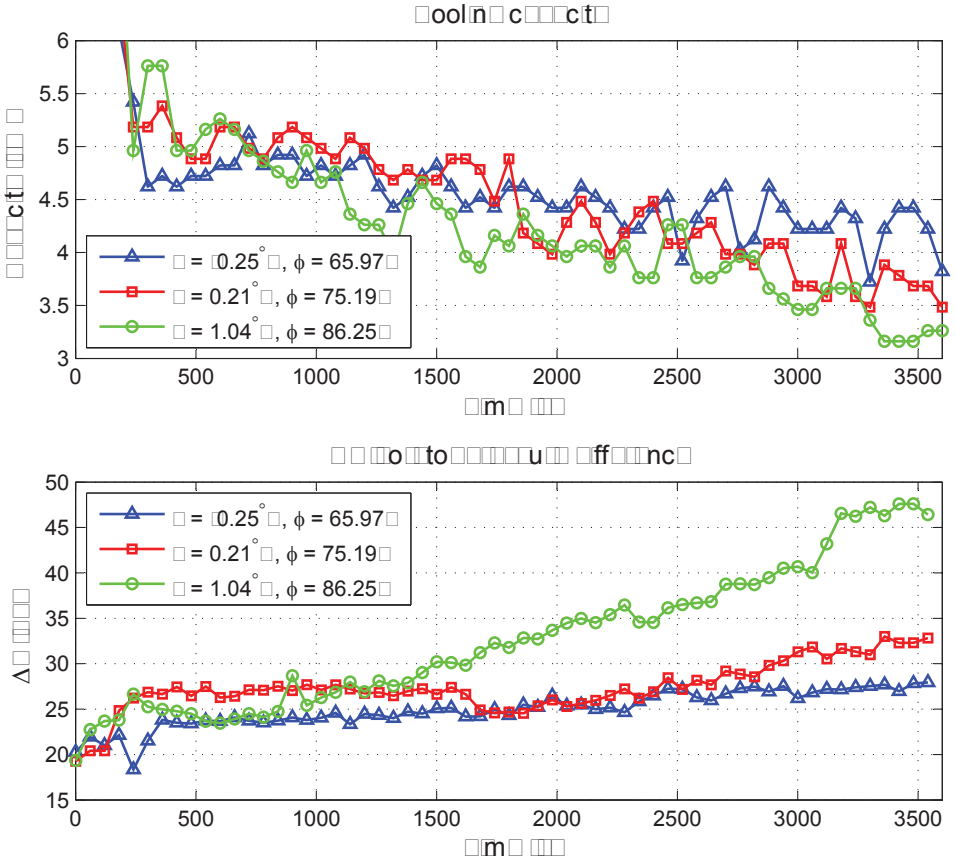

Figure 7.8. Results of the three experiments with varied relative humidity and constant air temperature. The graphs show the cooling capacity and the pressure drop over the evaporator air side.

The cooling capacities are plotted in the upper part of Figure 7.8. The fluctuations in the graphs are due to the expansion valve control which alternately over- and undershoots the level of superheat around its reference point. This tendency was previously shown in Figure 6.2 in Section 6.2. This causes the cooling capacity to vary with the mass flow rate of refrigerant. The main observation is that a higher relative humidity results in a lower cooling capacity after one hour. The cooling capacities generally seems to fluctuate around the 4.5-5.0 kW after the superheat has reached its reference and the heat pump operates steadily at 500 to 1500 seconds. The cooling capacity decreases with time as frost is deposited on the evaporator surface, and the difference in humidity seems to cause the curves to separate.

The evaporator pressure difference over the air side of the evaporator is plotted in the lower part of Figure 7.8. The pressure difference generally increases with time, and it is clear that increased relative humidity leads to increased pressure difference, indicating that more frost blocks the evaporator air side flow channels. The pressure drop increases with time and has a tendency which is close to linear for the pressure drops at relative humidities of 65.97% and 86.25%. The pressure drop at a relative humidity of 75.19% has a sudden reduction just after 1500 seconds of the experiment which is unexpected and might be a result of disturbance on the measuring equipment.

The evaporation temperature and the difference between air temperature and evaporation temperature are shown in Figure 7.9.

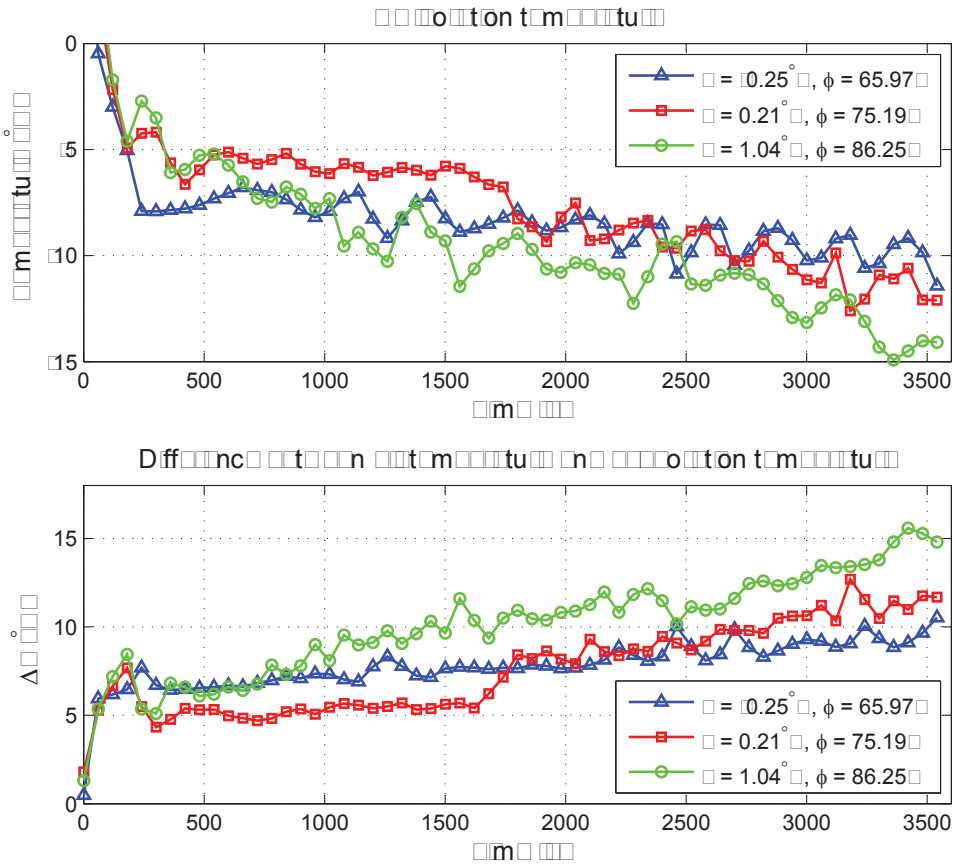

Figure 7.9. Results of the three experiments with varied relative humidity and constant air temperature. The graphs show evaporation temperature converted from the evaporation pressure and the temperature difference between air temperature and evaporation temperature.

The evaporation temperature shown in the upper part of Figure 7.9 decreases with time and frost formation on the evaporator surface. This is a result of the expansion valve slowly reducing the refrigerant flow to counteract the reduced exchange of energy. An increased relative humidity yields a decrease in evaporation temperature after one hour. A lowered cooling capacity occurs due to a lower evaporation temperature which results in a reduced performance.

The temperature difference between air temperature and evaporation temperature, shown in the lower part of Figure 7.9, increases with time. After the expansion valve controller has settled and stability in the temperature difference is obtained, there is a more or less constant temperature difference for all three scenarios for some time. The first curve that has an increase in the temperature difference is the scenario with the highest relative humidity of 86.25%. The next curve that has a significant increase in temperature difference is the red curve which is the scenario with 75.19% relative humidity. The blue curve, which is for a relative humidity of 65.97%, has a slight increase throughout the time of the experiment with some fluctuations in the last 25 minutes. These trends indicate that an increased relative

humidity results in an increased temperature difference at an earlier stage of the experiments than at lower relative humidities.

The mass of frost from the three experiments are shown in Figure 7.10.

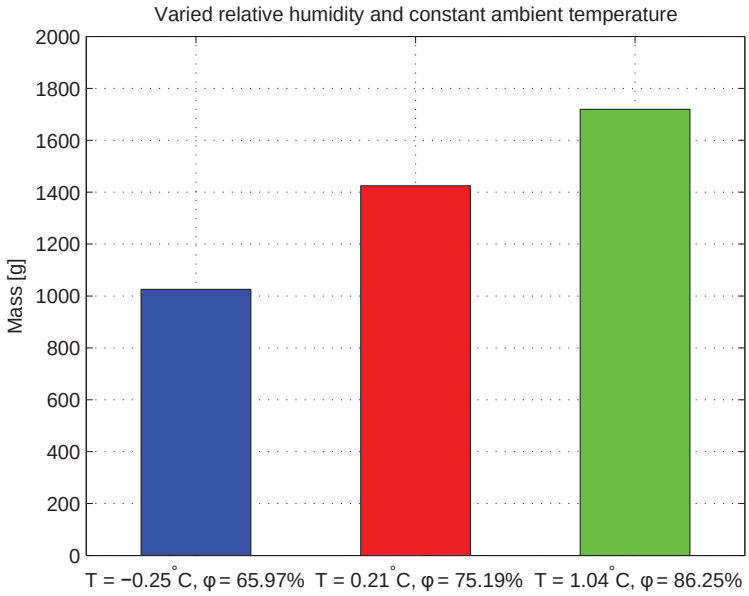

Figure 7.10. Mass of frost for the three experiments at varied relative humidities and constant air temperature.

As seen in Figure 7.10, the mass of frost increases with increased relative humidity as expected. The masses are measured to approximately 1026 g, 1425 g, and 1719 g respectively. It should be noted that the masses are found only for the water that drains of the evaporator. Water that remains on the evaporator and refreeze when normal operation is started and frost that evaporates during the defrost process causes an offset between the actual mass of frost and the measured mass of frost.

7.5 Experimental Results at Varied Air Temperature and Constant Relative Humidity

In this section, the results of the experiments with varied air temperature and constant relative humidity are presented. The relative humidity set point is held at 75%, while the air temperatures are set to -4°C, 0°C, and 4°C. According to DVI Energi, the frost formation issue starts around 4°C, hence this is chosen as the upper limit for these experiments. As mentioned, there were problems keeping the relative humidity and temperature perfectly constant which resulted in slight deviations from the set points. The settings and average values obtained during the experiments are given in Table 7.2 Notice that experiment 5 is the same as experiment 2, but is shown again for comparison purpose.

Table 7.2. The experiments and their set points.

Exp. no.	ϕ_{set} [%]	ϕ_{avg} [%]	T_{set} [°C]	T_{avg} [°C]	ET_{avg} [°C]	SH_{avg} [°C]
4 (×)	75	76.89	-4	-3.51	-10.71	4.17
5 (□)	75	75.19	0	0.21	-7.98	4.02
6 (◇)	75	74.83	4	3.75	-4.72	4.10

The results shown in this section are for cooling capacity, evaporator pressure difference, evaporation temperature, and temperature difference between air temperature and evaporation temperature, as in the previous section, hence these results are found and treated in the same way. The cooling capacity and evaporator pressure difference are shown in Figure 7.11.

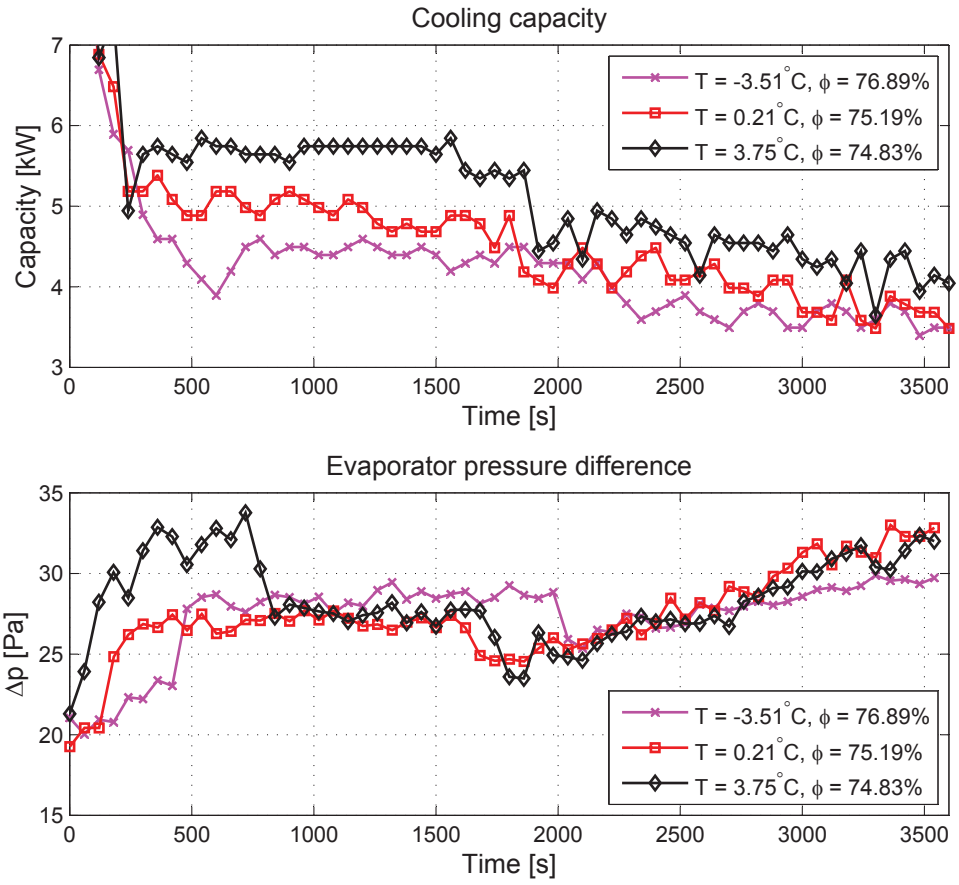

Figure 7.11. Results of the three experiments with varied air temperature and constant relative humidity. The graphs show the cooling capacity and the pressure drop over the evaporator air side.

The cooling capacities shown in the upper part of Figure 7.11 decreases with time, which was also the case for the scenarios with varied relative humidity and constant air temperature. The cooling capacities show an increased level of fluctuations after approximately 2000 seconds which indicate that the expansion valve controller has difficulties in maintaining superheat at the reference point. The cooling capacities has a slightly steeper gradient over time as the air temperature is increased, indicating that more frost is deposited at higher temperatures. This is expected, since the absolute humidity in the air increases with the temperature at constant

relative humidity. The lowest cooling capacity is obtained for the lowest air temperature of -3.51°C, except for some periods where the cooling capacity at an air temperature of 0.21°C is lower. This might be due to the fluctuations caused by the expansion valve controller. The highest cooling capacity is obtained at the highest air temperature. The reason for this relationship is that a lower air temperature yields a lower evaporation temperature and therefore a lower cooling capacity.

The pressure differences across the evaporator air side is shown in the lower part of Figure 7.11. The evaporator pressure differences have some unexpected behaviours in the first 2000 seconds after which the pressures seem to drop. This was also observed in other experiments and could be caused by changes in the flow velocity. After one hour, the lowest air temperature of -3.51°C yields the lowest pressure drop. The pressure drop for 0.21°C is slightly higher than for 3.75°C after one hour which is not expected since more frost is expected to formate at the air temperature of 3.75°C. The difference in pressure is very low and the uncertainty on the measuring equipment might affect the results.

The evaporation temperature and the temperature difference between air temperature and evaporation temperature are shown in Figure 7.9.

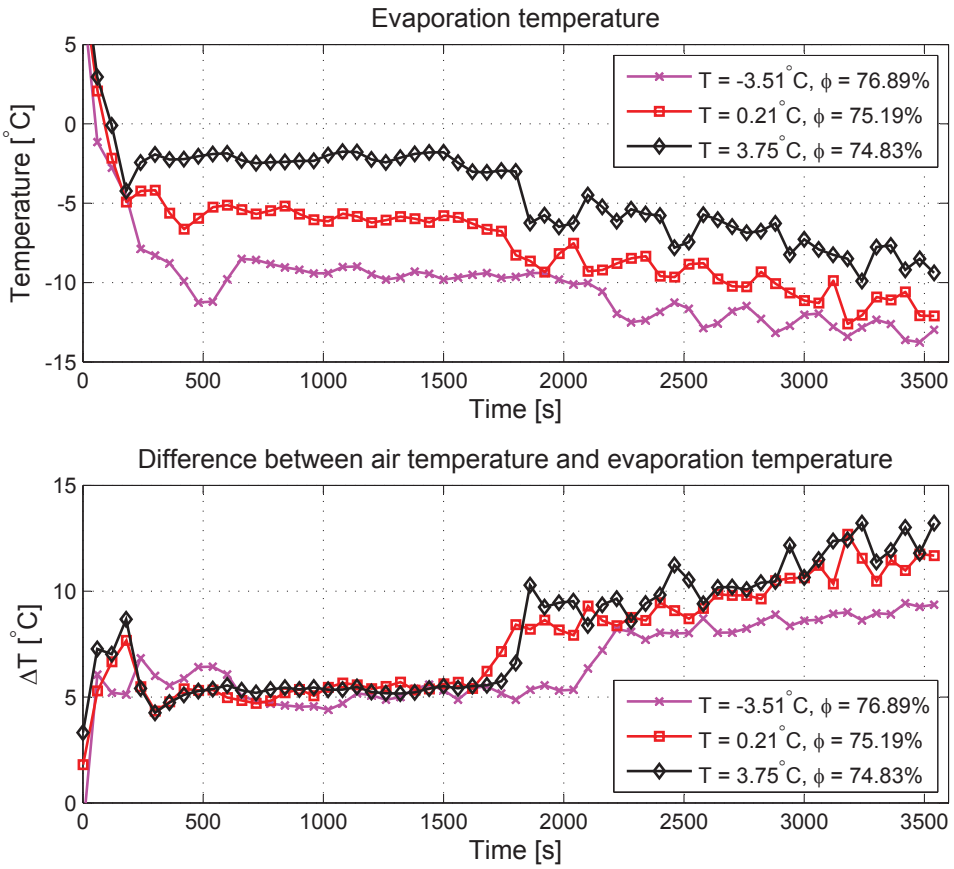

Figure 7.12. Results of the three experiments with varied air temperature and constant relative humidity. The graphs show evaporation temperature converted from the evaporation pressure and the temperature difference between air temperature and evaporation temperature.

The evaporation temperatures are plotted in the upper part of Figure 7.12. A lower air temperature yields a lower evaporation temperature which is expected. The evaporation temperature drops with time which is a result of the frost formation on the evaporator surface that affects the evaporation temperature. The evaporation temperature is more or less constant the first 1800 seconds after which it drops while having some more significant fluctuations.

The temperature difference between air temperature and evaporation temperature is shown in the lower part of Figure 7.12. The temperature difference is more or less constant in the first 1800 seconds which is a direct consequence of the evaporation temperature tendency. After this point there is a significant temperature increase for all three experiments. The increase occurs slightly later for the experiment at the lowest temperature. Generally, the temperature difference increases with increased air temperature which indicates that more frost on the evaporator yields a higher temperature difference.

The mass of frost from the three experiments are shown in Figure 7.13.

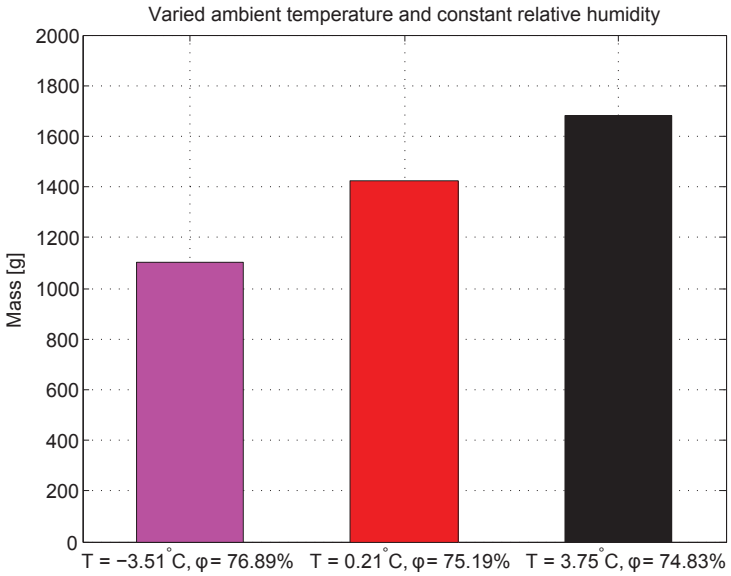

Figure 7.13. Mass of frost for the three experiments at varied air temperatures and constant relative humidity.

As seen in Figure 7.13, the mass of frost increases with increased air temperature. The reason for this relationship is that a higher air temperature yields a higher water vapour pressure and therefore a higher absolute humidity when the relative humidity is kept constant. The masses are measured to approximately 1102 g, 1425 g, and 1682 g respectively.

7.6 Model Validation

The purpose of this section is to validate the frost formation model by comparing experimental data with results of the model. This is done for the the cooling capacity and the evaporator pressure difference for the experiments presented in Section 7.4 and 7.5. The model results are performed at the same conditions as the experimental results, hence temperatures, relative humidities, evaporation temperature, and superheat are set according to the average

values measured during the experiments. The model results are performed with the frost conductivity correlation that yields the best consistency with the experimental results. The different cases and the correlations used are given below.

- Experiment 1 (△): Östin & Anderson (1991)
- Experiment 2 (□): Sturm (1997)
- Experiment 3 (○): Sturm (1997)
- Experiment 4 (×): Yonko & Sepsy (1967)
- Experiment 5 (□): Sturm (1997)
- Experiment 6 (◇): Sturm (1997)

In order to ensure that the masses of frost are consistent for model and experiment, the point x_f is set so that the masses correspond. The accuracy of this approach is determined by the value of x_f which is adjusted and rounded to an integer value in millimetres.

Validation of Results at Varied Relative Humidity and Constant Air Temperature
The cooling capacities for the experiments and the model simulations at varied relative humidity and constant air temperature are shown in Figure 7.14.

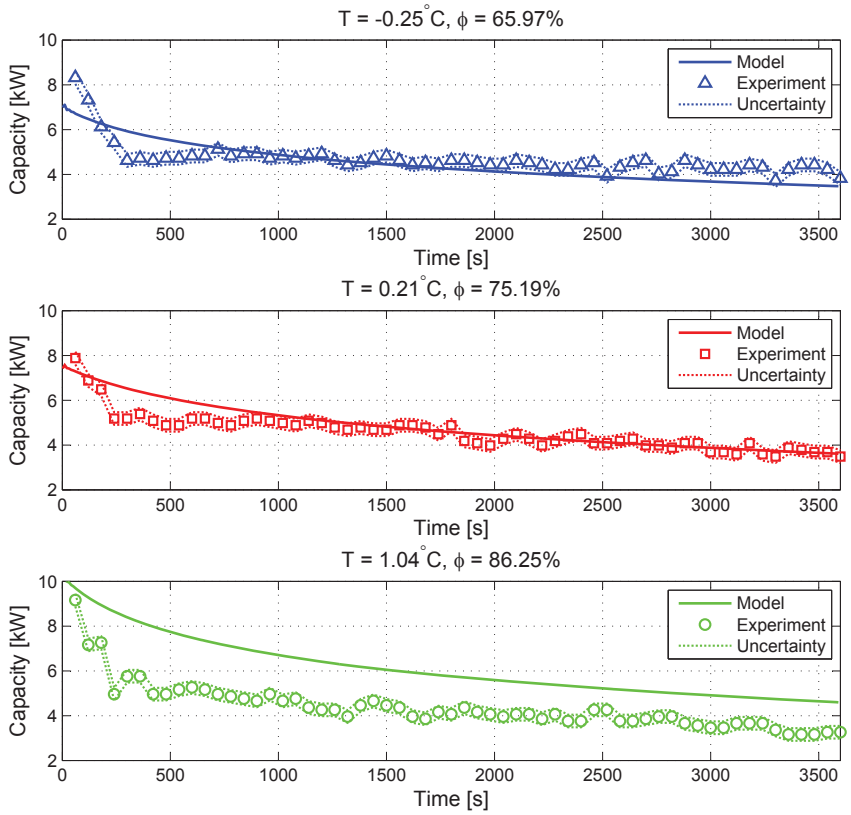

Figure 7.14. Validation of modelled cooling capacity at varied relative humidity and constant air temperature.

The simulated cooling capacity for $\phi = 65.97\%$ starts at approximately 7 kW and drops to approximately 3.5 kW after one hour. The simulated performance is overestimated by the model in the first 700 seconds, except for the initial period. After this point, the simulated

performance is consistent with the experimental results until at approximately 1700 seconds. After this point the simulated performance is underestimated due to a steeper gradient than for the experimental result. The simulated cooling capacity for $\phi = 75.19\%$ overestimates the performance in the first 1000 seconds where after it is consistent with the experimental result. The simulated cooling capacity for $\phi = 86.25\%$ overestimates the performance for the entire simulation period, but has the correct tendency. In general, the experimental data deviates more in the beginning of the periods due to the expansion valve fluctuating around the superheat reference point. Except for this deviation in the beginning of the period, the experimental data and simulation generally seem to have a similar behaviour, though a larger amount of frost seems to cause the model to overestimate the performance. Possible reasons for this will be further discussed in Chapter 8.

The pressure drop over the evaporator for the experiments and model simulations with varied relative humidity and constant air temperature are shown in Figure 7.15.

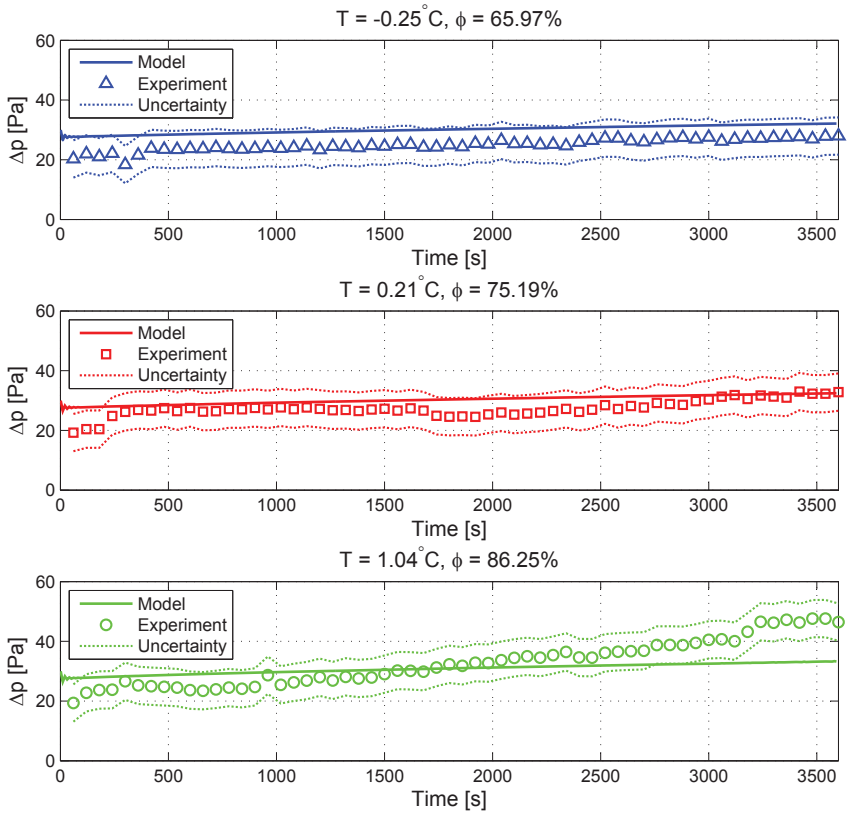

Figure 7.15. Validation of modelled evaporator pressure difference at varied relative humidity and constant air temperature.

The pressure drop over the evaporator seems consistent for the cases with $\phi = 65.97\%$ and $\phi = 75.19\%$ with only minor deviations. The pressure drop at $\phi = 86.25\%$ is within the uncertainty for most of the period, but the experimental results has a more increasing tendency than the model predicts. Since both the temperature and humidity is higher for this experiment than the two others it is expected that more frost will develop and lead to increased pressure drop. The increase from $\phi = 75.19\%$ to $\phi = 86.25\%$ however, is far more significant than that from $\phi = 65.97\%$ to $\phi = 75.19\%$, which might be related to the increase

in temperature and absolute humidity. The simulation for the case of $\phi = 86.25\%$ does not show the larger amount of frost to cause a significantly higher pressure drop. This might be caused by the correlation for frost density and thermal conductivity. This will be further discussed in Chapter 8.

Validation of Results at Varied Air Temperature and Constant Relative Humidity
The cooling capacities for the experiments and model simulations at varied air temperature and constant relative humidity are shown in Figure 7.16.

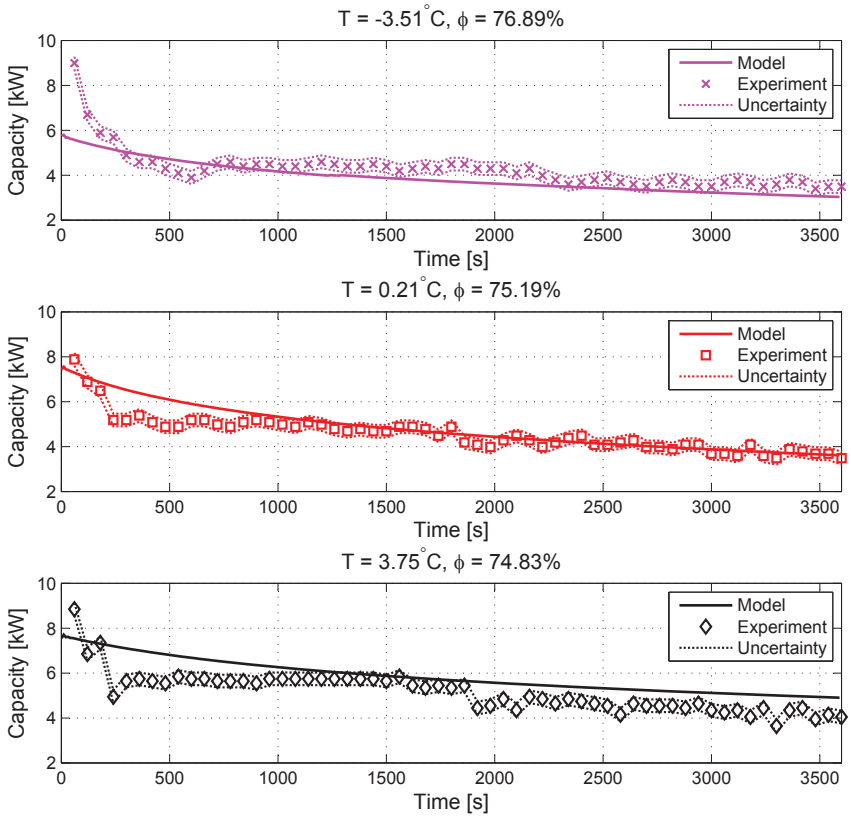

Figure 7.16. Validation of modelled cooling capacity at varied air temperature and constant relative humidity.

The cooling capacities simulated by the model generally show a similar pattern to that of the varied relative humidity. More frost is expected to develop as the temperature increases due to increased absolute humidity. In the case with T = -3.51°C, the model show decent accuracy, but generally underestimates the performance. The case for T = 0.21°C is the same case as previously shown. For the case with T = 3.75°C, where most frost is expected, the model generally overestimates.

The pressure drop over the evaporator for the experiments and model simulations with varied air temperature and constant relative humidity are shown in Figure 7.17.

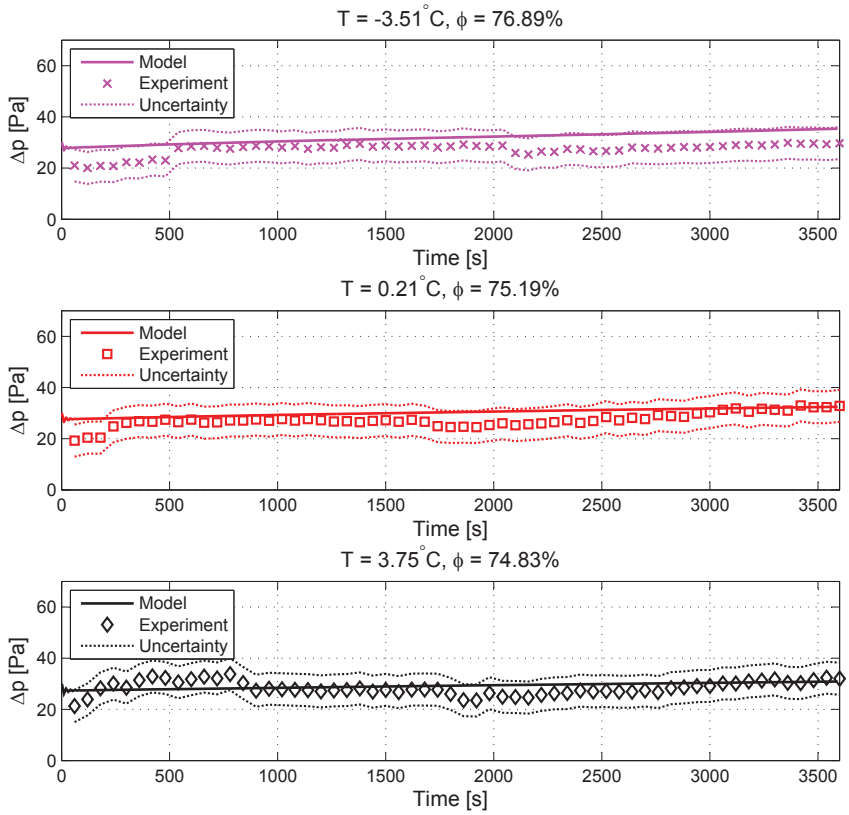

Figure 7.17. Validation of modelled evaporator pressure difference at varied air temperature and constant relative humidity.

The modelled pressure drops at varied air temperature and constant relative humidity are generally consistent with the experimental results and within minor deviations. There is a slight deviation in the beginning of the periods, but the tendencies are consistent throughout the one hour period. The simulated pressure drop at T = -3.51°C is slightly overestimated by the model, but the deviation is within the uncertainty of the experimental result which is acceptable. The simulated pressure drop for T = 3.75°C is within the uncertainty and seems to follow the tendency of the experimental result.

Deviation Between Model and Experimental Data

Since the simulated cooling capacity directly influences the calculation of the defrost initiation point, it is of interest to quantify how much the model deviates from the experimental data. Figure 7.18 shows the absolute deviation in percent as function of time.

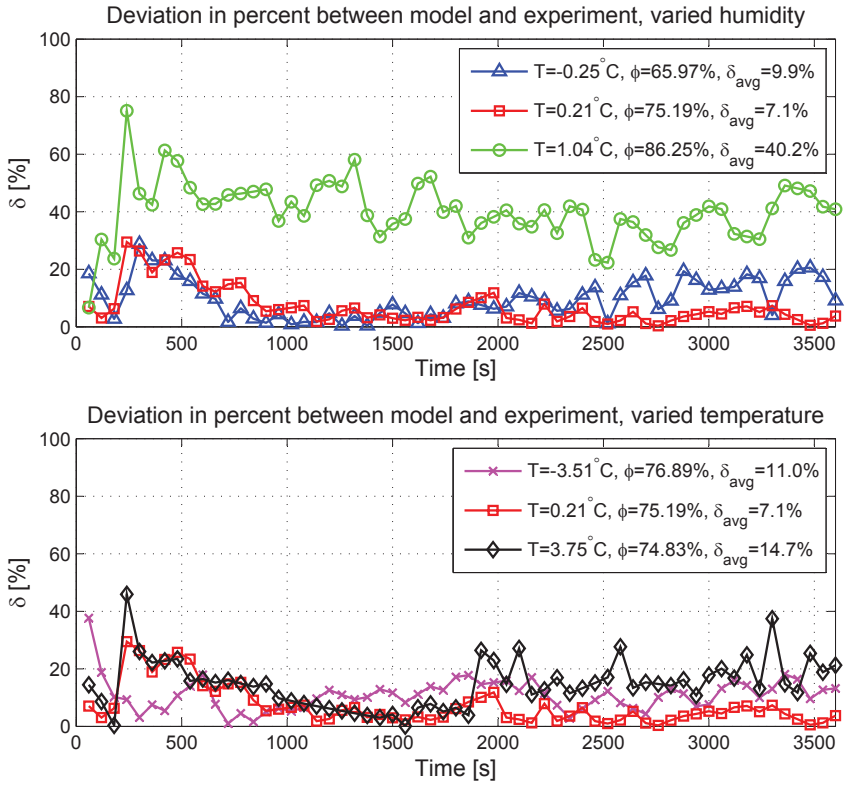

Figure 7.18. Deviation between the model and experiments in percent as function of time. The deviation is calculated as an absolute value, hence the curves do not tell whether the modelled value is higher or lower than for the experiment.

As seen in Figure 7.18, the model generally show a deviation of 20-30% between 300 seconds and 500 seconds, except for experiment 3 (○), that deviates significantly more, and experiment 4 (×) that deviates less. Experiment 1 (△) and experiment 4 (×) resulted in the lowest amount of frost with masses of 1026 g and 1102 g respectively. This yielded average deviations of 9.9% and 11.0%. Experiment 3 (○) and experiment 6 (◇) resulted in the most frost with masses of 1719 g and 1682 g respectively. These cases yielded average deviations of 40.2% and 14.7% respectively. Experiment 2 (□), where a medium amount of frost was measured, was the case with the best consistency. This case had a mass of frost of 1425 g and an average deviation of 7.1%. This could indicate that there is a region stretching from a mass of frost of approximately 1000 g to 1425 g where the model has a relatively consistent match with reality, with average deviations up to 11.0%. The conditions that lead to more frost caused the model to deviate more from reality.

The model is generally consistent with the experimental results for most cases and shows similar trends. Although, it appears that a large amount of frost results in a more significant influence on the cooling capacity during the experiments than the model predicts, which causes the model to overestimate the cooling capacity. For cases with a low amount of frost, the model seems to underestimate the cooling capacity slightly. The deviations will be discussed in Chapter 8.

7.7 Model Simulation Results

Different simulation results are presented in this section in order to visualise and discuss some of the interesting parameters that are not measured, but calculated by the model. The chosen results are for the overall heat transfer coefficient, mass flow rate of air through the evaporator, frost density, and frost thermal conductivity.

The simulated results for the cases with varied relative humidity and constant air temperature are shown in Figure 7.19.

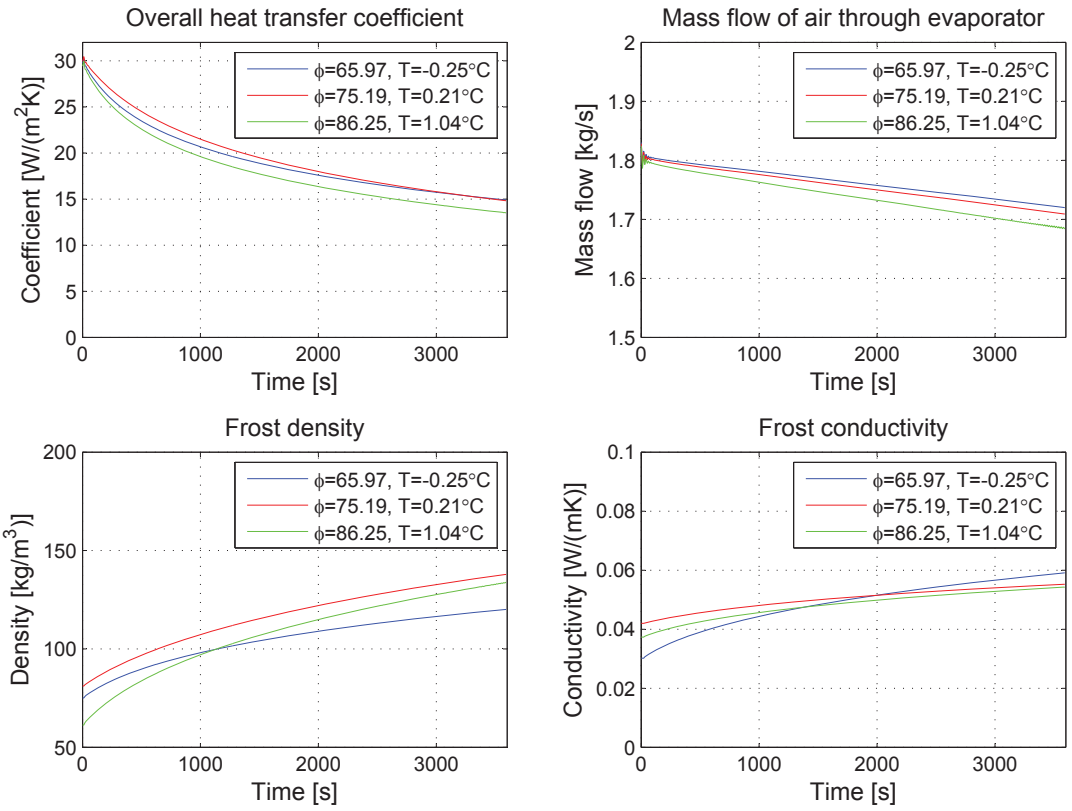

Figure 7.19. Simulated results for the cases with varied relative humidity and constant air temperature.

The overall heat transfer coefficient is dependent on the frost conductivity correlation used for the specific case, hence the slopes have slightly different tendencies. The cases for $\phi = 75.19\%$ and $\phi = 86.25\%$ are both calculated with the frost conductivity from Sturm (1997), which results in similar tendencies. The case with $\phi = 65.97\%$ is calculated with the frost conductivity from Östin & Anderson (1991), which means that the slope is slightly different and has a less decreasing tendency. This difference in correlation causes the red and blue line to overlap.

The mass flow rates of air through the evaporator for the three cases starts at approximately the same value, but with a slight difference due to the small variation in the air temperature. The air temperature variations cause the air densities to vary slightly, which yields a small variation in the mass flow rates of air. The different tendencies for the mass flow rates is a direct consequence of the pressure drop over the evaporator which increases with increased relative humidity in the air flow.

The frost densities are directly related to the surface temperature of the frost layer. The surface temperature of the frost layer is determined from the air flow temperature and the evaporator surface temperature, hence the variation in these temperatures cause the deviations between the tendencies of the frost densities.

The frost conductivities are directly dependent on the frost densities and have different slopes because of the different correlations used.

The simulated results for the cases with varied air temperature and constant relative humidity are shown in Figure 7.20.

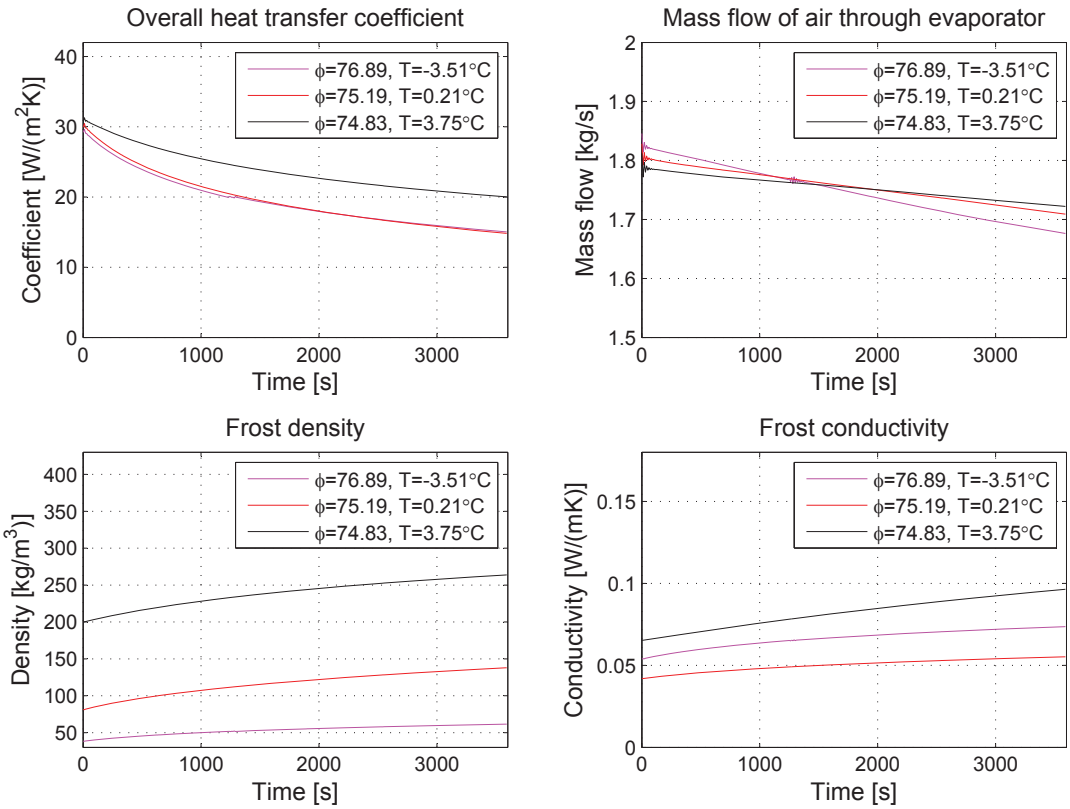

Figure 7.20. Simulated results for the cases with varied air temperature and constant relative humidity

The overall heat transfer coefficients are dependent on the correlations used for the frost conductivity, hence the slopes for the cases of T = 0.21°C and T = 3.75°C have similar tendencies because they are calculated using the frost conductivity correlation from Sturm (1997). The case with T = -3.51°C is calculated using the correlation from Yonko & Sepsy (1967) which results in a slope with a slightly less decreasing tendency.

The mass flow rates for the three cases starts at slightly different values which is primarily due to the temperature difference in the air flows. The reason for the slopes crossing each other is a result of the different pressure drops for the three cases which is dependent on the frost that blocks the air passage.

The values of the frost densities are very different for the three cases which is due to the difference in the frost surface temperatures. The frost surface temperature is dependent on the evaporation temperature which is significantly influenced by the air temperature. A higher air temperature yields a higher frost surface temperature and therefore a higher frost density.

The frost conductivities are determined from the frost densities and the correlation that they are calculated with.

7.8 Comparison of Defrost Strategies

The current DVI defrost strategy is compared to a new strategy which is determined by the frost formation model. This is done by performing a 5-hour experiment at a certain relative humidity and air temperature while logging data with LabVIEW and manually reading the heat production and heat capacity with 3 minute intervals. The measured data is then analysed in order to determine the average air temperature, relative humidity, evaporation temperature and level of superheat. With these values as inputs, the experiment is simulated with the frost formation model in order to calculate the optimum defrost initiation point for the new strategy. The frost conductivity correlation from Östin & Anderson (1991) was used since the best consistency between model and experiment was obtained with this correlation. The 5-hour experiment yielded four full operation cycles which are all compared to the simulation, as shown in the left part of Figure 7.21. The simulated total energy exchanged in the evaporator, the difference between the rated and actual amount, and the calculated time of which the defrost process should be initiated according to the new strategy are shown in the right part of Figure 7.21.

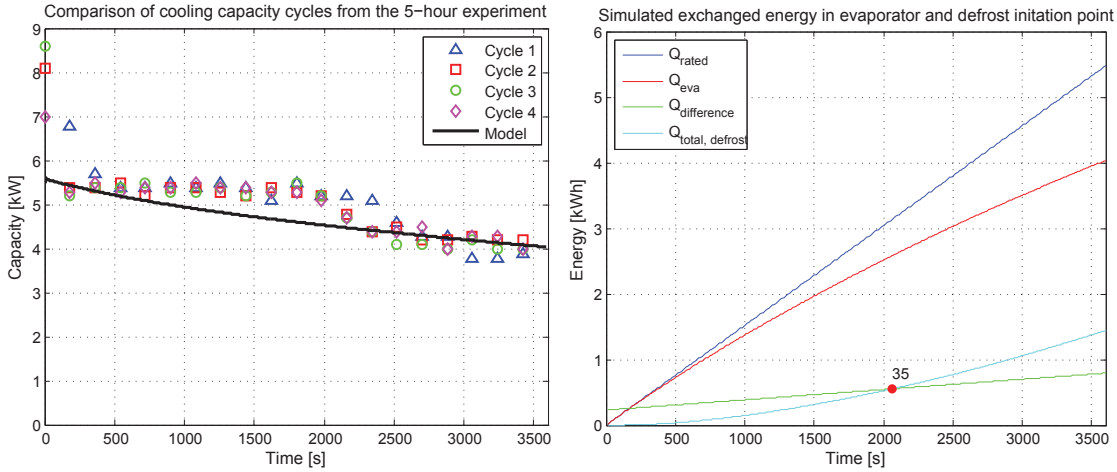

Figure 7.21. Left: The four full operation cycles from the 5-hour experiment and the corresponding model simulation. Right: The simulated exchanged energy in the evaporator and defrost initiation point for the new strategy. $Q_{\text{difference}}$ is the energy that the heat pump is reduced with due to frost.

As seen in Figure 7.21, the simulated cooling capacity show good consistency in the beginning and end of the simulation period. However, there is approximately half an hour in the middle of the simulation where the cooling capacity is underestimated compared to the measured data. An underestimation of the cooling capacity means that the heat pump performs better

than the model predicts, causing the calculation of the defrost initiation point to be earlier than it should be. However, it is of interest to compare the model while using the average values as inputs. Otherwise the simulation could be adjusted on input variables to match the measured data in order to yield another initiation point. By using average input values the defrost initiation point is calculated by the frost formation model to be at 35 minutes.

Once the defrost initiation point is found, the defrost timer of the heat pump control is changed from the original 60 minutes to the calculated 35 minutes, and another 5-hour experiment with the same set points is performed. The set points and measured values for the two 5-hour experiments are given in Table 7.3.

Table 7.3. The experiments and their set points.

$t_{defrost}$ [min]	ϕ_{set} [%]	ϕ_{avg} [%]	T_{set} [°C]	T_{avg} [°C]	ET_{avg} [°C]	SH_{avg} [K]
60	80	77.71	3	2.95	-5.21	5.77
35	80	79.00	3	2.84	-3.69	6.05

As seen in Table 7.3, the relative humidity was approximately 1.3% higher in the second experiment, which might have a minor influence on the results. This also applies for the small difference in air temperatures and level of superheat. The most significant difference between the two experiments is the evaporation temperature (ET), which in average has been 1.52°C higher in the second experiment. This indicates that the lower defrost timer has reduced the influence of frost formation on the heat pump performance.

As previously stated, the energy meter was manually read with 3 minute intervals during the experiment while the electricity meter was logged with LabVIEW. The accumulated amount of energy exchanged in the condenser and the electrical input to the system for the two experiments are shown in Figure 7.22.

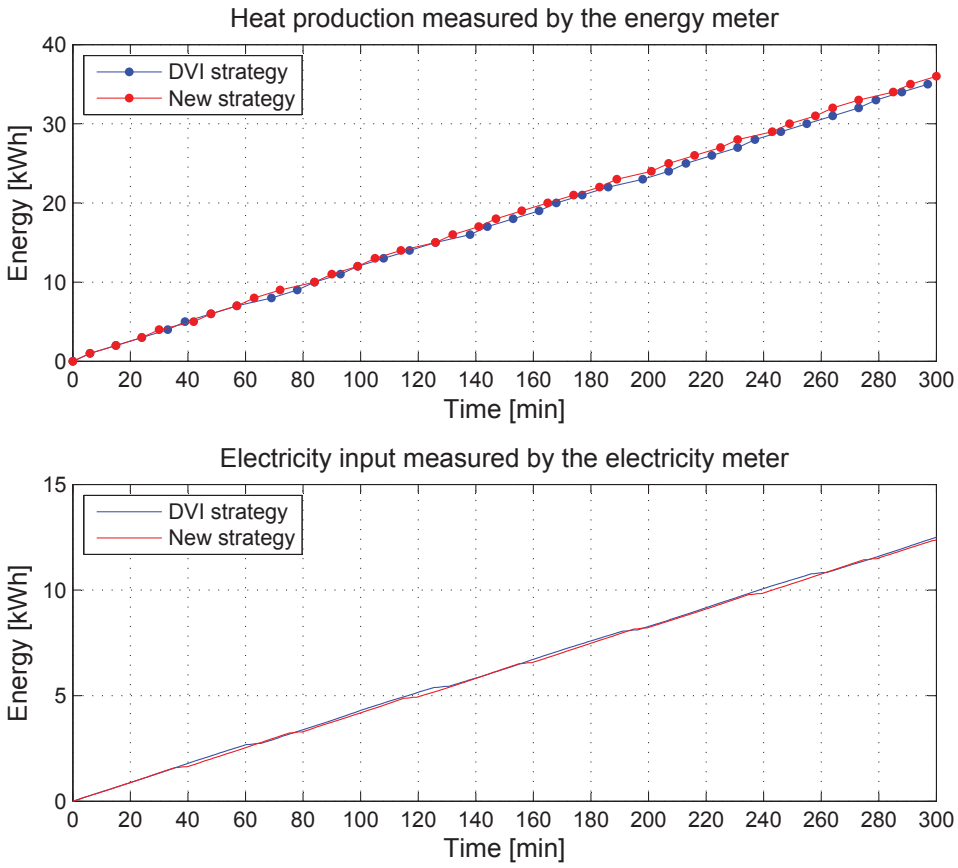

Figure 7.22. The produced heat and electrical input during the 5-hour experiments for defrost intervals of 60 and 35 minutes using the DVI strategy and the new strategy respectively.

As seen in Figure 7.22, the difference in heat production and electrical input to the system for the two strategies are close to insignificant. The DVI strategy produced 35 kWh of heat with an electrical input of 12.500 kWh yielding a total COP of 2.80. The new strategy produced 36 kWh of heat with an electrical input of 12.376 kWh yielding a total COP of 2.91. However, the resolution of the energy meter is 1 kWh resulting in a relatively high uncertainty of the heat production measurement. The first experiment had four defrost cycles during the 5-hour period while the second experiment had seven cycles. The fact that the curves are close to similar indicate that a reduction of the time of each defrost cycle is almost equalized by adding three extra cycles. A defrost timer of 35 minutes will lead to less frost to drain off the evaporator after each defrost cycle than the timer of 60 minutes. It is therefore likely that the time for draining off frost could be reduced to correspond the increased defrost frequency.

The data for the heat production and the electricity consumption is used to calculate the COP throughout the experiments. These are displayed in Figure 7.23.

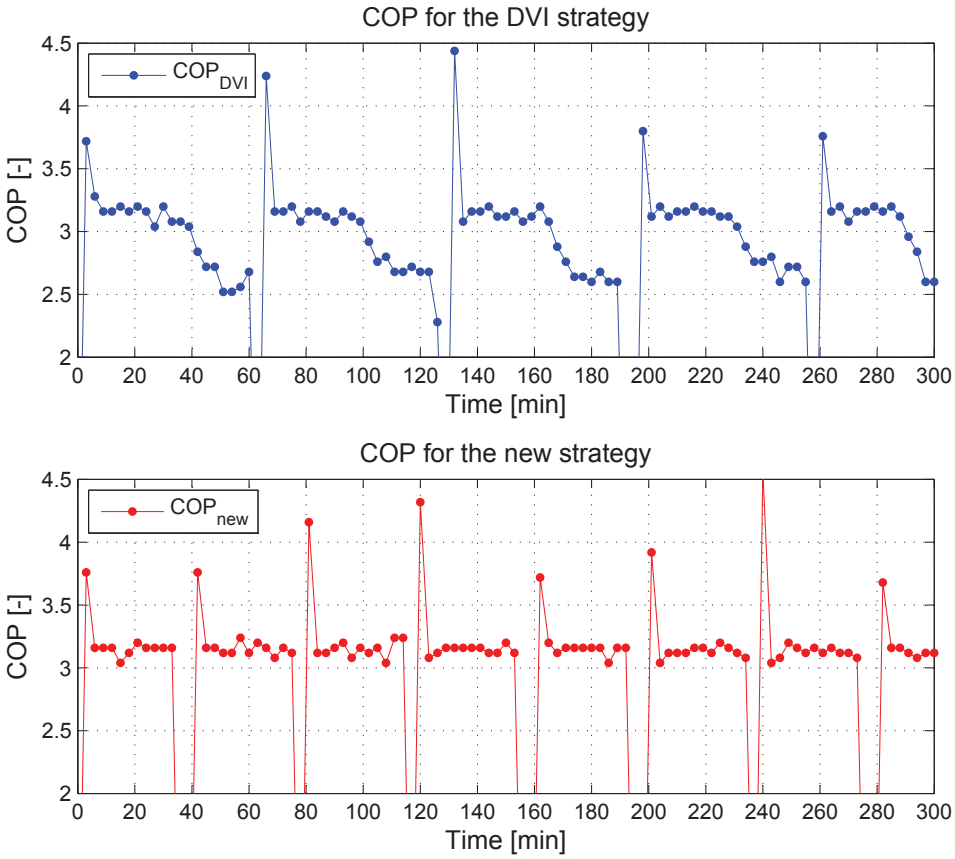

Figure 7.23. The COP during the 5-hour experiments for defrost intervals of 60 and 35 minutes using the DVI strategy and the new strategy respectively.

As seen in Figure 7.23, the DVI strategy resulted in four defrost cycles while the new strategy resulted in seven. It is clear from the DVI strategy that the COP is rather constant for approximately 35-40 minutes after each defrost cycle. After this point, the COP drops significantly for the remaining time until a defrost cycle is performed. With the new strategy, the heat pump performs a defrost cycle where it otherwise would have had a drop in COP. The new strategy therefore leads to more stable operation while increasing the defrost frequency.

The difference between the air temperature and evaporation temperature is the parameter used to determinate the point of defrost for both Bosch Termoteknik and Danfoss. It is therefore interesting to see if it is possible to identify any specific behaviour of this parameter within a nearby range to the calculated defrost point. The difference between the air temperature and evaporation temperature for the two experiments are shown in Figure 7.24.

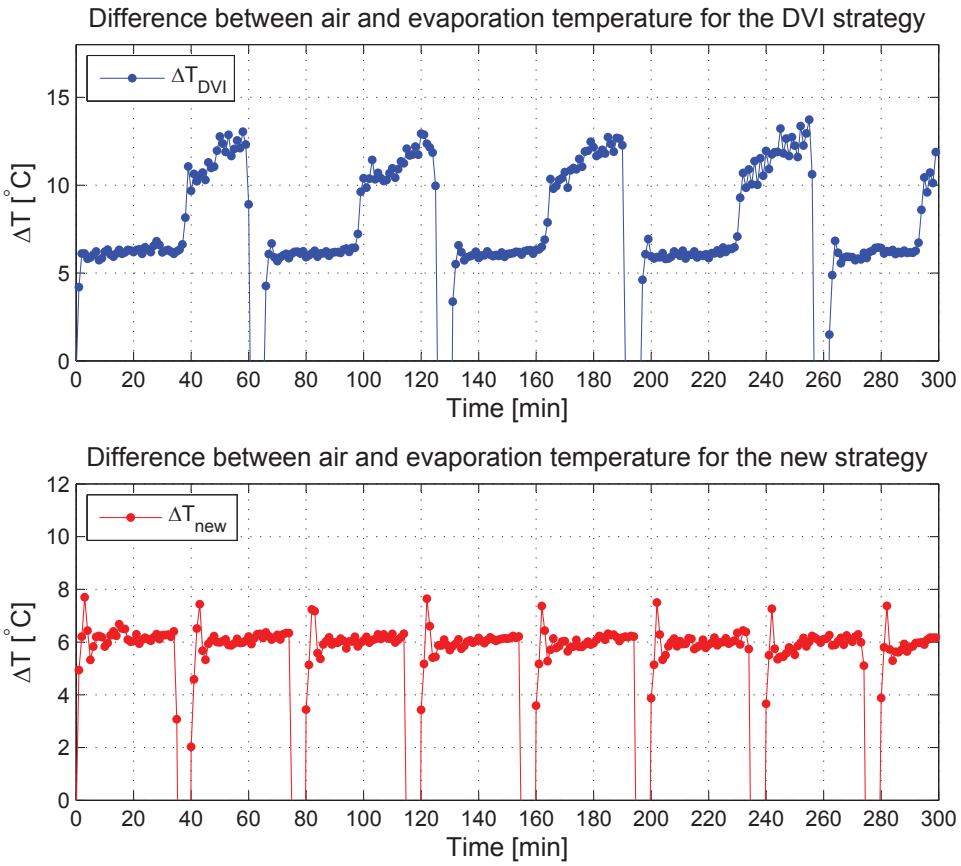

Figure 7.24. The difference between the air temperature and the evaporation temperature during the 5-hour experiment for both strategies.

As expected, the temperature difference show a pattern that corresponds to the COP behaviour. The DVI strategy leads to a significant increase in temperature difference after approximately 35-40 minutes in each cycle. In the new strategy, a defrost cycle is performed just before this increase would have happened. It is therefore plausible that controlling from this temperature difference would yield similar results as using the frost formation model to determine the defrost initiation point. However, it is not possible to tell if the calculated point of defrost would show a similar match at other ambient conditions. This should be investigated further in order to validate the defrost point calculated by the model at other ambient conditions.

7.9 Mass of Frost as Function of Absolute Humidity

A number of additional experiments are performed with the purpose of investigating whether frost formation occurs at higher temperatures than 4°C, which was set as limit according to DVI Energi. Furthermore, it is of interest to investigate the relationship between mass of frost and absolute humidity. Besides the five experiments used to validate the model, six additional one hour experiments are performed at varied ambient conditions, but only the mass of frost as function of ambient conditions is of interest. The resulting absolute humidities are calculated using EES. The average relative humidities, average air temperatures, average absolute humidity and the resulting masses of frost are given for all 11 experiments in Table 7.4.

Table 7.4. The 11 one hour experiments and their average relative humidity, average air temperature, average absolute humidity and mass of frost.

ϕ_{avg} [%]	T_{avg} [°C]	ω_{avg} [g/kg]	m_f [g]
63.63	-0.25	2.117	799
65.97	-0.25	2.434	1026
76.89	-3.51	2.160	1102
75.19	0.21	2.878	1425
74.83	3.75	3.693	1682
77.14	3.82	3.827	1710
74.68	4.73	3.921	1711
86.25	1.04	3.509	1719
81.63	5.09	4.447	2101
81.93	5.87	4.697	2189
77.94	7.76	5.091	2392

The mass of frost as function of absolute humidity for all 11 experiments are shown in Figure 7.25

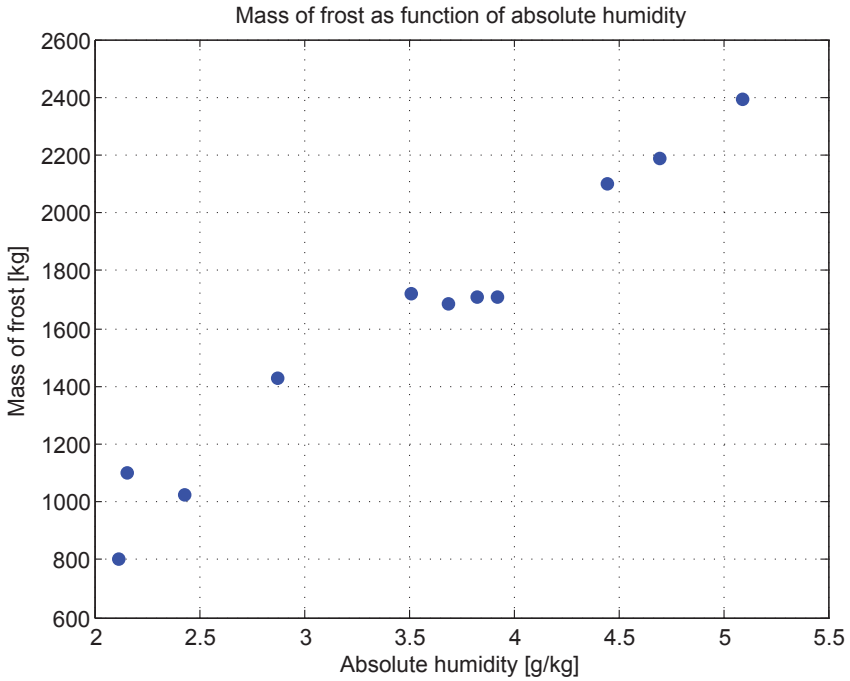

Figure 7.25. The average relative humidities, average air temperatures and the resulting masses of frost for the 11 one hour experiments

The mass of frost as function of absolute humidity seems to have a tendency close to linear in the range investigated. For most cases, a higher absolute humidity in the air flow causes more frost to formate on the evaporator surface. As seen in Table 7.4, frost was obtained on the evaporator surface at temperatures up to 7.76°C which is almost 4°C higher than the expected frost formation limit. Experiments at even higher temperatures could be performed in order to investigate when frost formation no longer occurs.

Chapter 8

Discussion

The purpose of this chapter is to discuss the results and some of the most relevant matters that has caused unexpected or undesired results and conditions. The chapter focuses on discussions related to the experiments, modelling and results, and future tasks and improvements respectively.

8.1 Experimental and Practical Issues

Control of Expansion Valve
During some of the experiments there were problems with the control of the expansion valve. The settings for the controller were adjusted to yield the best control of the superheat reference temperature, but a perfect control was difficult to obtain, especially when the frost formation was severe on the evaporator. It was clear from observations that the controller had difficulties keeping the superheat at the reference point when there was a significant amount of frost on the evaporator surface. This caused the superheat to have large fluctuations around the reference point which directly affects the evaporation temperature. This can be seen Figure 7.6 in Section 7.2. The fluctuations might be a consequence of the way the refrigerant is divided into six vertical tube sections when entering the evaporator. As the heat pump operates it is clearly observed that more frost develops in the bottom part of the evaporator than in the top. The increased thermal resistance causes the bottom sections to exchange less heat than the top sections. Because of this, there is a risk that some of the refrigerant in the bottom sections might not be fully evaporated and still be in its liquid state when leaving the evaporator. The superheat controller uses a temperature sensor located on the tube surface just after the point where the refrigerant streams are rejoined from the six sections. In case some of the refrigerant that passes through this tube is still in liquid state, it could cause a sudden change in temperature and therefore lead to fluctuations when the expansion valve attempts to control this.

The fluctuations were minimised by increasing the reference level of superheat to 6K and reducing the reaction time. However, it was not possible to fully eliminate the fluctuations that occurred in the end of the operation cycle where the frost was most severe. If the new strategy is used, less frost is allowed to develop on the evaporator surface, and it is likely that periods with large fluctuations of superheat will be resolved and allow DVI Energi to lower the superheat reference point.

Influence of Evaporator Position on the Flow Distribution
The evaporator is mounted approximately 30 cm from the end wall and 40 cm over the floor. This is corresponding to how the evaporator typically would be installed at a consumer. However, the evaporator would normally be installed on an outside house wall or similar, with

no walls or ceiling to influence the air flow. Because the climate chamber is relatively small, the air flow will recirculate inside the chamber. It is possible that the position of the evaporator causes a smaller amount of air to recirculate around the sides and bottom of the evaporator compared to around the top of the evaporator, causing an uneven flow distribution. When the evaporator is installed at a customer it is likely that a more natural air flow would result in a more uniform flow distribution. As described in Section 5.2, the flow through the evaporator was assumed to be uniform in the modelling phase. Future improvement of the model could involve accounting for a non-uniform flow distribution.

Measuring Pressure Drop Through Evaporator

The measurement of the pressure drop across the evaporator air side had some large fluctuations in some of the experiments presented in Chapter 7. This is expected to be due to the flow velocity of the air flow that the pressure transmitter is measuring on. The fan that forces the air flow through the evaporator was tested at different fan speeds in order to investigate if this influenced the behaviour of the pressure drop measurement. The pressure drop across the evaporator air side at different fan speeds is shown in Figure 8.1. The experiment was performed with the heat pump turned off and only the fan running.

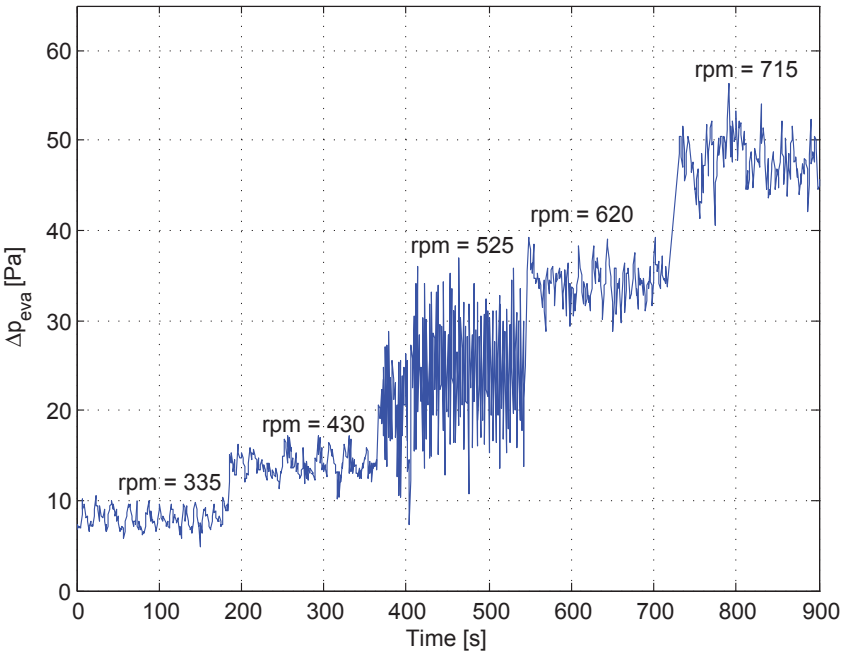

Figure 8.1. Pressure drop through evaporator at varied fan speeds.

As seen in Figure 8.1, there is a more significant fluctuation in the pressure drop measurement at the fan speed of 525 rpm than at any of the other fan speeds. During the experiments throughout the project, the fan speed has been 573 rpm. This implies a large risk of having measured similar fluctuations during the experiments since this fan speed is very close to where the undesired fluctuations occurs. This phenomenon is believed to occur either because of some turbulent tendencies in the air flow or due to an unknown issue regarding the rotational frequency. At higher fan speeds, the measurement behaves as expected which could indicate that whatever caused the fluctuations only do so in a certain range of flow velocity. The standard fan speed used by DVI Energi is 573 rpm, hence this speed is used in

all experiments.

Uncertainties of Acquired Data
In general the quality of the acquired data is considered reliable. The LabVIEW program was designed to acquired data with a rate of 20 samples per second and a sample length of 20 samples, yielding one data point each second that was the average value of the 20 samples. Furthermore the data was analysed and corrected for misreadings and then averaged over 60 seconds yielding one data point for each minute during the experiments. The equipment with the highest uncertainties were the air temperature sensor, the evaporator pressure difference sensor, the energy meter, and the mass of frost measurement.

The air temperature sensor used is a PTC sensor of type KTY82/121 which has a relatively large uncertainty that varies with the temperature. Between -10°C and 10°C, the average uncertainty is 1.91°C. All temperature sensors were calibrated to 0°C with ice water in order to minimise uncertainties.

The pressure difference sensor had large fluctuations in some flow velocities as previously mentioned. Furthermore, it had an absolute error of 6.25 Pa, which is a relatively large uncertainty when measuring pressure differences in the region of 30 Pa. The pressure sensor was calibrated to zero after it was mounted on the evaporator surface. The pressure tubes were mounted at each end of the same evaporator channel normal to the flow direction, which ideally should give a measurement of only the static pressure. However, at the inlet side the air is drawn in from several directions and most likely not perfectly aligned with the channel direction when measured. Hence there is a risk of measuring some of the dynamic pressure at the air inlet side.

The heating capacity and total heat production was manually read from the energy meter. The total heat production was read from a display of the total accumulated megawatt hours measured, with a resolution of three digits of precision. It was therefore only possible to read the heat production as an integer number of kilowatt hours, which naturally implies a relatively large uncertainty. During one hour of experiments, the energy meter counted approximately 7 kWh, yielding a maximum uncertainty of 1/7 kWh or 14.3%. However, this reading was only used for further analysis in the 5-hour experiments where the energy meter counted approximately 35 kWh, yielding an uncertainty of 1/35 kWh or 2.9%.

The approach of using a scale to measure the amount of frost on the evaporator gives reason to some uncertainty. There are two major reasons for this which are water retention and vaporization. After defrost cycles it was observed that not all water drained off the evaporator surface. Some of the droplets were retained on the fin surface and quickly froze when the heat pump returned to normal operation. It is very likely that additional water was retained in the drain tray beneath the evaporator surface, but this was not visually observed. Furthermore it was observed that some of the melted frost was vaporized during defrost cycles and was therefore not accounted for when measuring the mass of frost. The is consistent with the measurements, where the relative humidity increased during a defrost cycle as seen in Figure 7.4 in Section 7.2.

8.2 Model Development and Results

Reasons for Deviations Between Model Simulations and Experiments
In Section 7.6 regarding model validation, it was observed that the model generally deviates from the measured data in the beginning of the experiments. The model does not show as steep gradients as seen in the measured data. The steep gradients are a result of the expansion valve controller that attempts to match the reference point. In the end of a defrost cycle, when the 4-way valve is reversing to normal operation, the compressor is turned off and the expansion valve controller is turned on. When returning to normal operation, the expansion valve is fully open when the compressor starts the normal operation. The level of superheat quickly drops below the reference point and the expansion valve responds by closing. This pattern continues for some time, often around 5-7 minutes, until the controller finds the opening degree that makes the level of superheat match the reference point. This behaviour was previously shown in Figure 3.5. Because the energy meter is only read once every minute this fluctuation is not seen in neither the capacity or COP data. If the energy meter was read more often the capacity and COP would reflect this fluctuating pattern in the beginning of the experiments. As the model is designed with a constant level of superheat it cannot account for these large fluctuations which explains the general deviation in these periods.

The model validation given in Section 7.6 also revealed that the average deviation between model and experimental data was 11% or less when the ambient conditions resulted in a mass of frost up to 1425g. These average values include the beginning of the operation process where a large part of the deviation is caused by the fluctuating expansion valve.

Distribution and Formation of Frost
When developing the model it was assumed that a certain amount of frost would distribute equally over a given area. This means that the model predicts a frost layer of uniform thickness on all surfaces after the point x_f, regardless if the surface is a circular tube or a vertical flat fin. This assumption was made in order to simplify the modelling process, and it was expected to behave differently in reality. Throughout the experiments, the frost formation was observed to be most significant in the bottom of the evaporator. This is illustrated in Figure 8.2.

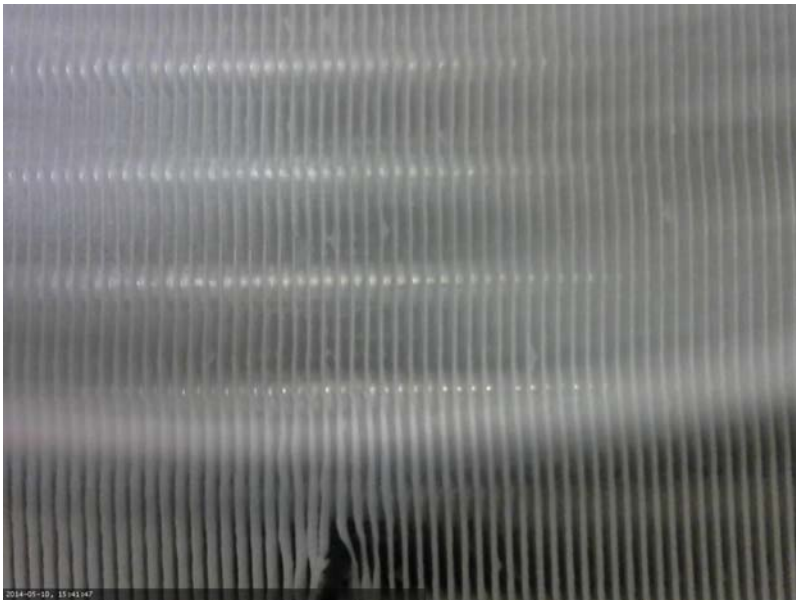

Figure 8.2. Image of the distribution of frost seen from the air outlet side. The frost layer is significantly thicker in the lower part of the image compared to other positions. The blurred white shadow is caused by frost on the fan blades. The image is taken after 54 minutes at $\phi = 88.48\%$ and $T = 0.65°C$.

It is clear from Figure 8.2 that the model assumption of uniform frost thickness does not represent the reality, and that model could be improved by distributing the frost in a way that is more consistent with reality. It is most likely a combination of several parameters that causes this non-uniform frost thickness. First of all there is the influence of the uneven flow distribution as previously described. The lower volumetric flow rate in the bottom section of the evaporator causes the air flow velocity to be lower which leads to a colder air flow. Furthermore it has been observed, that after a defrost cycle, water droplets drain down the fins where some of them become stationary and quickly refreezes once the heat pump returns to normal operation. These droplets are believed to initiate further frost formation since frost crystallisation occurs directly without nucleation on them. Additionally there are flow phenomena such as turbulence, shear stress, and particle size that also influence whether or not frost can deposit on a surface. All these parameters make it difficult to determine when and where on the evaporator surface frost begins to develop.

Frost Thermal Conductivity Correlations

The frost formation model developed in this project can use different correlations for the frost thermal conductivity. All the correlations describe the thermal conductivity as function of the frost density. When the model was compared to the experimental data, the results were calculated with the correlation that had the best match with the experimental data. Since the experiments were conducted at different ambient conditions, the frost structure and properties are very likely to relate to these conditions. It is therefore possible that one kind of frost will match with one correlation, while another kind of frost will have a better fit with another correlation. However, it has not been possible from the experiments conducted in this project to determine a clear pattern for what correlation is best fitting for a specific case. As stated in Section 1.3, it is difficult to select an accurate correlation for frost thermal conductivity because the frost formation process is very dependent on ambient

conditions. The best way to ensure that the frost thermal conductivity is consistent with the frost formation that occurs is to develop a specific correlation for a specific case. This is however impractical, but could be done using Fourier's law of heat conduction.

Frost Density Correlation

Contrary to the correlation for frost thermal conductivity, only one correlation for the frost density is used in the model. This correlation is developed by Hayashi et al. (1977) and is widely used and recognised in studies similar to this one. As shown in Figure 5.12 in Section 5.9, the frost density is a function of the frost surface temperature, which is determined by the evaporation temperature and the air temperature. Therefore, the different air temperatures in the experiments will cause the density of the frost that develops to be different. It was shown in Figure 7.20 in Section 7.7, that a temperature change from -3.51°C to 3.75°C increases the density with a factor of more than four. As a consequence of this, a frost mass of 1.682 kg does not necessarily lead to a thicker frost thickness than a mass of 1.102 kg. An example of this was seen in Figure 7.15 in Section 7.6, where the model predicts the pressure drop of experiment 3 (○) to only increase slightly compared to experiment 1 (△). However, a significant increase in pressure drop was obtained through the experiment, which indicates a thicker layer of frost. This deviation is likely to be caused by the assumption that the frost density and frost thermal conductivity is constant through the frost layer. As the frost is continuously developed in layers this is likely to cause the density and thermal conductivity to vary throughout the layer.

Neglecting Mass Diffusion

Mass diffusion in the porous frost layer was neglected in the frost formation model for simplicity, although mass diffusion will occur in reality due to concentration gradients in the frost layer. Including mass diffusion in the model would possibly increase the accuracy of the model. Mass diffusion calculations will depend on local water vapour densities in the frost layer and will affect the calculation procedure of the frost layer thickness and frost conductivity. Including mass diffusion would probably yield less frost that contributes to increasing the frost thickness and instead contribute to densification of the frost layer.

Neglection of Fin Louvers

The fins in the evaporator were modelled as flat plate fins without any louvers. As shown in Figure 3.2 in Section 3.2, the evaporator fins are designed with one-sided louvers, which will influence the cooling capacity, frost formation and several other parameters. The louvers were neglected because it was not possible to get detailed information on the louver geometry from the manufacturer of the evaporator, and it was not possible to determine this in other ways. Neglecting the louvers yielded a simplification of the modelling process, but would most likely have improved the accuracy of the model.

Influence of Realistic Operation Pattern on The Defrost Strategies

When the defrost strategies were compared in Section 7.8, the 5-hour duration of the experiments was primarily chosen in order to reduce the uncertainty of the energy meter readings. In reality a heat pump in a family house will rarely operate this long without stopping. The operation pattern will usually result in periods with either little or no demand of heat. It is therefore interesting to consider how the two defrost strategies would perform with different operation patterns, where the frost may or may not naturally melt in between the operation periods, depending on the ambient conditions.

8.3 Future Tasks and Improvements

Approaches to Determine the Defrost Interval
The frost formation model has shown that it is possible to model the performance of an ASHP under increasingly frosted conditions. The model can be used to determine the optimal defrost interval at a specific ambient temperature and relative humidity. By changing the heat exchanger geometry and compressor characteristics, the model can relatively easy be adjusted to a wide range of different heat pump and evaporator configurations. However, the model heavily depends on empirical factors and correlations which makes it more accurate in some conditions than others. The model is also sensitive to the input values of ambient temperature, relative humidity, evaporation and condensation temperature, and level of superheat, hence it is essential to compare the model to experiments.

In the 5-hour experiments of the defrost strategies, the model successfully calculated the point of where the heat pump experienced a significant drop in COP and capacity. Other heat pump manufacturers, like Danfoss and Bosch Termoteknik, continuously monitor temperature differences, such as the difference between the ambient temperature and the evaporation temperature, in order to determine this point. This approach seems to be a more practical way of improving the defrost issue than using a model to predict the optimal defrost point.

Further Improvement of the Heat Pump System
It was shown in Section 7.8, that changing the defrost interval from 60 minutes to 35 minutes did not increase neither the heat production or the COP noticeable. One of the reasons for this is that the actual defrost process was not changed accordingly. It is reasonable to believe that the termination criteria could be adjusted to match the reduced defrost interval, and that the wait timers, where the heat pump is reversed, could be reduced to account for less frost to drain off the surface. If DVI Energi choose to reduce the defrost interval in the future, the defrost cycle process should be changed accordingly.

Additionally it could be very interesting to research other parameters that could reduce the development of frost. In the future it might be a solution to treat heat exchanger surfaces using nanotechnology in order to prevent frost particles to stick to the surface.

Chapter 9

Conclusion

The objective of this project was to develop a reversed cycle defrost control strategy for an ASHP that could improve the performance of the DVI LV9 Combi heat pump compared to its current strategy. The approach was to develop a dynamic model of the frost formation process on the evaporator surface and the heat pump performance reduction and thereby determine the optimal defrost interval at a set of ambient conditions. The current defrost strategy would be compared to the new strategy in an experimental study.

The model of the frost formation process on the evaporator surface was developed as a dynamic model where the heat pump performance reduction was modelled as a consequence of an increasing frost formation. The frost formation process was modelled using empirical correlations for the properties of frost. The impact of the frost formation on the flow conditions was modelled to account for the blocking effect of the increasing frost layer development on the evaporator surface.

Experimental studies were performed in a climate chamber in order to investigate the influence of ambient conditions on the frost formation process and to validate the frost formation model. The experiments consisted of a single operation and defrost cycle and were conducted in two parts. In the first part, the relative humidity set point was varied between 65% and 85% while the air temperature set point was kept constant at 0°C. The second part was performed with varied air temperature set point between -4°C and 4°C while the relative humidity set point was kept constant at 75%. As expected, higher air temperatures and relative humidities resulted in more frost to develop on the evaporator surface and a more significant performance reduction was obtained. When the relative humidity was varied, the cooling capacity of the heat pump was initially relatively similar for the three experiments, but deviated from each other as frost was developed with time. When the air temperature was varied, the cooling capacity was initially more influenced by the air temperature, as the performance curves clearly differed from each other in the first half of the operation cycles. During all experiments, the difference between the air temperature and evaporation temperature increased during the operation cycle, often with a sudden significant increase.

The frost formation model was used to simulate an operation cycle at the conditions that were measured during the experiments. This was done in order to validate the model against the experiments at varied ambient conditions. In general, the model deviated from the experimental data in the beginning of the operation cycles. A significant reason for this was the controller of the electronic expansion valve that fluctuated around its superheat reference point. The model generally underestimated the cooling capacity at conditions that resulted in a low amount of frost and overestimated at conditions that yielded a high amount of frost.

At a medium level of frost, the model was consistent with the experimental results with an average deviation of 7.1%. The average deviations between the experimental data and model simulations are given in Table 9.1.

Table 9.1. The one hour experiments, used to validate the model against the experiments, and their average relative humidity, average air temperature, mass of frost, and deviation between model and experimental data.

ϕ_{avg} [%]	T_{avg} [°C]	ω_{avg} [g/kg]	m_f [g]	δ_{avg} [%]
65.97	-0.25	2.434	1026	9.9
75.19	0.21	2.878	1425	7.1
86.25	1.04	3.509	1719	40.2
76.86	-3.51	2.159	1102	11.0
74.83	3.75	3.693	1682	14.7

The model simulations were performed with the frost thermal conductivity correlation that resulted in the best match. The choice of correlation had a significant influence on the overall heat transfer coefficient and thereby the cooling capacity of the evaporator. It was observed that the conditions under which the frost was developed had a significant impact on what correlation for frost conductivity that yielded the best consistency, but no clear pattern for this tendency was found.

The model was used to calculate a new defrost interval which was compared to the current defrost strategy in two 5-hour experiments at a relative humidity set point of 80% and an air temperature set point of 3°C. The current strategy was performed with a defrost interval of 60 minutes. A new defrost interval was determined by the frost formation model which yielded an interval of 35 minutes in the new strategy. The interval of 35 minutes caused the heat pump to initiate a defrost cycle just before it would otherwise have had a significant drop in performance. Defrosting after 35 minutes therefore resulted in a more stable operation at the cost of more frequent defrosting cycles. The difference in electrical input and accumulated heat exchanged in the condenser during the 5-hour experiments were almost insignificant, indicating that the cost of performing additional defrost cycles was equalized by the more stable performance. However, if the defrosting process had been changed according to the reduced interval time it would have been beneficial for the new strategy. It is likely that a more stable performance would allow DVI Energi to reduce the superheat reference point and increase the performance.

The developed frost formation model successfully identified a defrost initiation point that resulted in more stable heat pump performance. However, the model is very sensitive to the input variables and properties for frost, which makes it more practical to determine the defrost point from measuring the difference between evaporation temperature and ambient temperature. With improvements to the inlet air flow distribution and frost deposition pattern the model could serve as an analysis tool in the refrigeration industry.

Bibliography

Barry N. Taylor and Chris E. Kuyatt, **1994**. Barry N. Taylor and Chris E. Kuyatt. *Guidelines for Evaluating and Expressing the Uncertainty of NIST Measurement Results*, 1994. http://physics.nist.gov/Pubs/guidelines/TN1297/tn1297s.pdf, viewed: 08.04.2014.

Byun, Jeon, Jung, and Lee, **2006**. Ju-Suk Byun, Chang-Duk Jeon, Ji-Hoon Jung, and Jinho Lee. *The application of photo-coupler for frost detecting in an air-source heat pump*. International Journal of Refrigeration, 2006. http://www.sciencedirect.com/science/article/pii/S014070070500126X, viewed: 08.02.2014.

Byun, Lee, and Jeon, **2007**. Ju-Suk Byun, Jinho Lee, and Chang-Duk Jeon. *Frost retardation of an air-source heat pump by the hot gas bypass method*. International Journal of Refrigeration, 2007. http://www.sciencedirect.com/science/article/pii/S0140700707000849, viewed: 06.02.2014.

Cengel and Boles, **2004**. Yunus A. Cengel and Michael A. Boles. *Thermodynamics - An Enginnering Approach*. McGraw-Hill, 5th edition, 2004. ISBN: 978-0-58-209193-1.

Cengel and Ghajar, **2011**. Yunus A. Cengel and Afshin J. Ghajar. *Heat and Mass Transfer*. McGraw-Hill, 4. edition, 2011. ISBN: 0073398128.

Cengel, Turner, and Cimbala, **2008**. Yunus A. Cengel, Robert H. Turner, and John M. Cimbala. *Fundamentals of Thermal-Fluid Sciences*. McGraw-Hill, 3rd edition, 2008. ISBN: 978-007-126631-4.

Christian Hedegaard, **2014**. Christian Hedegaard. *Correspondance with Christian Hedegaard, Danfoss*, 2014. Date: 28.04.2014.

Cui, Li, Liu, and Zhao, **2010**. J. Cui, W.Z. Li, Y. Liu, and Y.S. Zhao. *A new model for predicting performance of fin-and-tube heat exchanger under frost condition*. International Journal of Heat and Fluid Flow, 2010. http://ac.els-cdn.com/S0142727X10001827/1-s2.0-S0142727X10001827-main.pdf?_tid=249b13b6-92f9-11e3-b1b9-00000aacb360&acdnat=1392108631_0cacce5ce0c4396a65a2dcf8fde5bae7, viewed: 11.02.2014.

Danish Meteorological Institute, **2013**. Danish Meteorological Institute. *Danish Meteorological Institute - Weather Archive*, 2013. http://www.dmi.dk/vejr/arkiver/vejrarkiv/, viewed: 17.02.2014.

Don, Deng, Jiang, Xia, and Yao, **2011**. Jiankai Don, Shiming Deng, Yiqiang Jiang, Liang Xia, and Yang Yao. *An experimental study on defrosting heat supplies and energy consumptions during a reverse cycle defrost operation for an air source heat pump*. Journal of Applied Thermal Engineering, 2011.

http://www.sciencedirect.com/science/article/pii/S1359431111006806, viewed: 06.02.2014.

DONG Energy, Energinet.dk and Dansk Energi, **2013**. DONG Energy, Energinet.dk and Dansk Energi. *Varmepumper i Danmark - Udviklingsforløb for omstilling af oliefyr frem mod 2035*, Dansk Energi, 2013. http://www.danskenergi.dk/~/media/DEMJE/Analyser/Analyse06-Varmepumper_i_Danmark-Udviklingsforloeb_for_omstilling_af_oliefyr_frem_mod.ashx, viewed: 06.02.2014.

DVI Energi, **2014**. DVI Energi. *DVI Energi*, 2014. www.jordvarme.dk, viewed: 28.05.2014.

Hayashi, Aoki, Adachi, and Hori, **1977**. Y. Hayashi, A. Aoki, S. Adachi, and K. Hori. *Study of frost properties correlating with frost formation types*. ASME, 1977. viewed: 17.03.2014.

Henrik Hansen, **2014**. Henrik Hansen. *Correspondance with Henrik Hansen, Bosch Termoteknik*, 2014. Date: 10.02.2014.

John Roe, 3D Air Sales Ltd, **2000**. John Roe, 3D Air Sales Ltd. *R407C - The Engineers Guide*, 2000. http://www.3dair.co.uk/download-files/r407c-guide.pdf, viewed: 08.04.2014.

Kandula, **2010**. M. Kandula. *On the Effective Thermal Conductivity of Frost Considering Mass Diffusion and Eddy convection*, NASA, 2010. http://ntrs.nasa.gov/archive/nasa/casi.ntrs.nasa.gov/20110001592.pdf, viewed: 17.03.2013.

Kays and London, **1984**. W.M. Kays and A.L. London. *Compact Heat Exchangers*. Krieger Publishing Company, 3rd edition, 1984. ISBN: 1-57524-060-2.

Kwak and Bai, **2009**. Kyungmin Kwak and Cheolho Bai. *A study on the performance enhancement of the heat pump using electric heater under the frosting condition: Heat pump under frosting condition*. Journal of Applied Thermal Engineering, 2009. http://www.sciencedirect.com/science/article/pii/S1359431109003147, viewed: 06.02.2014.

Liang, Zhang, Li, and Chen, **2010**. Cai-Hua Liang, Xiao-Song Zhang, Xiu-Wei Li, and Zhen-Qian Chen. *Control strategy and experimental study on a novel defrosting method for air-source heat pump*. Journal of Applied Thermal Engineering, 2010. http://www.sciencedirect.com/science/article/pii/S1359431110000098, viewed: 07.02.2014.

Moallem, Padhmanabhan, Cremaschi, and Fisher, **2010**. Ehsan Moallem, Sankar Padhmanabhan, Lorenzo Cremaschi, and Daniel E. Fisher. *Experimental study of onset and growth of frost on outdoor coils of air-soruce heat pump systems*, School of Mechanical & Aerospace Engineering, Oklahoma State University, 2010. http://www.hvac.okstate.edu/Papers/Experimental%20study%20of%20onset%20and%20growth%20of%20frost%20on%20outdoor%20coils%20of%20air-source%20heat%20pumps%20(2010).pdf, viewed: 06.02.2014.

Myers, **1998**. Glen E. Myers. *Analytical Methods in Conduction Heat Transfer*. AMCHT Publications, 2. edition, 1998. ISBN: 0966606507.

Padhmanabhan, Cremaschi, Fisher, and Knight, **2008**. Sankar Padhmanabhan, Lorenzo Cremaschi, Daniel E. Fisher, and John Knight. *Comparison of Frost and Defrost Performance Between Microchannel Coil and Fin-and-Tube Coil for Heat Pump Systems*, Oklahoma State University, 2008. http://docs.lib.purdue.edu/iracc/869, viewed: 06.02.2014.

Pallesen, **2014**. Henning Pallesen. *Correspondance with Henning Pallesen, DVI Energi*, 2014. Date: 17.02.2014.

Prölss and Schmitz, **2006**. Katrin Prölss and Gerhard Schmitz. *Modeling of Frost Growth on Heat Exchanger Surfaces*, Hamburg University of Technology, 2006. https://modelica.org/events/modelica2006/Proceedings/sessions/Session5b3.pdf, viewed: 25.04.2014.

Qu, Xia, Deng, and Jiang, **2011**. Minglu Qu, Liang Xia, Shiming Deng, and Yiqiang Jiang. *An experimental investigation on reverse-cycle defrosting performance for an air source heat pump using an electronic expansion valve*. Journal of Applied Energy, 2011. http://www.sciencedirect.com/science/article/pii/S0306261911007628, viewed: 06.02.2014.

Rohsenow, Hartnett, and Cho, **1998**. Warren M. Rohsenow, James P. Hartnett, and Young I. Cho. *Handbook of Heat Transfer*. McGraw-Hill, 3rd edition, 1998. ISBN: 0-07-053555-8.

Sahin, **2000**. Ahmet Z. Sahin. *Effective thermal conductivity of frost during the crystal growth period*. International Journal of Heat and Mass Transfer, 2000. http://ac.els-cdn.com/S0017931099001623/1-s2.0-S0017931099001623-main.pdf?_tid=a988c728-cdfd-11e3-bb97-00000aacb362&acdnat1398597690_35c03bef885b02d63e6f2e0f7e579592, viewed: 25.04.2014.

Theerakulpinut, **1995**. S. Theerakulpinut. *Application of Modified Bessel Functions in Extended Surface Heat Transfer Problems*. Engineering Journal, 1995. http://www.tci-thaijo.org/index.php/kkuenj/article/viewFile/8121/8049, viewed: 31.03.2014.

Thermal Transfer Technology Limited, **2014**. Thermal Transfer Technology Limited. *Thermal Transfer Technology Limited*, 2014. Date: 17.02.2014.

Thulukkanam, **2013**. Kuppan Thulukkanam. *Heat Exchanger Design Handbook*. CRC Press, 2nd edition, 2013. ISBN: 978-143-984212-6.

Wang and Liu, **2003**. S.W. Wang and Z.Y. Liu. *A new method for preventing HP from frosting*. Renewable Energy, 2003. http://www.sciencedirect.com/science/article/pii/S0960148103002751, viewed: 08.02.2014.

Wang, Xiao, Guo, Lu, and Feng, **2011**. W. Wang, J. Xiao, Q.C. Guo, W.P. Lu, and Y.C. Feng. *Field test investigation of the characteristics for the air source heat pump under two typical mal-defrost phenomena*. Journal of Applied Energy, 2011. http://www.sciencedirect.com/science/article/pii/S0306261911003424, viewed: 06.02.2014.

Xu, Han, Chen, Li, Wang, Li, and Pan, **2012**. Bo Xu, Qing Han, Jiangping Chen, Feng Li, Nianjie Wang, Dong Li, and Xiaoyong Pan. *Experimental investigation of frost and defrost performance of microchannel heat exchangers for heat pump systems*. Journal of Applied Energy, 2012. http://www.sciencedirect.com/science/article/pii/S0306261912006678, viewed: 06.02.2014.

Yan, Li, and Tsay, **2005**. Wei-Mon Yan, Hung-Yi Li, and Yeong-Ley Tsay. *Thermofluid characteristics of frosted finned-tube heat exchangers*. International Journal of Heat and Mass Transfer, 2005. http://www.sciencedirect.com/science/article/pii/S0017931005001778, viewed: 10.02.2014.

Yang and Lee, **2004**. Dong-Keun Yang and Kwan-Soo Lee. *Dimensionless correlations of frost properties on a cold plate*. International Journal of Refrigeration, 2004. http://ac.els-cdn.com/S014070070300118X/1-s2.0-S014070070300118X-main.pdf?_tid=a147e8d8-cc44-11e3-8a04-00000aab0f6c&acdnat=1398408268_51a2071984f0780510de7c0606dbe22b, viewed: 25.04.2014.

Ziehl-Abegg, **2013**. Ziehl-Abegg. *Fan Measurement for Pressure Drop*, 2013. http://www.ziehl-abegg.com/ww/fans-download.html, viewed: 26.03.2014, PDF attached.

Appendix A

Properties of Atmospheric Air

Atmospheric air is a gas and liquid mixture that consists of dry air and water vapour. Different properties for atmospheric air are stated in this section and based on Cengel and Boles (2004).

Humidity Ratio and Relative Humidity
The composition of atmospheric air can be expressed as the humidity ratio by mass. This is defined as the ratio of the actual mass of water in the atmospheric air to the mass of the dry air which is given in Equation (A.1).

$$\omega = \frac{m_\mathrm{v}}{m_\mathrm{a}} \qquad \left[\mathrm{kg_v/kg_{d.a}}\right] \quad \text{(A.1)}$$

Where:
ω is humidity ratio $[\mathrm{kg_v/kg_a}]$
m_v is the mass of water vapour [kg]
m_a is the mass of dry air [kg]

The humidity ratio can also be expressed based on partial pressures as given in Equation A.2.

$$\omega = \frac{p_\mathrm{v} V/R_\mathrm{v} T}{p_\mathrm{a} V/R_\mathrm{a} T} = \frac{p_\mathrm{v}/R_\mathrm{v}}{p_\mathrm{a}/R_\mathrm{a}} = 0.622\frac{p_\mathrm{v}}{p_\mathrm{a}} \qquad \left[\mathrm{kg_v/kg_{d.a}}\right] \quad \text{(A.2)}$$

Where:
p_v is the partial pressure of water vapour [Pa]
p_a is the partial pressure of dry air [Pa]
R_v is the gas constant of water vapour [kJ/kg K]
R_a is the gas constant of dry air [kJ/kg K]
V is volume $[\mathrm{m^3}]$
T is temperature [K]

Equation (A.2) can be rewritten to express the pressures in terms of total and partial pressures which is given in Equation (A.3).

$$\omega = \frac{0.622 p_\mathrm{v}}{p - p_\mathrm{v}} \qquad \left[\mathrm{kg_v/kg_{d.a}}\right] \quad \text{(A.3)}$$

Where:
p is total pressure [Pa]

The relative humidity of air is given as the ratio of the partial pressure of water vapour to the saturated pressure of water vapour at a given temperature. This is given in Equation (A.4).

$$\phi = \frac{p_{\mathrm{v}}}{p_g} \qquad [\text{-}] \quad \text{(A.4)}$$

Where:
ϕ is the relative humidity [-]
p_{v} is the partial pressure of water vapour [Pa]
p_g is the saturated pressure of water vapour at a given temperature [Pa]

The expressions for humidity ratio and relative humidity can be combined to yield the expressions shown in Equation (A.5) and (A.6).

$$\omega = \frac{0.622 \phi p_g}{p - \phi p_g} \qquad \left[\mathrm{kg_v/kg_{d.a}}\right] \quad \text{(A.5)}$$

$$\phi = \frac{\omega p}{(0.622 + \omega) p_g} \qquad [\text{-}] \quad \text{(A.6)}$$

Since atmospheric air is a mixture of dry air and water vapour, the enthalpy of atmospheric air is given as the enthalpy of dry air and the enthalpy of water vapour. The amount of dry air in atmospheric air can be considered constant, but the amount of water vapour changes, thus this must be accounted for. The enthalpy of atmospheric air is therefore given as in Equation (A.7).

$$h = h_{\mathrm{a}} + \omega h_g \qquad [\text{-}] \quad \text{(A.7)}$$

Where:
h is the total enthalpy [kJ/kg]
h_a is the enthalpy of dry air [kJ/kg]
h_g is the enthalpy of saturated water vapour at a given temperature [kJ/kg]

The dew point temperature, T_{dp}, is defined as the temperature where condensation occurs due to cooling of atmospheric air at constant pressure, thus it is the saturation temperature of water at the vapour pressure. This is given in Equation (A.8).

$$T_{\mathrm{dp}} = T_{sat@p_v} \qquad [\text{-}] \quad \text{(A.8)}$$

Properties for atmospheric air is usually looked up in a Psychrometric Chart. Such a chart is shown in Figure A.1. (Cengel and Boles, 2004)

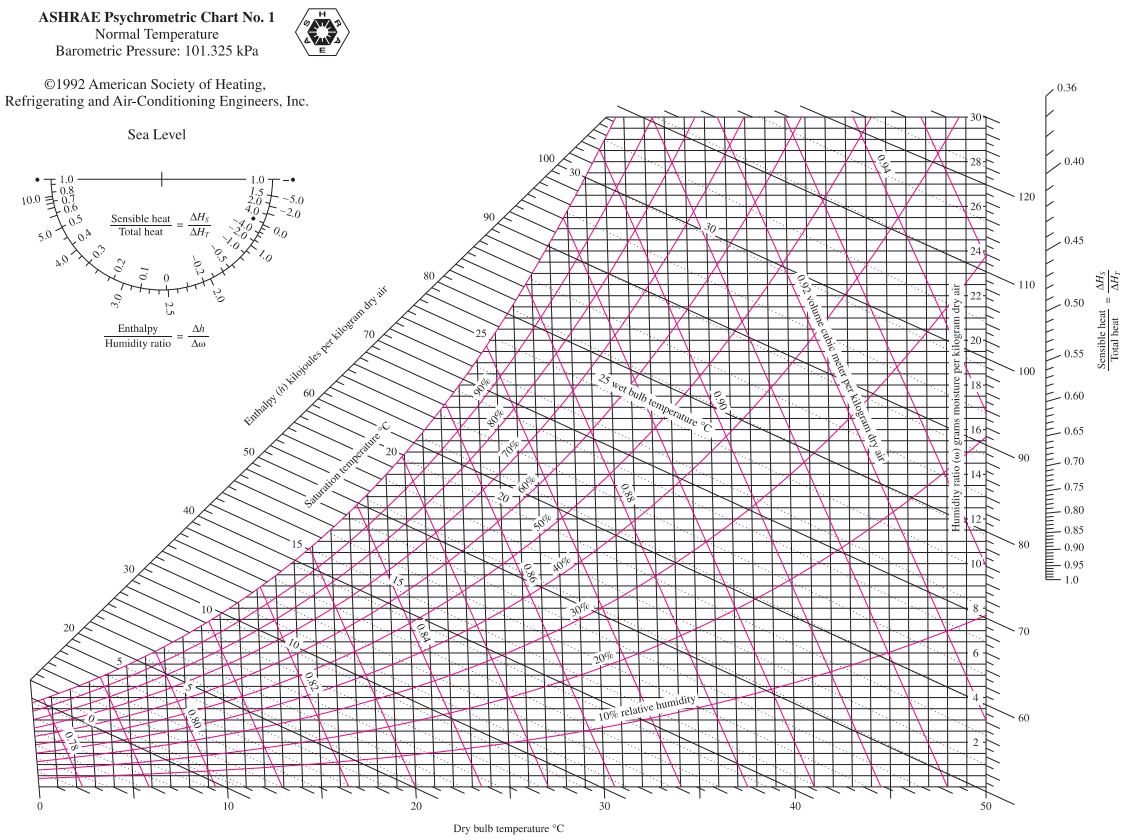

Figure A.1. Psychrometric Chart that is used to look up properties of atmospheric air (Cengel and Boles, 2004).

A phase diagram for water is given in Figure A.2.

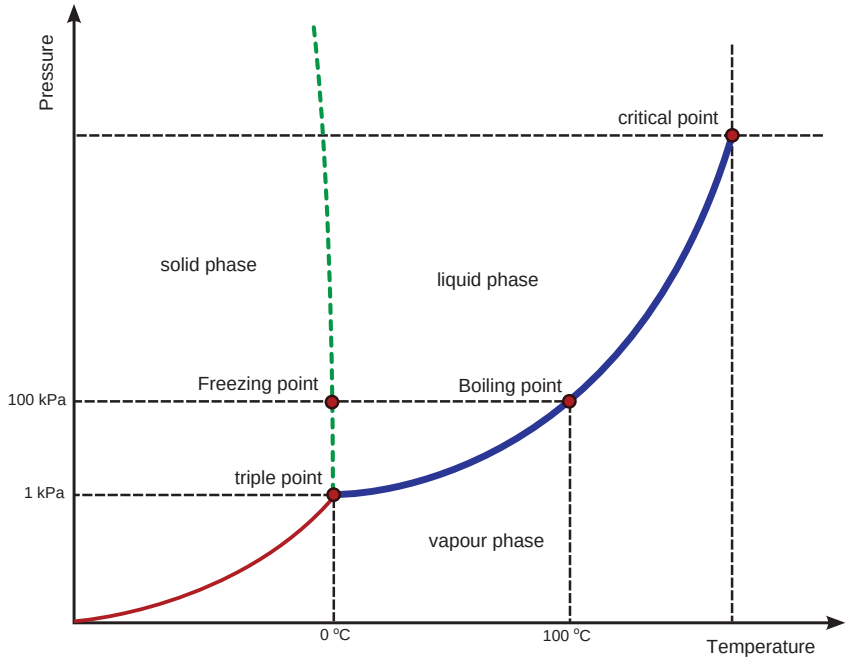

Figure A.2. Phase change diagram for water.

Appendix B

Refrigerant: R407C

In general refrigerants are divided into three categories - chlorofluorocarbons (CFC's), hydrochlorofluorocarbons (HCFC's), and hydrofluorocarbons (HFC's). Both CFC's and HCFC's contain chlorine, which contributes to the destruction of the ozone layer. The CFC's were initially dealt with by The Montreal Protocol (1990), which phased out the CFC's by the year 2000. After this the HCFC's have been temporarily allowed to ease the transition to HFC's. In the following period the HCFC R22 has been widely used, and is now being phased out. In order to make a smooth transition to HFC's, R407C was developed to perform very similar to R22. (John Roe, 3D Air Sales Ltd, 2000)

R407C is a blend of R32, R125, and R134a. It contains no chlorine and has a 'Zero Ozone Depleting Potential'. Since R407C is a blended refrigerant, at a certain pressure each of the component parts will boil at a different temperature. This is causing a 'temperature glide' of a few degrees at a phase change (John Roe, 3D Air Sales Ltd, 2000).

This kind of refrigerant is known as 'zeotropes', and the phenomenon can be seen by the slight slope of the temperature and pressure lines at the P-h and T-s diagrams on Figure B.1.

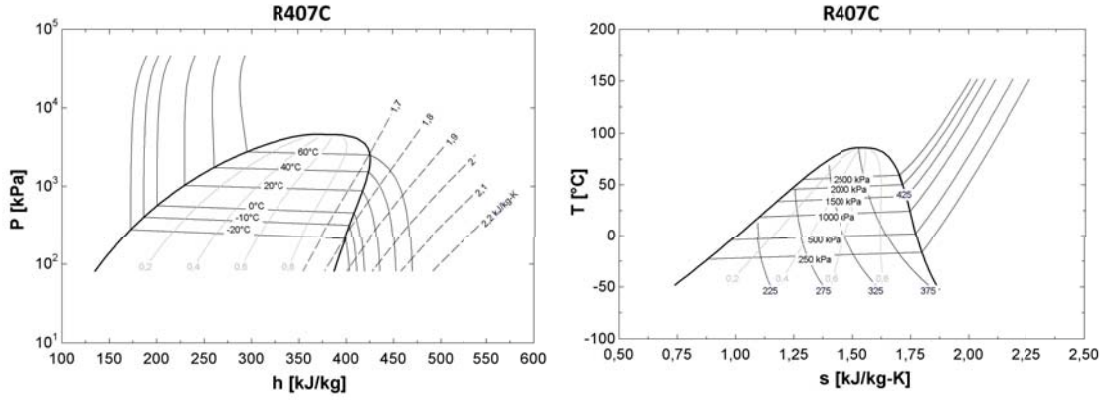

Figure B.1. Pressure/enthalpy and temperature/entropy diagrams for R407C.

A typical P-h diagram is shown in Figure B.2 along with the behaviour of R407C when evaporated through a counterflow evaporator.

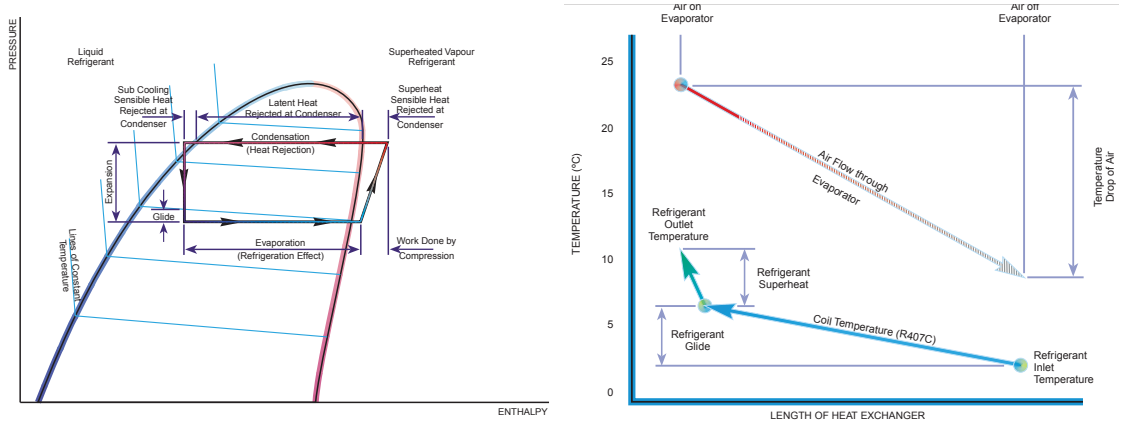

Figure B.2. Typical behaviour of R407C in a heat pump cycle (left) and through a counterflow heat exchanger during evaporation (right). (John Roe, 3D Air Sales Ltd, 2000)

In Figure B.2, the left side image shows a P-h diagram similar to that of B.1. However, in Figure B.2, the heat pump cycle of R407C is sketched and explained. It is also seen that the evaporation process takes place over a temperature glide. In the right part of Figure B.2, the evaporation process through a counterflow heat exchanger is shown. This process is similar to that of a cross-flow heat exchanger. Notice the amount of superheat added to the refrigerant in the end of the process. In the DVI LV9 heat pump the operation is controlled with a superheat of 5 K as reference point.

Appendix C

Bessel Functions for Circular Fins

Bessel functions and modified Bessel functions are widely used within heat transfer problems for extended surfaces. In this case they are used to solve differential equations describing the temperature distribution along circular fins and the fin efficiency for such fins. The circular fin considered is illustrated in Figure C.1.

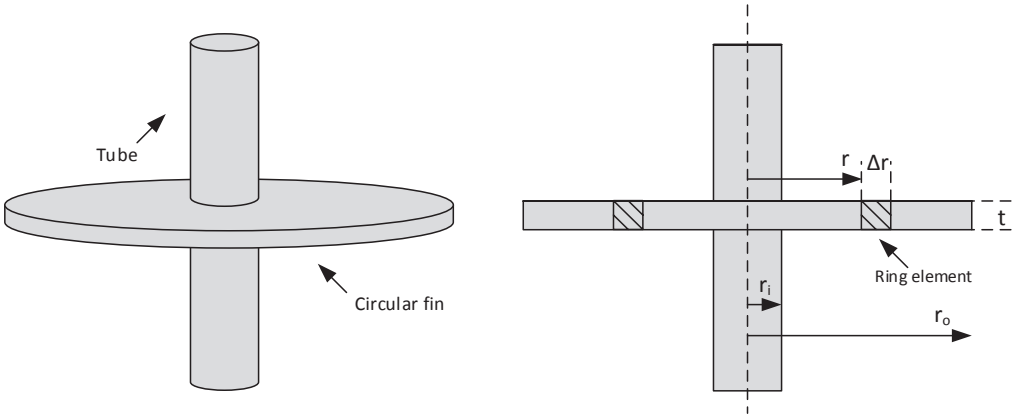

Figure C.1. Illustration of the circular fin on a tube.

The circular fin is approximated by the hexagonal fin as described in Section 5.6. By considering one-dimensional steady-state heat balance over the ring element in the circular fin shown in Figure C.1, the temperature distribution in the fin can be derived using the approach from Theerakulpinut (1995).

The conduction heat transfer rate through the area at r can be expressed by Fourier's law and is given as in Equation (C.1).

$$q_r = -kA\frac{dT}{dr}\bigg|_r \quad [\mathrm{W}] \quad \text{(C.1)}$$

Where:
q_r is heat transfer rate [W]
k is conductivity for the fin material [W/(mK)]
A is side area [m^2]
T is fin temperature [K]
r is the distance from the tube centre to the ring element [m]

The area A corresponds to the area of the side and is given as $2\pi rt$.

The conduction heat transfer can be written similarly for the area at $r + \Delta r$ as in Equation (C.2).

$$q_{r+\Delta r} = -kA\frac{dT}{dr}\bigg|_{r+\Delta r} \quad [\mathrm{W}] \quad \text{(C.2)}$$

Where:
$r + \Delta r$ is the distance from the tube centre to the end of the ring element.

The heat convection that occurs from the ambient air at the temperature T_∞ with the heat transfer coefficient h can be expressed as Newton's law of cooling and is given in Equation (C.3).

$$q_{\mathrm{conv}} = hA_c(T - T_\infty) \quad [\mathrm{W}] \quad \text{(C.3)}$$

Where:
q_{conv} is convective heat transfer $[\mathrm{W/(m^2K)}]$
A_c is surface area $[\mathrm{m^2}]$

The area A_c corresponds to the top and bottom surface area of the ring element and is given as $2(2\pi r\Delta r)$

The energy balance of the ring element can be expressed as in Equation (C.4).

$$q_r = q_{r+\Delta r} + q_{\mathrm{conv}} \quad [\mathrm{W}] \quad \text{(C.4)}$$

Substituting the expressions from Equation (C.1) to (C.3) into Equation (C.4) and rearranging the terms yields the energy balance shown in Equation (C.5).

$$\frac{r\frac{dT}{dr}\Big|_{r+\Delta r} - r\frac{dT}{dr}\Big|_{r}}{dr} - \frac{2h}{tk}r(T - T_\infty) = 0 \quad [-] \quad \text{(C.5)}$$

With $\Delta r \to 0$, the relationship in Equation (C.5) can be written as in Equation (C.6).

$$\frac{d}{dr}\left(r\frac{dT}{dr}\right) - \frac{2h}{tk}r(T - T_\infty) = 0 \quad [-] \quad \text{(C.6)}$$

This can be rewritten to the expression given in Equation (C.7).

$$r^2\frac{d^2T}{dr^2} + r\frac{dT}{dr} - \frac{2h}{kt}r^2(T - T_\infty) = 0 \quad [-] \quad \text{(C.7)}$$

Setting $\theta = T - T_\infty$ and $m^2 = \frac{2h}{kt}$ gives the expression in Equation (C.8).

$$r^2\frac{d^2\theta}{dr^2} + r\frac{d\theta}{dr} - m^2r^2\theta = 0 \quad [-] \quad \text{(C.8)}$$

Equation (C.8) is comparable to the modified Bessel equation given in Equation (C.9).

$$r^2\frac{d^2\theta}{dr^2}+r\frac{d\theta}{dr}-(\lambda^2r^2+v^2)y=0 \qquad [-] \text{ (C.9)}$$

The Bessel equation has the solution $\theta = C_1I_v(\lambda r)+C_2K_v(\lambda r)$. Similarly, the solution to Equation (C.8) is $\theta = C_1I_0(mr)+C_2K_0(mr)$. I_0 is the modified Bessel function of the first kind of order zero. K_0 is the modified Bessel function of second kind of order zero. C_1 and C_2 are two constants that are determined by the following boundary conditions.

$$\theta=\theta_i \text{ at } r=r_i$$
$$\frac{d\theta}{dr}=0 \text{ at } r=r_o$$

The modified Bessel functions of order one are introduced and they are equal to the derivatives of the modified Bessel functions of order zero.

$$\frac{d}{dx}(I_0(x))=I_1(x)$$
$$\frac{d}{dx}(K_0(x))=-K_1(x)$$

Using the modified Bessel functions of both order zero and one and the boundary conditions, the constants C_1 and C_2 are found and substituted into the solution to the Bessel function and solved for the temperature T(r). This is given in Equation (C.10).

$$T(r)=T_\infty+(T_i-T_\infty)\frac{K_1(mr_o)I_0(mr)+I_1(mr_o)K_0(mr)}{I_0(mr_i)K_1(mr_o)+I_1(mr_o)K_0(mr_i)} \qquad [-] \text{ (C.10)}$$

The fin efficiency is found by considering the ideal and actual heat flows. The actual heat flow is found using Equation (C.11).

$$q_{\text{fin}}=-2\pi kr_it\left.\frac{d\theta}{dr}\right|_r \qquad [-] \text{ (C.11)}$$

The ideal heat flow is calculated using Equation (C.12).

$$q_{\text{fin,ideal}}=2\pi(r_i^2-r_o^2)h\theta_i \qquad [-] \text{ (C.12)}$$

The fin efficiency is given as the actual heat flow to the ideal heat flow as shown in Equation (C.13).

$$\eta_{\text{fin}}=\frac{q_{\text{fin}}}{q_{\text{fin,ideal}}} \qquad [-] \text{ (C.13)}$$

The fin efficiency can be rewritten as in Equation (C.14).

$$\eta_{\text{fin}}=\frac{2r_{\text{i}}}{m(r_o^2-r_i^2)}\frac{I_1(mr_o)K_1(mr_i)-K_1(mr_o)I_1(mr_i)}{I_0(mr_i)K_1(mr_o)+I_1(mr_o)K_0(mr_i)} \qquad [-] \text{ (C.14)}$$

Appendix D

CD Content

---

1. Data Sheets
2. Experimental Data
3. Models
4. Digital Copy of Report
5. Images
6. LabVIEW Program